RESTRICTED

FP7-ICT Future Networks
SPECIFIC TARGETTED RESEARCH PROJECT
Project Deliverable

PHYDYAS Doc. Number	PHYDYAS_ 007
Project Number	ICT - 211887
Project Acronym+Title	PHYDYAS – PHYsical layer for DYnamic AccesS and cognitive radio
Deliverable Nature	Report
Deliverable Number	D5.1
Contractual Delivery Date	January 1, 2009
Actual Delivery Date	January 22, 2009
Title of Deliverable	Prototype filter and structure optimization
Contributing Workpackage	WP5: Prototype filter and filter bank structure
Project starting date; Duration	01/01/2008; 30 months
Dissemination Level	CO
Author(s)	Ari Viholainen (TUT – WP5 leader), Maurice Bellanger (CNAM), Mathieu Huchard (LETI)

Abstract: This deliverable first describes a modular filter bank structure and develops a unified signal model which, together with a modular and parametrised software implementation, provides a solid basis for utilizing the filter banks in other WPs. Different prototype filter design methods and alternative optimization criteria are included and extensive numerical results are provided to characterize the resulting designs. Also a study of the impact of the RF front-end impairments in FBMC has been initiated. An option of partial filter bank design is developed, for example to equip a low rate user in uplink in an efficient manner. Also a single-carrier -like transmission mode is developed and shown to provide similar PAPR benefit over basic FBMC transmission as what is achieved through DFT-spread OFDM, which has been adopted to the 3GPP-LTE uplink.

Contents

Notations

$\angle\{x\}$ the argument of a complex number x in [0,2π),

Re{.} real part

Im{.} imaginary part

(.)* complex conjugation

| . | absolute value

M overall number of subcarriers, FFT size

M_u^i number of used subcarriers of the ith user (in single-user case, index i is dropped)

$\mathcal{M}_u^i$ set of used subcarriers of the ith user

M_v number of virtual (unused) subcarriers

K overlapping factor in prototype filter design

α roll-off factor in prototype filter design

L_p prototype filter length

L_{eq} subcarrier equalizer length

T_s sampling interval (at SFB output and AFB input)

f_s sampling rate (at SFB output and AFB input) $f_s = 1/T_s$

T OQAM symbol duration; $T=MT_s$

Δf subcarrier spacing, $\Delta f = 1/T = f_s/M$

k subcarrier index (k=0, …, M-1; k=0 corresponds to center subcarrier)

l time index at OQAM symbol rate (→ T)

n time index at OQAM subsymbol rate (→ $T/2$)

m time index at SFB output/AFB input (→ T/M)

i user index in multiuser cases

U number of users

$v^R[n]$ real part of (arbitrary) complex sequence $v[n]$

$v^I[n]$ imaginary part of (arbitrary) complex sequence $v[n]$

$p(t)$ prototype filter impulse response, continuous-time model

$p[m]$ prototype filter impulse response, discrete-time [1]

$$p[m] = \sqrt{T_s}\, p\left(mT_s\right)$$

$P(z)$ prototype filter transfer function

$f_k[m]$ analysis filter impulse response for subchannel k

$F_k(z)$ analysis filter transfer function for subchannel k

$G_k(z)$ synthesis filter transfer function for subchannel k

$g_k[m]$ synthesis filter impulse response for subchannel k

$$g_k[m] = p[m] e^{j\frac{2\pi}{M}k\left(m-\frac{L_p-1}{2}\right)}$$

$p_{k,n}[m]$ SFB impulse response for real symbol $d_{k,n}$ (see also definition of $s[m]$)

$$p_{k,n}[m] = \theta_{k,n}\beta_{k,n} g_k[m - nM/2]$$

$$= \theta_{k,n}\beta_{k,n} p[m - nM/2] e^{j\frac{2\pi}{M}km}$$

$\theta_{k,n}$ phase mapping between real data sequence and complex samples at the SFB input

In general,

$$\theta_{k,n} = \begin{cases} \pm 1 & \text{for } k+n \text{ even} \\ \pm j & \text{for } k+n \text{ odd} \end{cases}$$

The recommended choice (following Siohan's papers) is [2]:

$$\theta_{k,n} = j^{k+n}$$

$$\beta_{k,n} = e^{j2\pi k\left(-\frac{n}{2}-\frac{L_p-1}{2M}\right)}$$

$d_{k,n}^{i}$ transmitted sequence of the *i*th user (data & pilots) (real)

$x_{k,n}$ observed ideal (without channel) complex sample sequence at AFB output,

$$\theta_{k,n}^{*} x_{k,n} = d_{k,n} + j u_{k,n}$$

Here $u_{k,n}$ is the un-interesting part of the received complex samples.

$y_{k,n}$ observed channel-distorted complex sample sequence at AFB output

$\tilde{d}_{k,n}$ real part of the subcarrier sequence after equalization and multiplication by $\theta_{k,n}^{*}$

$\hat{d}_{k,n}$ detected sequence (real)

$s[m]$ transmitted sequence at SFB output, single user case

$$\begin{aligned} s[m] &= \sum_{k\in\mathcal{M}_u}\sum_{n=-\infty}^{\infty} d_{k,n}\theta_{k,n} g_k\left[m-nM/2\right] \\ &= \sum_{k\in\mathcal{M}_u}\sum_{n=-\infty}^{\infty} d_{k,n}\theta_{k,n} p\left[m-nM/2\right] e^{j\frac{2\pi}{M}k\left(m-n\frac{M}{2}-\frac{L_p-1}{2}\right)} \\ &= \sum_{k\in\mathcal{M}_u}\sum_{n=-\infty}^{\infty} d_{k,n}\theta_{k,n}(-1)^{kn}\, p\left[m-nM/2\right] e^{j\frac{2\pi}{M}k\left(m-\frac{L_p-1}{2}\right)} \\ &= \sum_{k\in\mathcal{M}_u}\sum_{n=-\infty}^{\infty} d_{k,n}\theta_{k,n}\beta_{k,n} p\left[m-nM/2\right] e^{j\frac{2\pi}{M}km} \\ &= \sum_{k\in\mathcal{M}_u}\sum_{n=-\infty}^{\infty} d_{k,n} p_{k,n}[m] \end{aligned}$$

$s_i[m]$ transmitted sequence at SFB output in the uplink multiuser FBMC system, e.g.,

$$s_i[m] = \sum_{k\in\mathcal{M}_u^{i}}\sum_{n=-\infty}^{\infty} d_{k,n} p_{k,n}[m]$$

$s(t)$ transmitted continuous-time signal ($s_i(t)$ correspondingly for user *i* in multiuser case)

$$s(t) = \sum_{k\in\mathcal{M}_u}\sum_{n=-\infty}^{\infty} d_{k,n}\theta_{k,n}(-1)^{kn}\, p\left(t-n\frac{T}{2}\right) e^{j2\pi k\left(\Delta f t-\frac{L_p-1}{2M}\right)}$$

$r(t)$ received continuous-time signal in the uplink multiuser FBMC system

$$r(t) = \sum_{i=1}^{U} e^{j2\pi(\frac{\varepsilon_i}{T}t)} h_i(t,\tau) * s_i(t) + \eta(t) \qquad \text{general case}$$

$$r(t) = \sum_{i=1}^{U} e^{j2\pi(\frac{\varepsilon_i}{T}t)} \sum_{p=0}^{P_i-1} c_{i,p} s_i(t-\tau_{i,p}) + \eta(t) \qquad \text{discrete multipath case}$$

$$r(t) = \sum_{i=1}^{U} e^{j2\pi(\frac{\varepsilon_i}{T}t)} c_i s_i(t-\tau_i) + \eta(t) \qquad \text{AWGN case}$$

$$= \sum_{i=1}^{U} e^{j2\pi(\frac{\varepsilon_i}{T}t+\phi_i)} |c_i| s_i(t-\tau_i) + \eta(t)$$

ε_i carrier frequency offset of the *i*th user, normalized to subcarrier spacing

ϕ_i carrier phase offset (radians) of the *i*th user in the AWGN model

$h_i(t,\tau)$ time-variant channel impulse response of *i*th user

P_i number of paths in the multipath channel model of user *i*

$c_{i,p}$ complex gain of the *p*th path of the channel of user *i*

$\tau_{i,p}$ delay of the *p*th path of the channel of user *i*

τ_i timing offset of the *i*th user in the AWGN model

$\eta(t)$ complex envelope of white (Gaussian) noise whose real and imaginary parts are statistically independent and have a power spectral density level of N_0

σ_η^2 channel noise variance

N_0 one-sided noise power spectral density of white channel noise

$r[m]$ received complex sequence at AFB input

$\eta[m]$ channel noise

$h_i[m]$ discrete-time channel impulse response for user *i* in block-fading model

$H_i(e^{j\omega})$ channel frequency response for user *i*

H_k channel response of subcarrier *k* (assuming flat-fading and time invariant/block-fading case)

$H_{k,n}$ channel response for subcarrier *k* and symbol *n* (assuming flat-fading and time variant case)

$H_{k,n}^{p,q}$ channel response for subcarrier *k* and symbol *n* from TX antenna *p* to RX antenna *q*

$w_k[n]$ subcarrier-wise channel equalizer impulse response for subchannel *k*

Notes:

(1) This assumes causal continuous-time prototype filter impulse response, which is different from Siohan's continuous-time model.

(2) The choice of $\theta_{k,n}$, i.e., the signs in mapping real data sequence to complex samples at the SFB input is an internal choice of the filter bank module (i.e., the definition of $x_{k,n}$ above can be assumed to be valid in any case). However, it has an effect on the signal models at the SFB output and for the complex sequences at the AFB output. In the receiver side, $\beta_{k,n}^*$ is implemented before the subband processing, and $\theta_{k,n}^*$ after it. With this choice, all the subchannels are centered at DC at the subchannel processing stage.

1 Introduction

Multicarrier modulation is an efficient transmission technique, where the available channel bandwidth is subdivided into several parallel subchannels, each with its own associated carrier. A transmitter should efficiently combine several low-rate input signals into a single high-rate signal, which is then transmitted over a channel, and a receiver should be able to reconstruct at least good approximations of the low-rate signals. A synthesis-analysis filter bank, i.e., transmultiplexer (TMUX) structure can be considered to be the core of multicarrier system. The synthesis filter bank (SFB) consists of all parallel transmit filters and the analysis filter bank (AFB) includes the matching receive filters. There are many different realization solutions because the field of filter banks is very broad. In the case of practical applications, the implementation complexity is one of the main criteria. Therefore, modulated filter banks are widely used as a computationally efficient solution whenever filter banks are needed. Modulated filter banks are very efficient from both the design and the implementation points of view because all subchannel filters can be generated from synthesis and analysis prototype filters by using cosine, sine, or exponential modulation [1][2][3].

There are many different kinds of multicarrier techniques, but orthogonal frequency division multiplexing (OFDM) has been, no doubt, the most prominent one. For example, OFDM has become the modulation choice for both wireless local area network (WLAN) and terrestrial digital broadcasting (digital audio and video broadcasting; DAB, DVB-T, DVB-H) standards [4]. From the filter bank point of view, OFDM is based on the use of the inverse and forward DFT for modulation and demodulation, respectively. In addition, the prototype filter is a rectangular window whose length is equal to the size of the block transforms. For ideal transmission channel, the perfect signal recovery is possible because subchannel filters are orthogonal. In practice, OFDM uses a cyclic prefix (CP), which is longer than the channel impulse response or the maximum multipath delay, to eliminate intersymbol interference (ISI) caused by the channel. However, the resulting subchannel filters are not spectrally well isolated. They consist of a mainlobe overlapping with immediate adjacent subchannels and high sidelobes that extend over a wide frequency band. The first sidelobe of a subchannel is only 13 dB below the mainlobe as can be seen in Figure 1-1. These sidelobes interfere with the mainlobes across the entire band and this can lead to an extensive intercarrier interference (ICI) problem in case of fast fading or carrier frequency offsets (CFOs). Also, the system performance may degrade significantly in the presence of narrowband interference. The energy of a narrowband interference spreads into many adjacent subchannels and this cannot be avoided by simply switching-off the subchannel in which the interference lies.

On the other hand, more recent multicarrier techniques, such as discrete wavelet multitone [5], filtered multitone (FMT) [6], cosine modulated multitone (CMT) [7], OFDM with offset QAM (OFDM/OQAM) based technique [7], modified DFT based technique [9], and exponentially modulated filter bank (EMFB) based technique [10], apply highly frequency selective filter banks instead of just using simple IDFT/DFT blocks. In general, these techniques can be called as filter bank based multicarrier (FBMC) techniques. The improved frequency selectivity has been accomplished by using longer and spectrally well-shaped prototype filters. Because of that, the sidelobe levels are considerably lower than in the case of OFDM as can be seen in Figure 1-1. In this way, a good spectral containment for all the subchannels can be obtained and this also results in a good resistance against narrowband interference. In fact, any subchannel overlaps significantly only with its neighboring subchannels. Then, in order to make two multicarrier signals independent, it is sufficient to leave an empty subchannel between them. However, the consecutive symbol waveforms are highly overlapping in time when the frequency selectivity of subchannels is

improved. Due to the overlapping symbols, a cyclic prefix approach need not, and cannot be used. Consequently, the subchannels cannot be expected to be flat-fading, in contrast to CP-OFDM.

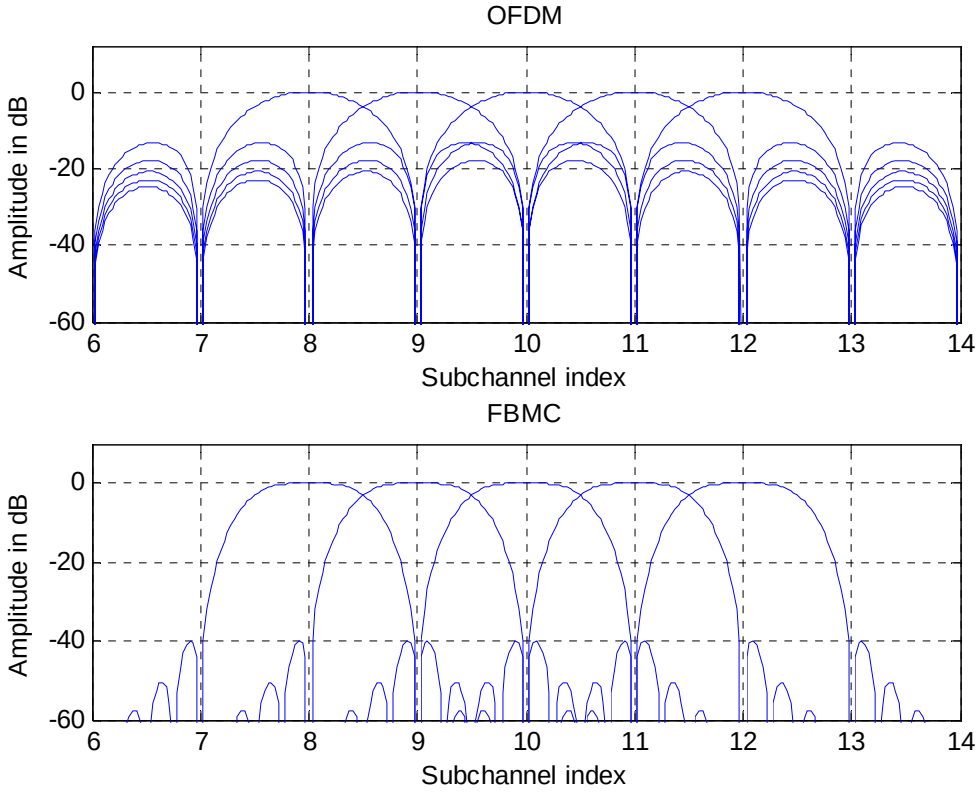

Figure 1-1: Comparison of subchannel filter magnitude responses in the case of OFDM and FBMC.

1.1 Objectives of Work Package 5

The objective of PHYDYAS project is to propose a FBMC-based physical layer for the new concepts of dynamic access spectrum management (DASM) and cognitive radio. The analysis and synthesis filter banks are naturally the key components in the PHYDYAS project. During the first phase of the project, the work is based on a selected filter bank design known from the literature [11]. This filter bank is based on the polyphase structure and analytical formulas for calculating the prototype filter coefficients for a wide choice of the main parameters. The term PHYDYAS reference filter bank refers to this design with the prototype filter length $L_p = 4M - 1$, where M is the number of subchannels.

In PHYDYAS, the Work Package 5 is focusing on the performance analysis and further optimization of the filter banks for use during the later phases of the project. The original targets included:

- Development of simple, flexible and low-complexity filter bank structures.
- Optimization of the prototype filter and performance analysis, from the perspective of the specifications of the RF front end and for spectrum sensing in a cognitive radio scenario.
- Development of configurations where analysis and synthesis filter banks are of different sizes (considering, e.g., scenarios of wide-band base station receiver and multiple narrow-band mobile transmitters),

- Investigation of flexible channel selection filter design, utilizing the filter bank as the last stage of a multistage filter in the analog-digital chain,

During the project, the work was extended to cover also single-carrier -like transmission mode with reduced PAPR (peak-to-average power ratio) for uplink transmission. This is basically an extension of the DFT-spread OFDM idea which has been adopted to the uplink of the 3GPP-LTE (E-UTRA) system [12] .

1.2 Contents of Deliverable 5.1

The rest of this deliverable is organized as follows. First in Chapter 2, the utilized analysis and synthesis filter bank structures, with offset-QAM model for subcarrier modulation, are formulated. The chapter includes also a brief discussion of the connections between the adopted TMUX model and other types of filter bank structures considered in the FBMC contexts.

Chapter 3 focuses on the prototype filter design methods and optimization criteria. Chapter 3 includes also comparisons of alternative designs considering frequency selectivity and total filter bank structure based interference ($\mathrm{TOI} = \mathrm{ISI} + \mathrm{ICI}$) in case of an ideal TMUX system, as well as, PAPR and spectrum sensing characteristics. The prototype filter design is likely to have some effect also on the sensitivity to the ICI introduced by CFO and fading channel, as well as on the channel equalizer performance. However, these effects depend crucially on the synchronization and channel equalization methods, and the effect of the prototype filter on these issues is investigated under PHYDYAS WP3.

Chapter 4 concentrates on the analog and digital front-end aspects. First we discuss the role of the synthesis and analysis filter banks in implementing sharp channel filtering characteristics for the transmitter and receiver, respectively. Then RF architectures are briefly discussed and the sensitivity of FBMC system to various RF impairments is investigated.

Chapter 5 investigates first the idea of partial TMUX systems, showing how it is possible to combine synthesis and analysis filter banks of different sizes in the TMUX configuration. Then we study the possibilities to utilize a block of adjacent subchannels for single-carrier transmission. The idea of filter bank-spread FBMC transmission is formulated and shown to provide similar PAPR benefit over multicarrier FBMC transmission as what is achieved in DFT-spread OFDM in comparison to OFDM.

Finally, Chapter 6 summarizes the results of this deliverable and gives some recommendations about the choice of the filter bank design.

2 Filter bank structure

One basic choice made already during the planning phase of PHYDYAS was to consider FBMC schemes based on the OFDM/OQAM model [8], where the subcarrier modulation is of the offset-QAM type. Noting that the OFDM/OQAM model is essentially equivalent to the modified DFT (MDFT) filter bank model [9], it can be stated that the OFDM/OQAM model is clearly the most common FBMC principle considered in the literature. The use of OFDM/OQAM model has various implications on the filter bank structures, but it does not limit the generality of the studies. This is because other common forms of FBMC systems can be shown to be closely connected to the adopted model, as will be discussed in Section 2.5.

2.1 Description of TMUX system

The core of the FBMC system is the TMUX configuration shown in Figure 2-1. The main processing blocks in this direct form representation are OQAM pre-processing, synthesis filter bank, analysis filter bank, and OQAM post-processing. The transmission channel is typically omitted when analyzing and designing TMUX systems because the channel equalization problem is handled separately.

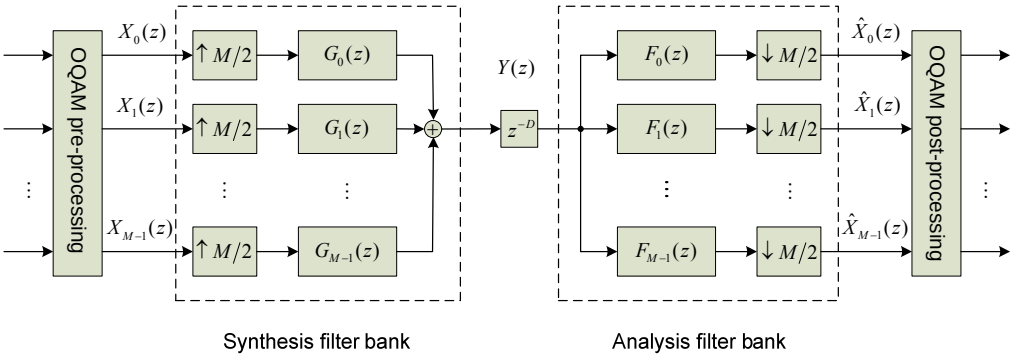

Figure 2-1: TMUX configuration.

The synthesis and analysis filter banks are naturally the key components. As already mentioned, the field of filter banks is very broad and even modulated filter banks can be divided into different types depending on the choice of the prototype filters, modulation functions, and desired properties. In PHYDYAS project, we have decided to study M-subchannel filter banks that can be classified by the following terms:

- *Complex modulated*: In order to achieve a good spectral efficiency, a complex I/Q baseband signal is needed for transmission purposes and complex modulated filter banks are a logical choice. This means that all subchannel filters are frequency shifted versions of the prototype filter.

- *Uniform*: All subchannel filters have the same bandwidth as the prototype filter and they divide the available channel bandwidth equally.

- *Finite impulse response (FIR)*: FIR filter banks are used instead of their infinite impulse response (IIR) counterparts because FIR filters are always stable and they are relatively easy to design and implement.

- *Orthogonal*: For orthogonal filter banks, only a single prototype filter is needed. Typically, linear-phase prototype filters are used, and therefore exponential modulation schemes can provide linear-phase subchannel filters. The resulting overall system delay depends on the order of the prototype filter.

- *Nearly perfect reconstruction (NPR)*: The output signals are only approximately delayed versions of the input signals, i.e., certain amount of filter bank structure based distortions can be tolerated as long as they are small compared to those caused by a transmission channel.

The main filter bank design parameters are:

- The number of subchannels M is basically an arbitrary even number, but typically it is a power of two in order to provide efficient implementation.

- The most interesting prototype filter lengths are chosen to be $L_p = KM - 1$, $L_p = KM$, and $L_p = KM + 1$, where K is a positive integer called as overlapping factor and it is selected to be 3 or higher.

- The prototype filter is designed in such a manner that only immediately adjacent subchannel filters are significantly overlapping with each other in the frequency domain.

The number of subchannels is twice the upsampling and downsampling factors indicating 2x oversampled filter banks if input and output signals are complex-valued. However, if input and output signals are purely real/imaginary-valued then the presented TMUX is equivalent to a critically sampled TMUX. This is because the sample rate (counted in terms of real-valued samples) of the SFB output and AFB input is equal to the sum of the sample rates of the subchannel signals. An extra delay z^{-D}, with D depending on the length of the prototype filter ($L_p = KM + 1 - D$), has to be included either to the SFB output or AFB input.

2.1.1 OQAM pre/post-processing

Our TMUX system transmits OQAM symbols instead of QAM symbols. The pre-processing block, which utilizes the transformation between QAM and OQAM symbols, is shown in Figure 2-2. As can be seen, the first operation is a simple complex-to-real conversion, where the real and imaginary parts of a complex-valued symbol $c_{k,l}$ are separated to form two new symbols $d_{k,2l}$ and $d_{k,2l+1}$ (this operation can also be called as staggering). The order of these new symbols depends on the subchannel number, i.e., the conversion is different for even and odd numbered subchannels. The complex-to-real conversion increases the sample rate by a factor of 2. The second operation is the multiplication by $\theta_{k,n}$ sequence.

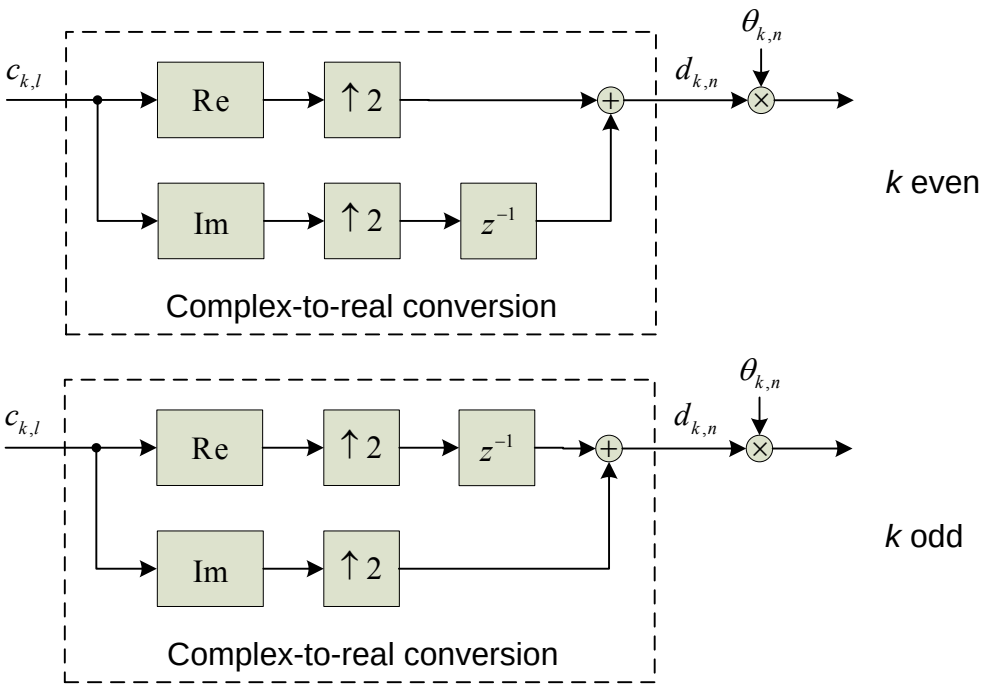

Figure 2-2: OQAM pre-processing section.

A possible choice is

$$\theta_{k,n} = j^{(k+n)} \tag{1}$$

and the same sequence is used in [8]. However, it should be noted that the signs of the $\theta_{k,n}$ sequence can be chosen arbitrarily, but the pattern of real and imaginary samples has to follow the above definition. For example, an alternative sequence

$$\theta_{k,n} = \begin{cases} 1, j, 1, j, \ldots & \text{for } k \text{ even} \\ j, 1, j, 1, \ldots & \text{for } k \text{ odd} \end{cases} \tag{2}$$

is used in [9]. Anyway, input signals are purely real or imaginary -valued after the OQAM pre-processing.

The post-processing block is shown in Figure 2-3 and again there are two slightly different structures depending on the subchannel number. The first operation is the multiplication by $\theta^*_{k,n}$ sequence that is followed by the operation of taking the real part. The second operation is real-to-complex conversion, in which two successive real-valued symbols (with one multiplied by j) form a complex-valued symbol $\hat{c}_{k,n}$ (this operation is also called as de-staggering). The real-to-complex conversion decreases the sample rate by a factor 2.

As can be seen, the first operation is a simple complex-to-real conversion, where the real and imaginary parts of a complex-valued symbol $c_{k,l}$ are separated to form two new symbols $d_{k,2l}$ and $d_{k,2l+1}$ (this operation can also be called as staggering). The order of these new symbols depends on the subchannel number, i.e., the conversion is different for even and odd numbered subchannels.

The complex-to-real conversion increases the sample rate by a factor of 2. The second operation is the multiplication by $\theta_{k,n}$ sequence

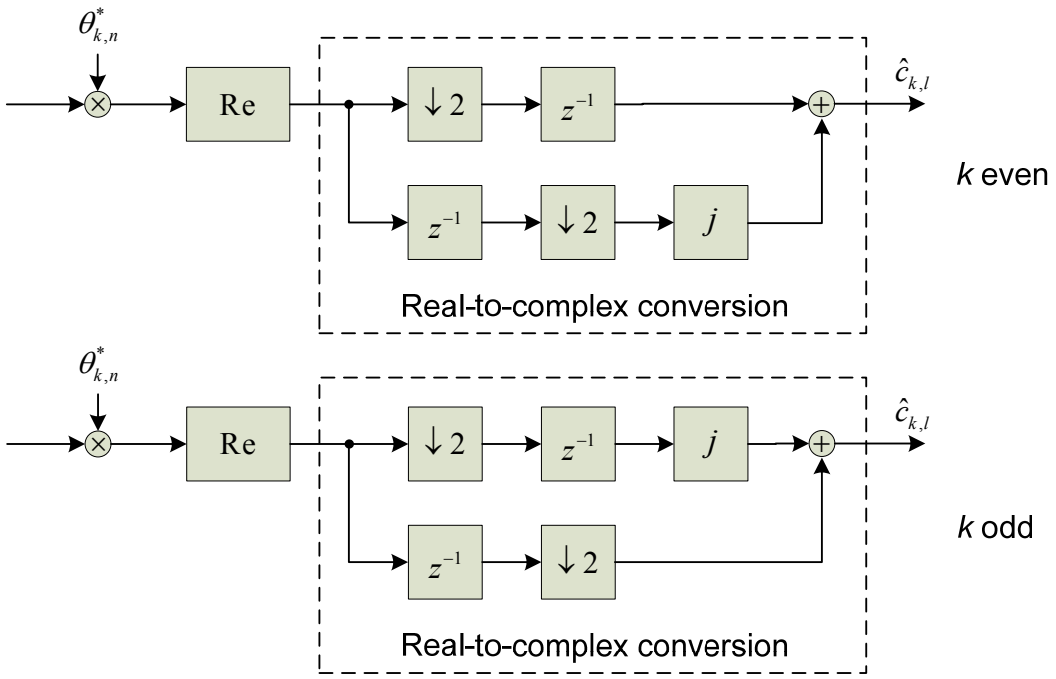

Figure 2-3: OQAM post-processing section.

2.1.2 Synthesis and analysis filter banks

A direct form SFB consists of M upsamplers and M synthesis filters. As shown in Figure 2-1, the input signals $X_k(z)$, where $k = 0, 1, \ldots, M-1$, are first upsampled by $M/2$ and then filtered with synthesis filters $G_k(z)$. The SFB output signal $Y(z)$ is formed when all subsignals are added together. A direct form AFB is constructed using M analysis filters and M downsamplers as shown in Figure 2-1. The input signal $Y(z)$ is first filtered by analysis filters $F_k(z)$ and these signals are then downsampled by a factor of $M/2$ to form output signals $\hat{X}_k(z)$.

In the case of chosen class of complex modulated filter banks, all subchannel filters can be generated from a single real-valued linear-phase lowpass prototype filter $p[m]$ by using exponential modulation. Due to the modulation function, the resulting subchannel filters are complex-valued and therefore the useful frequency range is $[-\pi, \pi]$. Typically, two different types of channel stacking arrangements can be considered, namely, even-stacked filter banks and odd-stacked filter banks. The center frequencies of the kth subchannel filters are $\omega_k = \frac{2k\pi}{M}$ and $\omega_k = \frac{(2k+1)\pi}{M}$ for even-stacked and odd-stacked filter banks, respectively.

In PHYDYAS project, we have chosen to use even-stacked filter banks, whereas odd-stacked filter banks have been studied e.g., in [10]. The following definitions are similar to those used in the case of MDFT filter banks [13]. The kth synthesis filter is defined by

$$g_k[m] = p[m] \exp\left(j\frac{2\pi k}{M}\left(m - \frac{L_p - 1}{2}\right)\right), \tag{3}$$

where $m = 0, 1, \ldots, L_p - 1$ and L_p is the filter length. In order to simplify notations, it is assumed that the prototype filter is designed in such a manner that there is no need for the additional scaling factor. The kth analysis filter is simply a time-reversed and complex-conjugated version of the corresponding synthesis filter

$$\begin{aligned} f_k[m] &= g_k^*[L_p - 1 - m] \\ &= p[L_p - 1 - m] \exp\left(-j\frac{2\pi k}{M}\left(L_p - 1 - m - \frac{L_p - 1}{2}\right)\right) \\ &= p[m] \exp\left(j\frac{2\pi k}{M}\left(m - \frac{L_p - 1}{2}\right)\right). \end{aligned} \tag{4}$$

An interpretation to the above equations is that first zero-phase subchannel filters are generated from a linear-phase prototype filter and then their impulse responses are delayed by $(L_p - 1)/2$ samples resulting in causal subchannel filters. Due to the nature of the modulation function, the 0th subchannel filter is purely real and the $\frac{M}{2}$th is purely imaginary. However, all the subchannel filters have linear phase.

2.2 Efficient implementation of filter bank structures

The direct form implementations of Figure 2-1 are not very efficient for practical applications because filtering operations are performed at the high sampling rate leading to a huge amount of unnecessary calculations. Luckily, there are various efficient multirate structures for the needed filter banks, including lapped transforms, lattice structures, and polyphase structures [1][2]. Common to all these structures is that they consist of a filter section, the coefficients of which are determined by the prototype filter design, and a transform section implementing the modulation. The polyphase structures are the only ones that can be applied to NPR filter banks. Their main advantage is that they can offer drastic simplifications because filtering operations are done at the lower sampling rate and no unnecessary calculations are performed. Next, polyphase structures for SFBs and AFBs are derived.

2.2.1 Polyphase structure of synthesis filter bank

In the case of modulated filter banks, the number of the polyphase filter branches depends on the periodicity of the modulation function. The periodicity of modulation function used in Eqs. (3) and (4), i.e.,

$$\begin{aligned} e_{k,m} &= \exp\left(j\frac{2\pi k}{M}\left(m - \frac{L_p - 1}{2}\right)\right) \\ &= \exp\left(-j\frac{2\pi k}{M}\left(\frac{L_p - 1}{2}\right)\right) \exp\left(j\frac{2\pi km}{M}\right) \\ &= \beta_k \Theta_{k,m} \end{aligned} \tag{5}$$

is M because $\Theta_{k,q+tM} = \Theta_{k,q}$, where $q = 0, 1, \ldots, M-1$ and $t = 0, 1, \ldots, K-1$. Now the kth synthesis filter can be expressed in the form of type-1 polyphase filters as follows

$$\begin{aligned} G_k(z) &= \sum_{m=0}^{L_p-1} p[m] e_{k,m} z^{-m} \\ &= \sum_{q=0}^{M-1} \sum_{t=0}^{K-1} p[q+tM] \beta_k \Theta_{k,q+tM} z^{-(q+tM)} \\ &= \sum_{q=0}^{M-1} \beta_k \Theta_{k,q} z^{-q} \sum_{t=0}^{K-1} p[q+tM] z^{-tM} \\ &= \sum_{q=0}^{M-1} \beta_k \Theta_{k,q} z^{-q} A_q(z^M). \end{aligned} \tag{6}$$

Now, all synthesis filters can be compactly represented using the following matrix notation

$$\mathbf{G}(z) = \mathbf{B} \cdot \mathbf{W} \cdot \mathbf{A}(z^M) \cdot \mathbf{c}(z), \tag{7}$$

where

$$\begin{aligned} \mathbf{G}(z) &= [G_0(z)\ G_1(z)\ \cdots\ G_{M-1}(z)]^T, \\ \mathbf{B} &= \mathrm{diag}[\beta_0\ \beta_1\ \cdots\ \beta_{M-1}], \\ [\mathbf{W}]_{k,q} &= \Theta_{k,q}, \\ \mathbf{A}(z^M) &= \mathrm{diag}[A_0(z^M)\ A_1(z^M)\ \cdots\ A_{M-1}(z^M)] \\ \mathbf{c}(z) &= [1\ z^{-1}\ \cdots\ z^{-(M-1)}]^T. \end{aligned} \tag{8}$$

The starting point of polyphase structure is the direct form synthesis filter bank shown in Figure 2-1. The output signals without downsampling can be written using matrix notations as

$$\begin{aligned} Y(z) &= \mathbf{G}^T(z) \cdot \mathbf{X}(z^{M/2}) \\ &= \left(\mathbf{B} \cdot \mathbf{W} \cdot \mathbf{A}(z^M) \cdot \mathbf{c}(z)\right)^T \cdot \mathbf{X}(z^{M/2}) \\ &= \mathbf{c}^T(z) \cdot \mathbf{A}(z^M) \cdot \mathbf{W} \cdot \mathbf{B} \cdot \mathbf{X}(z^{M/2}). \end{aligned} \tag{9}$$

where $\mathbf{X}(z^{M/2}) = [X_0(z^{M/2})\ X_1(z^{M/2})\ \cdots\ X_{M-1}(z^{M/2})]^T$ and other matrices are defined by Eq. (8). The above equation can be interpreted in such a manner that the synthesis filter bank consists of upsamplers by $M/2$, β_k-multipliers, IDFT, type-1 polyphase filters $A_q(z^M)$, and delay chain. By using the well-known multirate identity [2], all upsamplers can be moved through β_k-multipliers, IDFT, and polyphase filters. The resulting polyphase implementation structure is shown in Figure 2-4.

It can be noticed that the upsamplers and delay chain form a parallel-to-serial (P/S) converter with overlapping of $M/2$. This is because the number of branches is M and the upsampling factor is only

$M/2$. In this sense, polyphase filters $A_k(z^2)$ and $A_{k+M}(z^2)$ could actually share a common delay line.

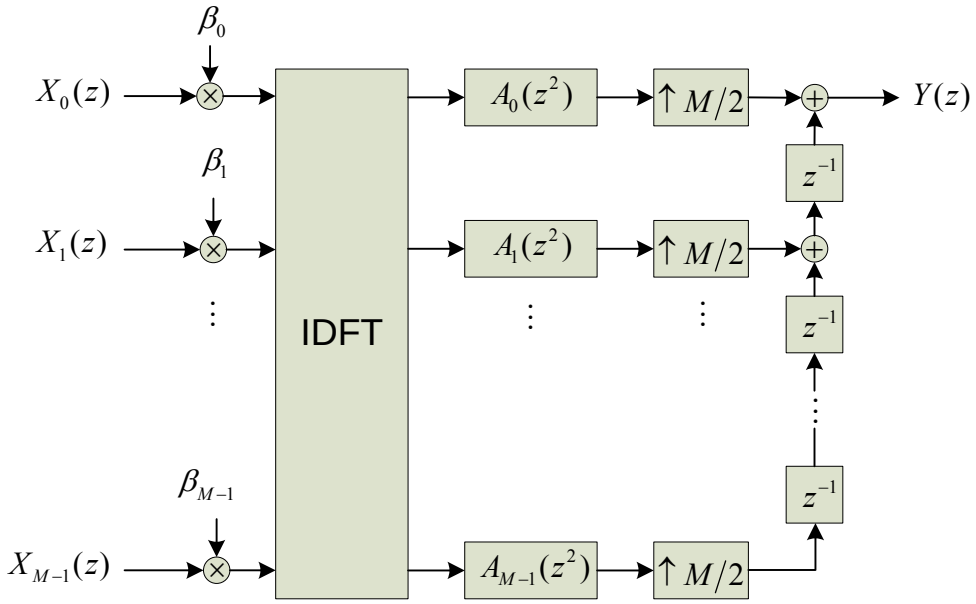

Figure 2-4: Efficient polyphase implementation of synthesis filter bank.

2.2.2 Polyphase structure of analysis filter bank

The analysis filters are defined using exactly the same equation as the synthesis filters. Therefore, the polyphase decomposition of the kth analysis filter can be directly written as follows

$$\begin{aligned} F_k(z) &= \sum_{m=0}^{L_p-1} h_p[m] e_{k,m} z^{-m} \\ &= \sum_{q=0}^{M-1} \beta_k \Theta_{k,q} z^{-q} A_q(z^M). \end{aligned} \tag{10}$$

Moreover, all analysis filters can be written using the matrix notation as follows

$$\mathbf{F}(z) = \mathbf{B} \cdot \mathbf{W} \cdot \mathbf{A}(z^M) \cdot \mathbf{c}(z), \tag{11}$$

where

$$\mathbf{F}(z) = [F_0(z)\ F_1(z)\ \cdots\ F_{M-1}(z)]^T \tag{12}$$

and other terms are the same as in Eq. (8).

The starting point of polyphase structure is the direct form analysis filter bank shown in Figure 2-1. The output signals can be written using matrix notations as

$$\begin{aligned}\hat{\mathbf{X}}(z^{M/2}) &= \mathbf{F}(z^M)\cdot Y(z)\\ &= \mathbf{B}\cdot\mathbf{W}\cdot\mathbf{A}(z^M)\cdot\mathbf{c}(z)\cdot Y(z),\end{aligned} \tag{13}$$

where $\hat{\mathbf{X}}(z^{M/2}) = [\hat{X}_0(z^{M/2})\ \hat{X}_1(z^{M/2})\ \cdots\ \hat{X}_{M-1}(z^{M/2})]^T$ and other matrices are defined by Eq. (8). The analysis filter bank can be interpreted to consist of delay chain, type-1 polyphase filters, IDFT, β_k-multipliers, and downsamplers by $M/2$. Naturally, the downsamplers by $M/2$ can be moved trough β_k-multipliers, IDFT, and polyphase filters. The resulting polyphase implementation structure is very similar to synthesis filter bank case as can be seen in Figure 2-5. The same main processing blocks as in the case of synthesis filter bank are used but in reversed order.

It can be noticed that the delay chain and downsamplers form an serial-to-parallel (S/P) converter with overlapping of $M/2$. This is because the number of branches is M and the downsampling factor is only $M/2$. Again, this means that polyphase filters $A_k(z^2)$ and $A_{k+M}(z^2)$ could actually share a common delay line.

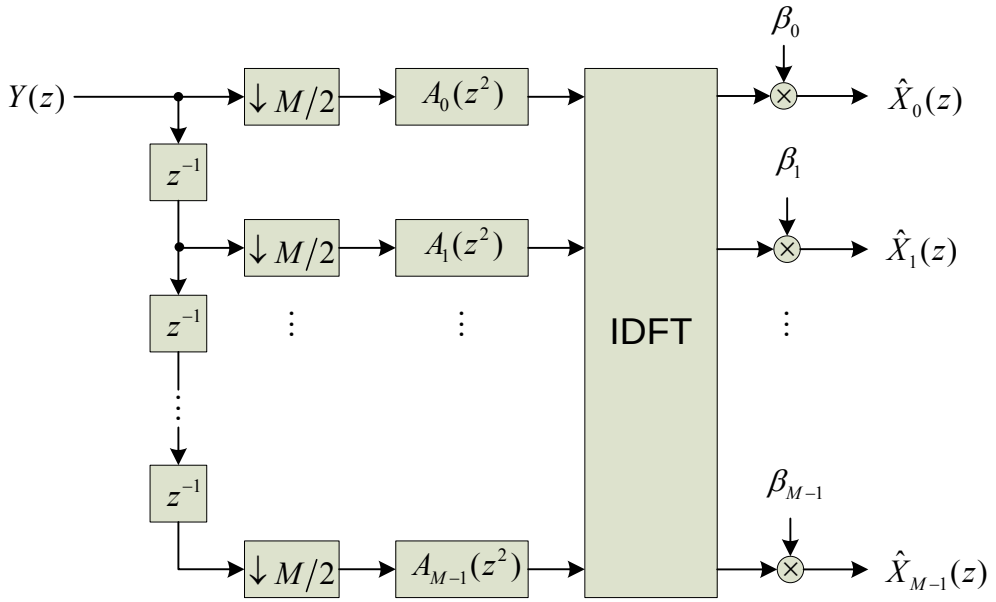

Figure 2-5: Efficient polyphase implementation of analysis filter bank.

2.2.3 Practical issues

DFT-based AFB

The IDFT-based AFB was very straightforward to derive but in order to provide better backward compatibility to OFDM, the AFB should be based on DFT. In this case, two additional modifications are needed. First, the delay chain and polyphase filters are flipped upside down. In addition, new multipliers $\hat{\beta}_k$ have to be defined is such a manner that the IDFT-based and DFT-based implementations provide the same subchannel signals.

In the IDFT-based structure, let us denote input samples to IDFT as x_k and AFB output samples as z_k, whereas the corresponding AFB output samples are $\tilde{z}_k$ in the DFT-based structure. Now the output samples can be written as

$$z_k = \Big(\sum_{n=0}^{M-1} \exp\Big(j\frac{2\pi kn}{M}\Big) \cdot x_n \Big) \beta_k \tag{14}$$

and

$$\begin{aligned} \tilde{z}_k &= \Big(\sum_{n=0}^{M-1} \exp\Big(-j\frac{2\pi kn}{M}\Big) \cdot x_{M-1-n} \Big) \hat{\beta}_k \\ &= \Big(\sum_{n=0}^{M-1} \exp\Big(-j\frac{2\pi k(M-1-n)}{M}\Big) \cdot x_n \Big) \hat{\beta}_k. \end{aligned} \tag{15}$$

In order to fulfill the requirement $\tilde{z}_k = z_k$, the following has to hold

$$\begin{aligned} \hat{\beta}_k &= \exp\Big(j\frac{2\pi kn}{M}\Big) \exp\Big(j\frac{2\pi k(M-1-n}{M}\Big) \beta_k \\ &= \exp\Big(-j\frac{2\pi k}{M}\Big) \beta_k \\ &= \exp\Big(-j\frac{2\pi k}{M}\Big(\frac{L_p+1}{2}\Big)\Big). \end{aligned} \tag{16}$$

The resulting DFT-based AFB is shown in Figure 2-6.

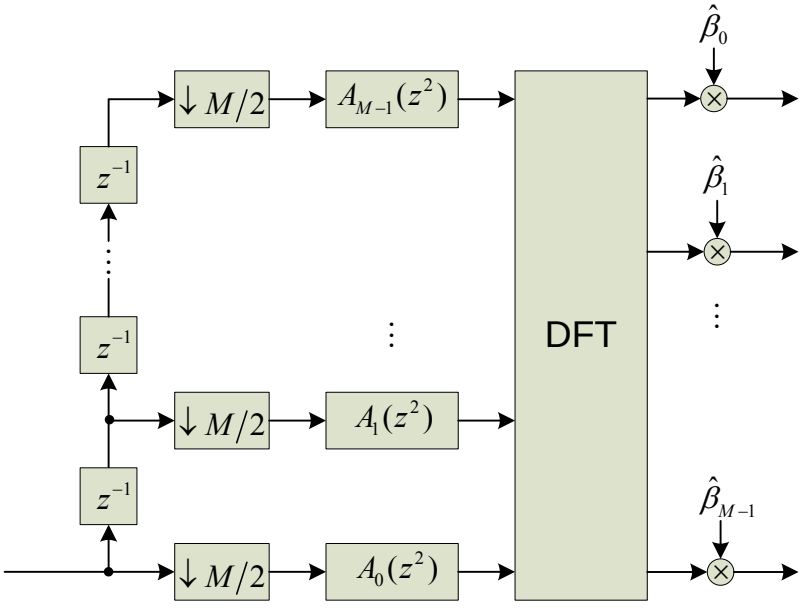

Figure 2-6: Efficient DFT-based implementation of analysis filter bank.

Subchannel processing

In the FBMC application, the use of critically sampled AFB would be problematic, since the aliasing effects would make it difficult to compensate imperfections of the transmission channel. Therefore, a factor of two oversampling is commonly applied in the subchannel processing sections. In the considered filter bank models, the useful data symbols are carried alternatingly by real and imaginary parts of the complex-valued subcarrier sequences. By using the whole complex samples in subchannel processing in the receiver, effectively 2x oversampling is obtained. At the end of the subchannel processing sections, the needed real/imaginary parts are selected to get a critically sampled sequence for detection.

It is also noticed that the signals with even numbered subchannels are nicely centered around zero frequency, i.e., they have a baseband format. On the other hand, the signals with odd numbered subchannels are centered around π. This would results in two different kinds of subchannel processing sections. However, it is possible to frequency shift all odd numbered subchannel signals around zero frequency by adding a simple extra term $(-1)^{kn}$ to both β_k- and $\hat{\beta}_k$-multipliers. In this manner, all subchannel processing sections can work using baseband signal format.

Implementation of extra delay

It was already mentioned that if the prototype filter length is $L_p = KM + 1 - D$ then an extra delay of z^{-D} has to be included into the TMUX configuration. This requirement comes from the fact that the center tap of the convolution between the impulse responses of the kth synthesis and analysis filters has to be situated on a sample index that is a multiple of $M/2$. In this manner, the resulting system delay is equal to $(L_p - 1)/(M/2)$. For example, the filter length of $L_p = KM - 1$ requires the extra delay of z^{-2}. There are several options how the required delay can be implemented and a couple of solutions are given here:

- The whole z^{-2} delay can be included into SFB output or AFB input.
- One z^{-1} delay can be easily included into the synthesis filter (and the other one into analysis filter) definition. Actually, this means that the first impulse response coefficient of the prototype filter can be set to be equal to zero:

$$\begin{aligned} z^{-1}G_k(z) &= \sum_{m=0}^{L_p-1} p[m] \exp\left(j\frac{2\pi k}{M}\left(m - \frac{L_p-1}{2}\right)\right) z^{-(m+1)} \\ &= \sum_{m=0}^{L_p+1} \tilde{p}[m] \exp\left(j\frac{2\pi k}{M}\left(m - 1 - \frac{L_p-1}{2}\right)\right) z^{-m} \\ &= \sum_{m=0}^{L_p+1} \tilde{p}[m] \exp\left(j\frac{2\pi k}{M}\left(m - \frac{L_p+1}{2}\right)\right) z^{-m}, \end{aligned}$$

  where $\tilde{p}[m] = [0\ p[m]\ 0]$ and L_p is the length of the original prototype filter. The last zero is included just that the new prototype filter is still a symmetric filter but in practical implementation it can be omitted.

The other z^{-1} delay can be included into AFB input. If the original delay chain and donwsamplers are considered to form the type-3 polyphase decomposition $y_l[m] = y[m\frac{M}{2} - l]$, then after the extra delay it has changed to the type-2 $\tilde{y}_l[m] = y[M - 1 - l + m\frac{M}{2} - M]$. The following example with $M = 4$ enlightens this modification

$$\begin{cases} y_0[m] = [y[0], y[2], y[4], \dots] \\ y_1[m] = [y[-1], y[1], y[3], \dots] \\ y_2[m] = [y[-2], y[0], y[2], \dots] \\ y_3[m] = [y[-3], y[-1], y[1], \dots] \end{cases}$$

$$\begin{cases} \tilde{y}_0[m] = [y[-1], y[1], y[3], \dots] \\ \tilde{y}_1[m] = [y[-2], y[0], y[2], \dots] \\ \tilde{y}_2[m] = [y[-3], y[-1], y[1], \dots] \\ \tilde{y}_3[m] = [y[-4], y[-2], y[0], \dots]. \end{cases}$$

It can be seen that the type-2 polyphase decomposition forms a conventional S/P conversion with overlapping of $M/2$.

2.3 Proposed implementation

The proposed filter bank structures to be used in the transmitter and receiver are shown in Figure 2-7 and Figure 2-8, respectively. Here, the main points are summarized:

OQAM pre-processing

- Input signals consist of complex-valued QAM symbols.
- The block C2R$_k$ denotes complex-to-real conversion, therefore $d_{k,n}$ is purely real-valued and its sampling rate is 2x higher than the input sampling rate.
- $\theta_{k,n} = \exp\left(j\frac{\pi}{2}(k+n)\right) = j^{(k+n)}$ leading to subchannel signals, where purely real-valued and imaginary-valued samples alternate and their order changes from one subchannel to the next.

Synthesis filter bank

- $\beta_{k,n} = (-1)^{kn} \exp\left(-j\frac{2\pi k}{M}\left(\frac{L_p-1}{2}\right)\right)$
  - $KM - 1$ length prototype filters: $L_p = KM + 1$ because the first impulse response coefficient is set to be zero (this models the required extra delay). Now $\beta_{k,n} = (-1)^{kn}(-1)^{kK}$
  - KM length prototype filters: $L_p = KM$. Now $\beta_{k,n} = (-1)^{kn}(-1)^{kK} \exp\left(j\frac{\pi k}{M}\right)$.
  - $KM + 1$ length prototype filters: $L_p = KM + 1$. Now $\beta_{k,n} = (-1)^{kn}(-1)^{kK}$
- Typically, the number of subchannels M is considered to be a power of two. In this case, IDFT can be replaced by inverse fast Fourier transform (IFFT) that can be efficiently realized using the Split-Radix algorithm [1].
- Type-1 polyphase filters are defined as $a_k[m] = p[k + mM]$.
- Upsamplers and delay chain form a P/S converter with overlapping of $M/2$.
- Output signal $s[m]$ is complex-valued.

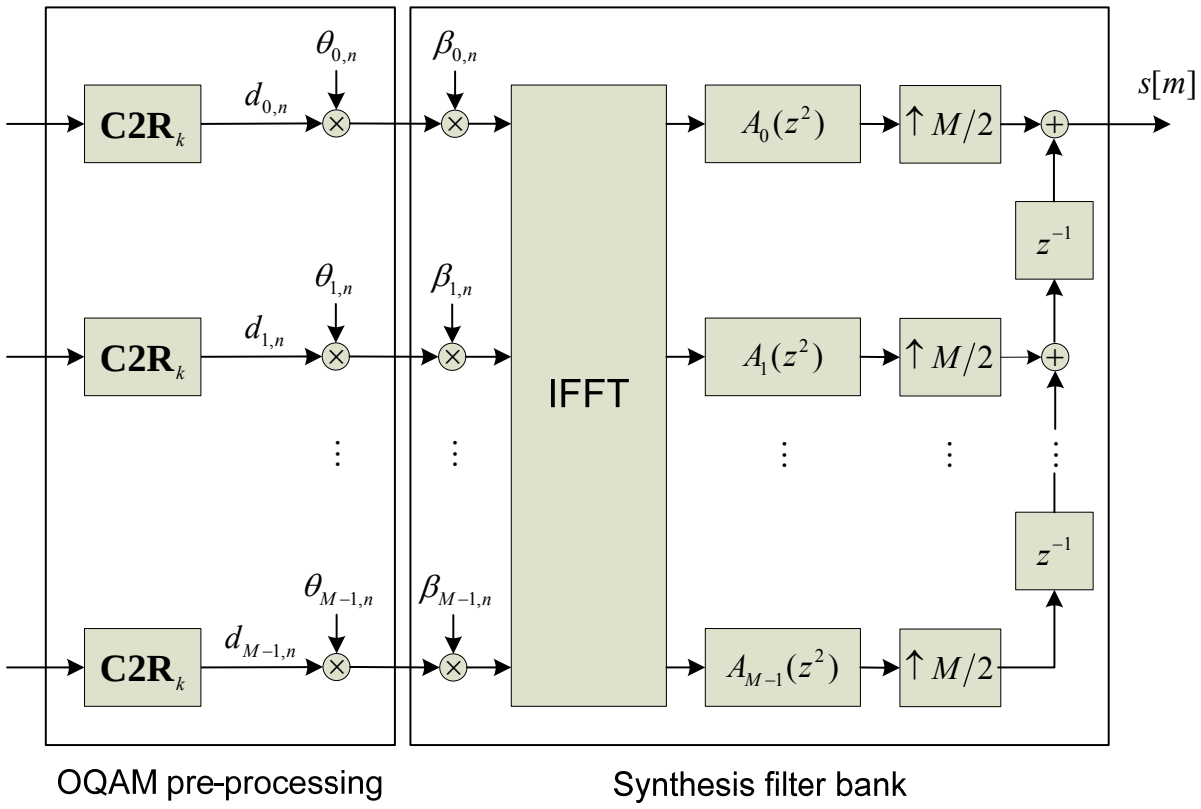

Figure 2-7: Proposed implementation of FBMC transmitter.

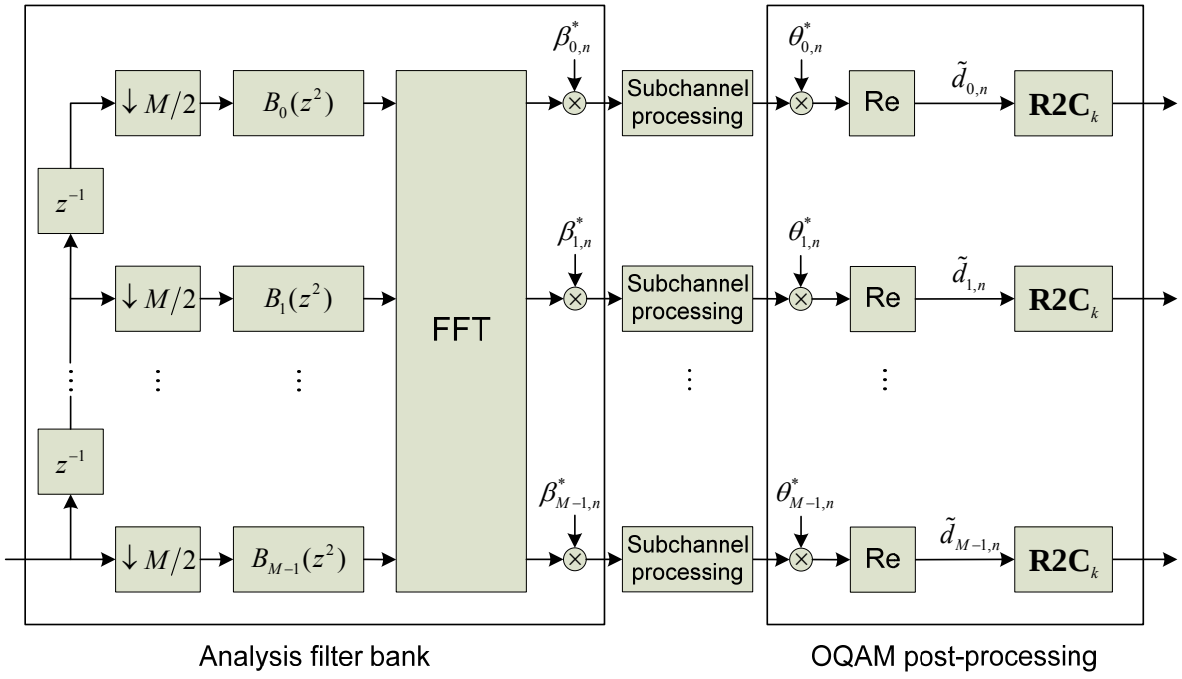

Figure 2-8: Proposed implementation of FBMC receiver.

Analysis filter bank

- Delay chain and downsamplers form a S/P converter with overlapping of $M/2$.
- Polyphase filters are defined as $b_k[m] = a_{M-1-k}[m] = p[M-1-k+mM]$ leading to type-2 representation.
- In typical scenario, DFT can be replaced by FFT. Additional multiplication by M is needed due to chosen prototype filter scaling.
- $\hat{\beta}_{k,n} = (-1)^{kn} \exp\left(-j\frac{2\pi k}{M}\left(\frac{L_p+1}{2}\right)\right)$
  - $KM-1$ length prototype filters: $L_p = KM-1$ because the required extra delay is merged to S/P converter. Now $\hat{\beta}_{k,n} = (-1)^{kn}(-1)^{kK} = \beta^*_{k,n}$
  - KM length prototype filters: $L_p = KM$ because the required extra delay is merged to S/P converter. Now $\hat{\beta}_{k,n} = (-1)^{kn}(-1)^{kK}\exp\left(-j\frac{\pi k}{M}\right) = \beta^*_{k,n}$.
  - $KM+1$ length prototype filters: $L_p = KM+1$ because there is no need for extra delays. Now $\hat{\beta}_{k,n} = (-1)^{kn}(-1)^{kK}\exp\left(-j\frac{2\pi k}{M}\right)$.

Subchannel processing

- Subchannel processing is done using complex-valued subchannel signals

OQAM post-processing

- $\theta^*_{k,n} = \exp\left(-j\frac{\pi}{2}(k+n)\right) = (-j)^{(k+n)}$ and after the Re-operation $\tilde{d}_{k,n}$ is purely real-valued.
- The block $R2C_k$ denotes real-to-complex conversion leading to complex-valued output signals and their sampling rates are 2x lower than before the conversion.

2.4 Computational complexity

The computational complexity of filter bank structures can be evaluated by calculating the number of real multiplications and additions that are necessary to compute a new length-M complex-valued output sequence. However, our analysis is just based on the number of multiplications because it is a known fact that adders are considerably cheaper to implement than multipliers.

The total number of real multiplications for SFB is the sum of the multiplications in each processing block; pre-processing, $\beta_{k,n}$-multipliers, M-point IFFT, and M-branch polyphase filter section, i.e.,

$$C_{SFB} = 2 \cdot \Big(M \cdot 2 + \big(M\big(\log_2(M) - 3\big) + 4\big) + KM \cdot 2 \Big). \tag{17}$$

Here, the pre-processing section is considered to be multiplication-free because it only consists of trivial multiplications by ± 1 and $\pm j$. The IFFT is assumed to be implemented using the Split-Radix algorithm [1]. Moreover, the first multiplication by 2 is because a complex-valued QAM symbol is separated into two OQAM symbols.

The complexity of AFB is equal to the complexity of SFB because similar processing blocks are used but in the reverse order. This results in the total complexity of the FBMC system

$$C_{FBMC} = C_{SFB} + C_{AFB} = 4 \cdot \Big(M \cdot 2 + \big(M \big(\log_2(M) - 3 \big) + 4 \big) + KM \cdot 2 \Big). \quad (18)$$

It should be noted that the complexity of $\beta_{k,n}$-multipliers can be omitted if the length of the prototype filter is $L_p = KM - 1$. From the implementation complexity point of view that filter length seems to be a very good choice.

The FBMC system (where $\beta_{k,n}$-multipliers are omitted) is compared with the OFDM system in terms of the number of real multiplications in Figure 2-9. From the filter bank point of view, we recall that the OFDM only consists of IFFT and FFT, i.e., its complexity can be written as

$$C_{OFDM} = 2 \cdot \big(M \big(\log_2(M) - 3 \big) + 4 \big). \quad (19)$$

It can be seen that the FBMC is approximately 10 times more complex than the conventional OFDM. It can also be noticed that the computational complexity of FBMC depends only slightly on the overlapping factor K.

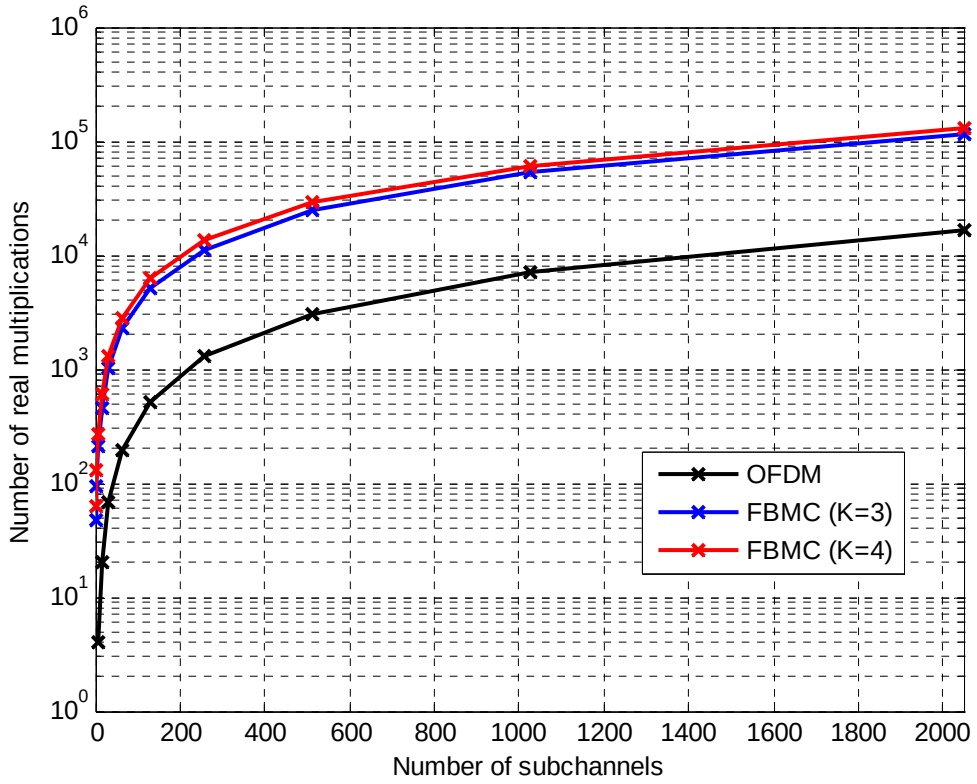

Figure 2-9: Number of real multiplications as a function of number of subchannels in the case of OFDM and FBMB.

2.5 Connection to other filter bank structures

The proposed TMUX configuration is not the only option. The exponentially modulated filter bank (EMFB)-based TMUX can be also used instead of our FBMC/OQAM system. There are two main differences: EMFB is an odd-stacked filter bank and low-rate SFB input signals are purely real-valued. In addition, critically sampled EMFB has an efficient implementation that is based on CMFB and SMFB. Especially, PR filter banks can be efficiently implemented using ELT-type of structures [1]. Here, only the basic idea of EMFBs is given, but more detailed information can be found from [14].

Basically, EMFB can be considered to be a complex extension of the ELT, so the synthesis and analysis filters are generated from a linear-phase lowpass FIR prototype filter by using complex exponential modulation sequences as follows

$$g_k^e[m] = \sqrt{\frac{4}{M}} h_p[m] \exp\left(j\frac{2\pi}{M}\left(k+\frac{1}{2}\right)\left(m+\frac{M/2+1}{2}\right)\right)$$

$$f_k^e[m] = \frac{1}{2}\sqrt{\frac{4}{M}} h_p[m] \exp\left(-j\frac{2\pi}{M}\left(k+\frac{1}{2}\right)\left(N-m+\frac{M/2+1}{2}\right)\right), \tag{20}$$

where $k = 0, 1, \ldots, M-1$ and $m = 0, 1, \ldots, L_p - 1$. Due to modulation, all subchannel filters are linear-phase filters and their impulse responses are purely complex-valued.

The key idea behind the efficient implementation of the critically sampled EMFB system is that the EMFB channel filters can be represented using cosine and sine modulated channel filters as follows

$$g_k^e[m] = \begin{cases} \left(g_k^c[m] + j g_k^s[m]\right), & k \in [0, M/2-1] \\ -\left(g_{M-1-k}^c[m] - j g_{M-1-k}^s[m]\right), & k \in [M/2, M-1] \end{cases} \tag{21}$$

$$f_k^e[m] = \begin{cases} \frac{1}{2}\left(f_k^c[m] - j f_k^s[m]\right), & k \in [0, M/2-1] \\ -\frac{1}{2}\left(f_{M-1-k}^c[m] + j f_{M-1-k}^s[m]\right), & k \in [M/2, M-1], \end{cases} \tag{22}$$

where the superscripts c and s denote cosine modulated and sine modulated, respectively. These definitions enable the efficient implementation of AFB because real-valued suchannel signals can be simplified according to

$$\begin{aligned} \hat{X}_k(z) &= \mathrm{Re}\Big([Y_I(z) + j \cdot Y_Q(z)][F_k^c(z) - j \cdot F_k^s(z)]\Big) \\ &= \mathrm{Re}\Big(Y_I(z)F_k^c(z) + Y_Q(z)F_k^s(z) + j \cdot [Y_Q(z)F_k^c(z) - Y_I(z)F_k^s(z)]\Big) \\ &= Y_I(z)F_k^c(z) + Y_Q(z)F_k^s(z) \end{aligned}$$

and

$$\begin{aligned}\hat{X}_{M-1-k}(z) &= \mathrm{Re}\Big([Y_I(z)+j\cdot Y_Q(z)][-F_k^c(z)-j\cdot F_k^s(z)]\Big)\\ &= \mathrm{Re}\Big(-Y_I(z)F_k^c(z)+Y_Q(z)F_k^s(z)-j\cdot[Y_Q(z)F_k^c(z)+Y_I(z)F_k^s(z)]\Big)\\ &= -Y_I(z)F_k^c(z)+Y_Q(z)F_k^s(z).\end{aligned}$$

Figure 2-10 describes the EMFB-based TMUX configuration. It has real-valued low-rate signals and complex-valued I/Q presentation for high-rate channel signal. The TMUX itself is realized efficiently using cosine and sine modulated filter bank blocks. The analysis bank can efficiently include the operation of taking the real part of the signal after the complex-valued subchannel filtering, whereas the synthesis bank implements the complex-valued subchannel filters with real-valued input signals. However, the analysis part should implement complex-valued output signals instead of real-valued ones for subchannel processing. This can be obtained by duplicating the analysis bank blocks (both I and Q signals are processed using CMFB and SMFB, so totally two CMFB and two SMFB blocks are needed). In this manner, 2x oversampled subchannel signals can be provided for the subchannel processing purposes. Alternative method to implement 2x oversampled AFB is presented in [15], where the filter bank structure is an efficient DFT-based realization.

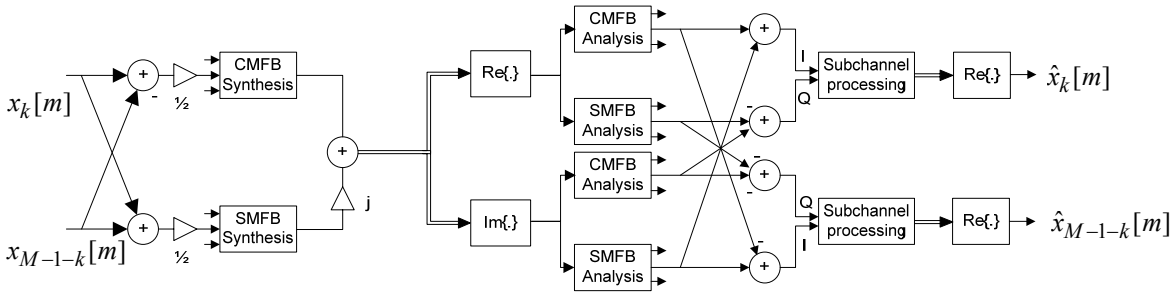

Figure 2-10: EMFB-based TMUX configuration.

As a conclusion, EMFB-based TMUX is very closely related to FBMC/OQAM. Also an IFFT/FFT-based implementation of EMFB has been reported in [15], and it shows even higher degree of commonality with the selected FBMC approach. The main difference is a half subchannel offset in the used subchannel stacking arrangement. Moreover, low-rate signals are purely real-valued, leading to a somewhat simplified alternative signal model, which could be beneficial, e.g., in some analytical studies.

3 Prototype filter

The prototype filter is a key element in the complex modulated filter banks because all synthesis and analysis filters are frequency shifted versions of the corresponding lowpass prototype filter frequency response. In this sense, the quality of filter bank system depends mainly on the properties of the prototype filter. In PHYDYAS project, the prototype filter is selected to be a causal real-valued symmetric FIR filter with high frequency selectivity.

The prototype filter can be designed to fulfill PR conditions or to provide NPR characteristics. In the PR case, the resulting prototype filter is typically a spectral factor of an Mth-band (Nyquist) filter. However, it is worth emphasizing that the PR property is exactly obtained only in the case of ideal transmission channel. In our case, the PR conditions are not essential because it is sufficient that filter bank structure based interferences are small enough compared to the residual interferences due to transmission channel. Moreover, NPR designs are more efficient than PR designs, e.g., in providing higher stopband attenuation with given prototype filter length.

The initial prototype filter of our project has been designed using so-called frequency sampling technique [16]. The impulse response coefficients of the prototype filter can be expressed using the following closed-form representation:

$$p[m] = \bar{P}[0] + 2\sum_{k=1}^{K-1}(-1)^k \bar{P}[k]\cos\left(\frac{2\pi k}{KM}(m+1)\right), \tag{23}$$

where

$$\begin{aligned} m &= 0, 1, \ldots, KM-2 \\ K &= 4 \\ \bar{P}[0] &= 1 \\ \bar{P}[1] &= 0.97195983 \\ \bar{P}[2] &= 1/\sqrt{2} \\ \bar{P}[3] &= \sqrt{1-\bar{P}[1]} = 0.23514695. \end{aligned}$$

Those $\bar{P}[k]$ coefficients do not depend on the filter length, thus, this approach is scalable. The magnitude response of the initial prototype filter is shown Figure 3-1. In this figure, the subchannel spacing Δf is taken as unity ($\Delta f = 1$). It is important to notice that the stopband attenuation exceeds 60 dB for the frequency range above 2 subchannel spacings.

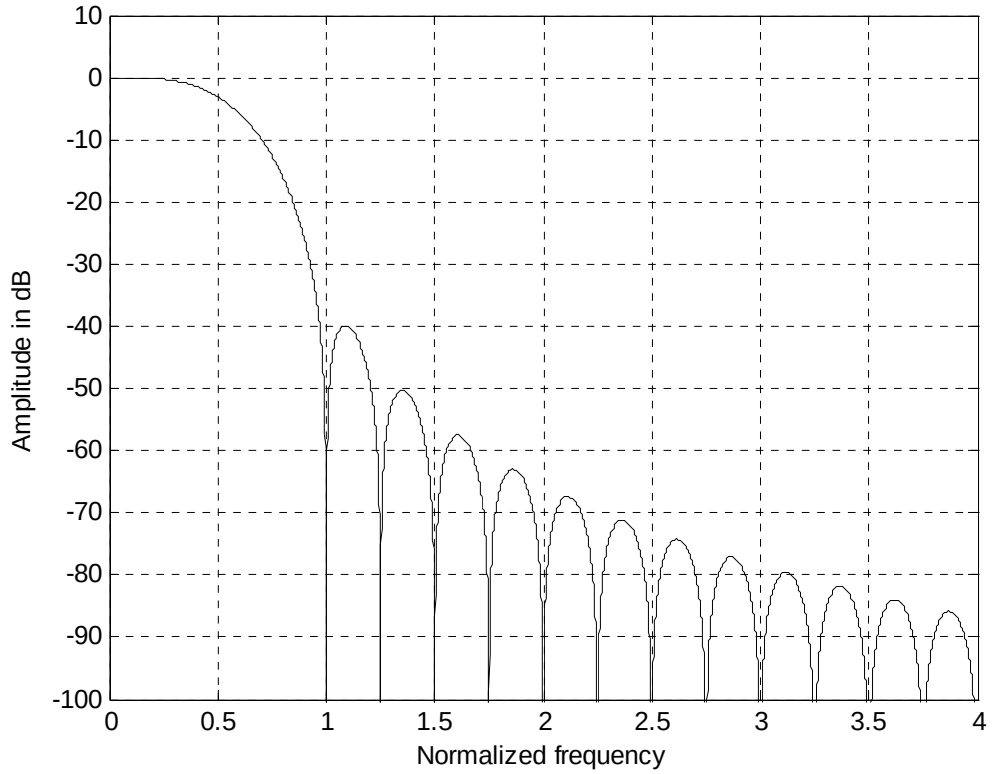

Figure 3-1: Magnitude response of the initial prototype filter.

3.1 Design techniques

There exist plenty of different techniques to design complex modulated filter banks. A reason is that CMFB design techniques are also applicable because the prototype filter for an $M/2$-subchannel CMFB can be used for M-subchannel complex modulated filter banks [17]. In the case of PR filter banks, the linear-phase prototype filter of length KM can be represented using special lattice rotation or butterfly angles instead of filter coefficients [18][19]. In this manner, the PR constraints are automatically satisfied and the number of unknowns is reduced. Further simplifications, in terms of number of unknowns, can be obtained when lattice rotation angles are approximated by polynomial functions [20][21]. Unfortunately, these techniques are not applicable for NPR filter banks.

A straightforward way to design NPR prototype filters is to directly optimize the impulse response coefficients. Naturally, the efficiency of the design process depends highly on the size of the problem. For example, the number of unknowns (filter coefficients) increases dramatically when designing frequency selective filter banks with high number of subchannels ($M \geq 128$). However, iterative methods such as [22], which make certain approximations to the optimization problem, can lead to acceptable solution. In addition to the traditional approaches, design methods based on frequency-response masking (FRM) technique have been used in [23]. In this way, the number of optimized parameters can be drastically decreased. On the other hand, FRM technique is not so straightforward because prototype filter is realized with the aid of three subfilters (model and masking filters). Therefore, FRM technique is not considered here.

We are interested in NPR design techniques that can reduce the number of unknowns. In other words, the prototype filter coefficients should be given using a closed-form representation that includes only a few adjustable design parameters. The same closed-form representation would be valid for all values of M resulting in the scalability property. Therefore, we mainly concentrate on frequency sampling technique and windowing based techniques.

3.1.1 Frequency sampling technique

The idea of frequency sampling technique is actually very simple. The closed-form representation of a L_p-length prototype filter $p[m]$ is based on the use of pre-defined coefficients (magnitude values) that weight specific cosine terms. Slightly different representations can be derived depending on the relation between filter length L_p and number of frequency points Q:

$Q = L_p + 1$:

$$p[m] = \frac{1}{Q}\left(\bar{P}[0] + 2\sum_{k=1}^{U}(-1)^k \bar{P}[k]\cos\left(\frac{2\pi k}{Q}\left(m+1\right)\right)\right) \text{ for } U = \begin{cases} \frac{L_p}{2}, & L_p \text{ even} \\ \frac{L_p-1}{2}, & L_p \text{ odd} \end{cases} \tag{24}$$

$Q = L_p$:

$$p[m] = \frac{1}{Q}\left(\bar{P}[0] + 2\sum_{k=1}^{U}(-1)^k \bar{P}[k]\cos\left(\frac{2\pi k}{Q}\left(m+\frac{1}{2}\right)\right)\right)) \text{ for } U = \begin{cases} \frac{L_p}{2}-1, & L_p \text{ even} \\ \frac{L_p-1}{2}, & L_p \text{ odd} \end{cases} \tag{25}$$

$Q = L_p - 1$:

$$p[m] = \frac{1}{Q}\left(\bar{P}[0] + 2\sum_{k=1}^{U}(-1)^k \bar{P}[k]\cos\left(\frac{2\pi k}{Q}m\right)\right)) \text{ for } U = \begin{cases} \frac{L_p}{2}-1, & L_p \text{ even} \\ \frac{L_p-1}{2}-1, & L_p \text{ odd} \end{cases} \tag{26}$$

with

$$p[0] = p[L_p - 1] = \frac{1}{2Q}\left(\bar{P}[0] + \sum_{k=1}^{U}(-1)^k \bar{P}[k]\right)) \text{ for } U = \begin{cases} \frac{L_p}{2}-1, & L_p \text{ even} \\ \frac{L_p-1}{2}-1, & L_p \text{ odd.} \end{cases} \tag{27}$$

The above equations are quite simple to derive. If the frequency response of a prototype filter is defined as follows

$$P(e^{j\omega}) = \sum_{m=0}^{L_p-1} p[m]e^{-j\omega m} \tag{28}$$

then the impulse response coefficients of this prototype filter can be calculated as

$$p[m] = \frac{1}{Q}\sum_{k=0}^{Q-1} P(e^{j\omega_k})e^{j\omega_k m} \text{ for } m = 0, 1, \ldots, L_p - 1. \tag{29}$$

The above relation is evident when considering Q point frequency grid ($Q \geq L_p$) and writing Eq. (28) using matrix representation and solving $p[m]$, i.e., $\mathbf{P} = \mathbf{W}\mathbf{p} \Leftrightarrow \mathbf{p} = \frac{1}{Q}\mathbf{W}^{-1}\mathbf{P}$.

A slightly different case is $Q = L_p - 1$ then

$$p[m] = \frac{1}{Q}\sum_{k=0}^{Q-1} P(e^{j\omega_k})e^{j\omega_k m} \text{ for } m = 1, 2, \ldots, L_p - 2 \tag{30}$$

and

$$p[0] + p[L_p - 1] = \frac{1}{Q}\sum_{k=0}^{Q-1} P(e^{j\omega_k}). \tag{31}$$

The required frequency response at the point ω_k is

$$\begin{aligned} P(e^{j\omega_k}) &= \sum_{m=0}^{L_p-1} p[n]e^{-j\omega_k m} \\ &= \begin{cases} e^{-j\omega_k \frac{L_p-1}{2}} \sum_{m=0}^{\frac{L_p}{2}-1} p[m] 2\cos\left(\omega_k\left(\frac{L_p-1}{2} - m\right)\right), & L_p \text{ even} \\ e^{-j\omega_k \frac{L_p-1}{2}} \left(\sum_{m=0}^{\frac{L_p-1}{2}-1} p[m] 2\cos\left(\omega_k\left(\frac{L_p-1}{2} - m\right)\right) + p[\frac{L_p-1}{2}]\right), & L_p \text{ odd} \end{cases} \\ &= \bar{P}[k]e^{j\Theta(k)}, \end{aligned} \tag{32}$$

where $\bar{P}[k]$ and $\Theta(k)$ stand for the magnitude and phase, respectively. Here, the linear-phase property, $p[m] = p[L_p - 1 - m]$, where $m = 0, 1, \ldots, \frac{L_p}{2} - 1$ for L_p even and $m = 0, 1, \ldots, \frac{L_p-1}{2} - 1$ for L_p odd, was used.

To yield real-valued filter coefficients, $\bar{P}[k]$ has to be symmetric, i.e., $\bar{P}[k] = \bar{P}[Q - k]$ for $k = 1, 2, \ldots, Q - 1$. Now we can calculate the filter coefficients by assuming equally spaced frequency grid $\omega_k = \frac{2\pi k}{Q}$:

$$\begin{aligned} p[m] &= \frac{1}{Q}\sum_{k=0}^{Q-1} \bar{P}[k]e^{j\Theta(k)}e^{j\omega_k m} \\ &= \frac{1}{Q}\sum_{k=0}^{Q-1} \bar{P}[k]e^{j\frac{2\pi k}{Q}\left(n - \frac{L_p-1}{2}\right)}. \end{aligned} \tag{33}$$

After some mathematical manipulation, the close-form representations can be derived. In the case of initial prototype filter, the desired magnitude response values that differ from zero values were given.

3.1.2 Windowing based techniques

In order to be able to generate a L_p-length prototype filter $p[m]$ using the windowing method, the impulse response of a causal ideal lowpass filter $p_{id}[m]$ with cut-off frequency ω_c has to be multiplied by a specific window function $w[m]$, i.e.,

$$p[m] = w[m]p_{id}[m], \tag{34}$$

where

$$p_{id}[m] = \begin{cases} \sin\left(\frac{\omega_c(m-(L_p-1)/2)}{\pi(m-(L_p-1)/2))}\right), & 0 \le m \le L_p - 1 \\ 0, & \text{otherwise} \end{cases} \tag{35}$$

and $w[m]$ is a four-term generalized cosine window function given by

$$w[m] = \sum_{k=0}^{3} (-1)^k A_k \cos\left(\frac{2\pi km}{L_p - 1}\right), \tag{36}$$

where A_k values are the weights of each cosine term [24]. Without loss of generality, this generalized window function is normalized according to

$$\sum_{k=0}^{3} A_k = 1. \tag{37}$$

This condition reduces the number of optimized parameters by one. Therefore, the parameter vector contains only four adjustable terms, namely, three weights of the generalized cosine window and the cut-off frequency of the ideal lowpass filter. The A_k coefficients are independent of the filter length and the number of subchannels, whereas the cut-off frequency depends on the number of subchannels. However, this approach is scalable.

It should be also noticed that $w[m]$ can be some pre-defined window function, such as Hann ($A_0 = 0.5$ and $A_1 = 0.5$), Hamming ($A_0 = 0.54$ and $A_1 = 0.46$), Blackman ($A_0 = 0.42$, $A_1 = 0.5$, and $A_1 = 0.08$), or Kaiser (defined using the zeroth order Bessel function) window. The first three are fixed windows so the only parameter to be optimized is the cut-off frequency of the ideal lowpass filter. The last one is an adjustable window that gives one extra parameter for the design process.

3.2 Optimization

The purpose of the optimization is to find prototype filter coefficients or other adjustable parameters that can be defined as optimal according to certain design criteria. The given design parameters are usually: number of channels M, filter length L_p, passband edge ω_p, stopband edge ω_s, and allowable filter bank structure based distortions. In a general case, there is an objective function that has to be minimized or maximized subject to constraints in the form of equality constraints and/or inequality constraints. This general formulation can be referred to as constrained optimization

problem. This is not the only option because the optimization problem could be modified in such a manner that there are no constraints. This results in an unconstrained optimization problem.

An efficient and accurate solution to the optimization problem depends on the size of the problem in terms of the number of filter dependant unknowns, but also on characteristics of the objective function and possible constraints. Typically, the objective function and constraints are highly nonlinear with respect to the unknown parameters. These strong nonlinearities imply that the optimization problems are computationally complex, time-consuming, very sensitive to initial values, and have a slow convergence. Moreover, the global optimality is not guaranteed, because the solution can be easily trapped in a local minimum.

3.2.1 Design criteria

In order to obtain frequency selective filters, it is very typical to define the objective function using frequency-domain specifications. For this purpose the magnitude response of the real-valued prototype filter is divided into three types of regions: the passband region is $[0, \omega_p]$, the stopband region is $[\omega_s, \pi]$, and the gap between these two is called as the transition band. The band edges can be given as follows $\omega_p = \frac{(1-\alpha)\pi}{M}$ and $\omega_s = \frac{(1+\alpha)\pi}{M}$, where α is the roll-off factor that defines how much adjacent subchannels are overlapping. A typical choice is $\alpha = 1.0$, which means that the transition bands of a subchannel end at the centers of the adjacent subchannels. This means that only immediately adjacent subchannels are significantly interacting with each other. Furthermore, in many cases, the constraints imposed by the problem automatically shape the passband region and only the stopband region is taken into account in the objective function. Three well-known design criteria are least-squares (LS), minimax, and peak-constrained least-squares (PCLS) criteria.

- The goal of the LS criterion is to minimize the stopband energy of the prototype filter. The objective function can be written as follows

$$F(\mathbf{x}) = \int_{\omega_s}^{\pi} |P(e^{j\omega})|^2 d\omega. \tag{38}$$

  The magnitude response of the resulting filter is shaped in such a manner that the attenuation increases steadily when going further from the stopband edge. The attenuation is rather low at the stopband edge, but it increases very rapidly to the level of the first stopband ripple.

- The goal of the minimax criterion is to minimize the maximum stopband ripple instead of the stopband energy. In minimax design, the objective function is

$$F(\mathbf{x}) = \max_{\omega \in [\omega_s, \pi]} |P(e^{j\omega})|. \tag{39}$$

  The magnitude response of the resulting filter is shaped in such a manner that the attenuation is equiripple on the overall stopband region. The attenuation at the stopband edge is much higher than in the case of LS criterion, but this results in significantly increased total stopband energy.

- The PCLS criterion offers a trade-off between the LS and minimax criteria. The objective function is the stopband energy subject to maximum stopband ripple that is less than or equal to some prescribed value δ, i.e.,

$$F(\mathbf{x}) = \int_{\omega_s}^{\pi} |P(e^{j\omega})|^2 d\omega \quad \text{subject to } |P(e^{j\omega})| \leq \delta \quad \text{for } \omega \in [\omega_s, \pi]. \tag{40}$$

  If δ is large enough, then this criterion reduces to the LS criterion. When decreasing δ, this criterion approaches the minimax criterion. Logically, this additional constraint increases total stopband energy.

In this report, LS, minimax, and PCLS design criteria are used for the prototype filter optimization. Moreover, the applicability of each criterion is analyzed.

3.2.2 Constraints

Naturally, the optimization constraints depend highly on the application. In the case of multicarrier systems, maximum allowable filter bank structure based interferences are typical choices. Here, the terms ISI and ICI are usually introduced. They can be measured by forming the input-output relation of the corresponding FBMC system. In the case of OQAM, it is advantageous to include θ_k, θ_k^*, Re-operation to the TMUX configuration, i.e., the considered input and output signals are purely real-valued. This simplifies the analysis considerably.

The transfer functions between real-valued input and output signals can be collected together using matrix notations as follows

$$\mathbf{X}(z^{M/2}) = \mathbf{T}_{TMUX}(z^{M/2}) \cdot \hat{\mathbf{X}}(z^{M/2}), \tag{41}$$

where

$$\mathbf{X}(z) = \begin{bmatrix} X_0(z) & X_1(z) & \cdots & X_{M-1}(z) \end{bmatrix}^T \tag{42}$$

$$\hat{\mathbf{X}}(z) = \begin{bmatrix} \hat{X}_0(z) & \hat{X}_1(z) & \cdots & \hat{X}_{M-1}(z) \end{bmatrix}^T. \tag{43}$$

The matrix $\mathbf{T}_{TMUX}(z^{M/2})$ is the transfer matrix and its element $\left[\mathbf{T}_{TMUX}(z^{M/2})\right]_{a,b}$ represents the relation between input signal $\mathbf{X}_a(z^{M/2})$ and the output signal $\hat{\mathbf{X}}_a(z^{M/2})$. The elements in the main diagonal are the transfer functions of the subchannels of the TMUX system and other elements describe the crosstalk between different subchannels.

The power of the total interference due to structure based ISI and ICI components can be estimated for example by using the following formula

$$\text{TOI} = \text{ISI} + \text{ICI}, \tag{44}$$

where

$$\mathrm{ISI} = \max_k \Big(\sum_n \left([\mathbf{T}_{TMUX}(n)]_{k,k} - \delta(n-\Delta) \right)^2 \Big) \tag{45}$$

and

$$\mathrm{ICI} = \max_k \Big(\sum_{l=0, l\neq k}^{M-1} \sum_n \left([\boldsymbol{T}_{TMUX}(n)]_{k,l} \right)^2 \Big), \tag{46}$$

where $\delta(n)$ is the ideal impulse and Δ is the delay of TMUX system. In the case of FBMC/OQAM, crosstalk terms $\left[\mathbf{T}_{TMUX}(z^{M/2})\right]_{a,b} = 0$ if $a+b$ is odd. This is a filter bank structure based property and it means that every other crosstalk term is equal to zero. In addition, it has been noticed that similar terms exist in every row. These properties simplify the calculation of interference components.

In the NPR case, prototype filter can be optimized in such a manner that the total interference is below some pre-defined level. Another option is to do the optimization just based on the maximum ISI (ICI) level and then analyze the resulting ICI (ISI) level. It should be also mentioned that the total interference or interference components can be used as an optimization criterion.

3.3 Optimization results

In this section, new prototype filters are generated with the aid of optimization. Here, three different filter lengths $L_p = \{KM-1, KM, KM+1\}$ are considered. The most interesting overlapping factors are $K = \{3,4,5\}$ and the number of subchannels is selected to be $M = 64$. Although optimum prototype filters seem to be slightly dependent on the number of subchannels, it is quite safe to draw conclusions based on the presented results. If the presented optimization techniques cannot improve the characteristics of the initial prototype filter for $M = 64$ then they cannot provide improvements for $M = 1024$ either.

The prototype filters are optimized using four different design methods:

- frequency sampling technique (D1)
- windowing based techniques (D2)
- direct optimization of filter coefficients (D3).

For each method, we use the following optimization criteria:

- LS criterion (C1)
- minimax criterion (C2)
- PCLS criterion (C3)
- total filter bank structure based interference (C4).

Here, optimized prototype filters are analyzed based on three performance metrics:

- total filter bank structure based interference (TOI)
- minimum stopband attenuation (MSA)
- level of highest stopband ripple (HSR).

It is very likely that the presented prototype filters can be further improved because other initial parameters could lead to better local optimum or even to the global optimum solution. However, the general trend can be observed from the following results.

3.3.1 Frequency sampling technique

In this method, the prototype filter is defined according to

$$p[m] = \bar{P}[0] + 2\sum_{k=1}^{U}(-1)^k \bar{P}[k]\cos\left(\frac{2\pi k}{KM}\left(m + \frac{KM-(L_p-1)}{2}\right)\right), \quad m = 0, 1, \ldots, L_p - 1.$$

Now the aim is to find out the coefficients $\bar{P}[k]$ ($k = 0, 1, \ldots, K-1$) in such a manner that the selected optimization criterion is minimized. The rest of the coefficients are set be $\bar{P}[k] = 0$ ($k = K, K+1, \ldots, U$) in order to provide continuously decreasing stopband attenuation. In addition, it is also shown in [9] that there should be a specific relationship between certain magnitude values, i.e., $\bar{P}[0] = 1$ and $\bar{P}[l]^2 + \bar{P}[K-l]^2 = 1$ for $l = 1, 2, \ldots, \lfloor K/2 \rfloor$. This means that there are only one or two freely adjustable parameters (x, y):

- $K = 3$: $\bar{P}[0] = 1$, $\bar{P}[1] = x$, $\bar{P}[2] = \sqrt{1-x^2}$
- $K = 4$: $\bar{P}[0] = 1$, $\bar{P}[1] = x$, $\bar{P}[2] = 1/\sqrt{2}$, $\bar{P}[3] = \sqrt{1-x^2}$
- $K = 5$: $\bar{P}[0] = 1$, $\bar{P}[1] = x$, $\bar{P}[2] = y$, $\bar{P}[3] = \sqrt{1-y^2}$, $\bar{P}[4] = \sqrt{1-x^2}$.

Therefore, we can easily do global search to track down the global optimum for example in terms of total interference. Figure 3-2 shows the resulting levels of TOI and MSA. In the case of $K = 5$, the other adjustable parameter was experimentally chosen as $y = 0.88101964$. It can be seen that global optimums are very easy to find. Moreover, different kind of trade-offs can be made by selecting different x value. For example, in the case of the initial prototype ($\mathrm{TOI} = -65.2$, $\mathrm{MSA} = -39.8$, and $\mathrm{HSR} = -39.8$) by slightly increasing $\bar{P}[1] = 0.97195983 + 0.0008$ and decreasing the corresponding $\bar{P}[3]$, the resulting prototype filter has the following properties: $\mathrm{TOI} = -63.9$, $\mathrm{MSA} = -40.4$, and $\mathrm{HSR} = -40.4$. As can be seen from Figure 3-3, the attenuation of subchannel with index $i+2$ is significantly increased. The counterpart is a reduced attenuation for the subchannels with indices $i > 3$. However, this attenuation is kept well below 80 dB.

It has been also noticed that by increasing the filter length from $L_p = KM - 1$ to $L_p = KM$ or $L_p = KM + 1$ the improvement of TOI and MSA levels are very small (only fractions of decibels).

Next, it is demonstrated the effect of optimization to the stopband behavior of the prototype filter. Wisely chosen random values have been used as initial values for the optimization. Figure 3-4, Figure 3-5, and Figure 3-6 show the magnitude responses of the prototype filters obtained using optimization criteria C1-C4 and the corresponding optimum values are given in Table 3-1. In addition, the resulting levels of TOI, MSA, and HSR are summarized in
Table 3-2.

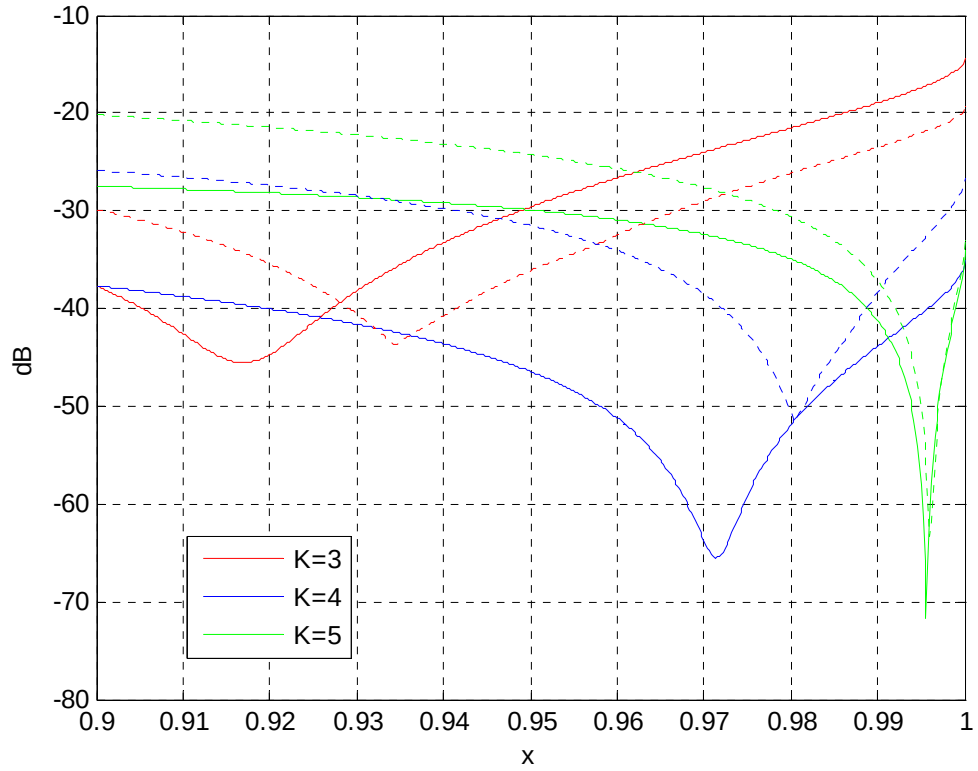

Figure 3-2: The level of TOI (solid line) and MSA (dotted line) in the case of $K = \{3, 4, 5\}$, $M = 64$ and $L_p = KM - 1$.

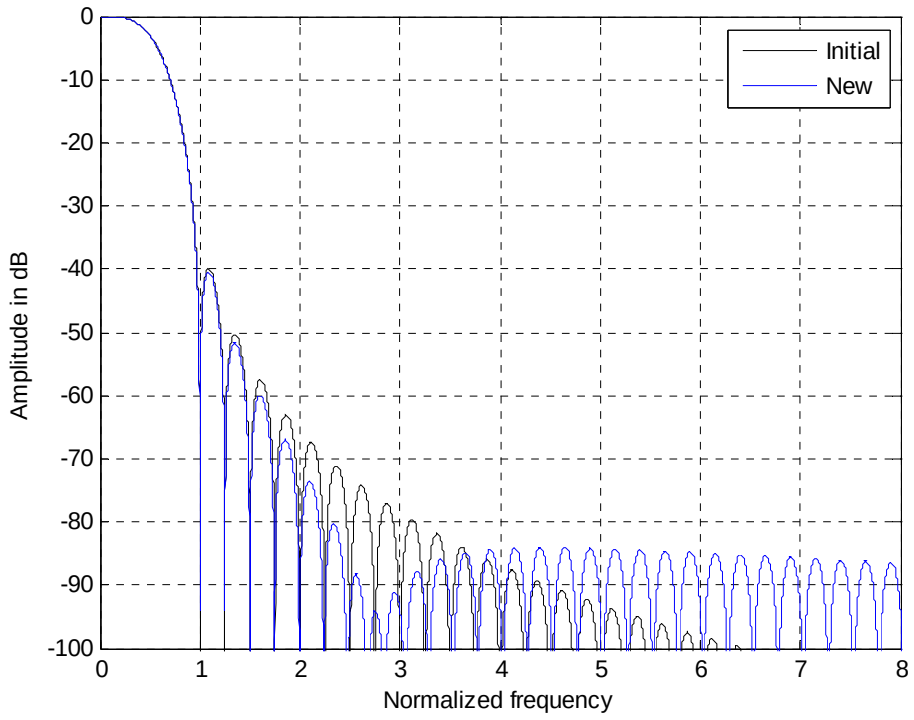

Figure 3-3: Magnitude responses of the initial and a slightly modified version of the initial prototype filter in the case of $K = 4$, $M = 64$, and $L_p = 255$.

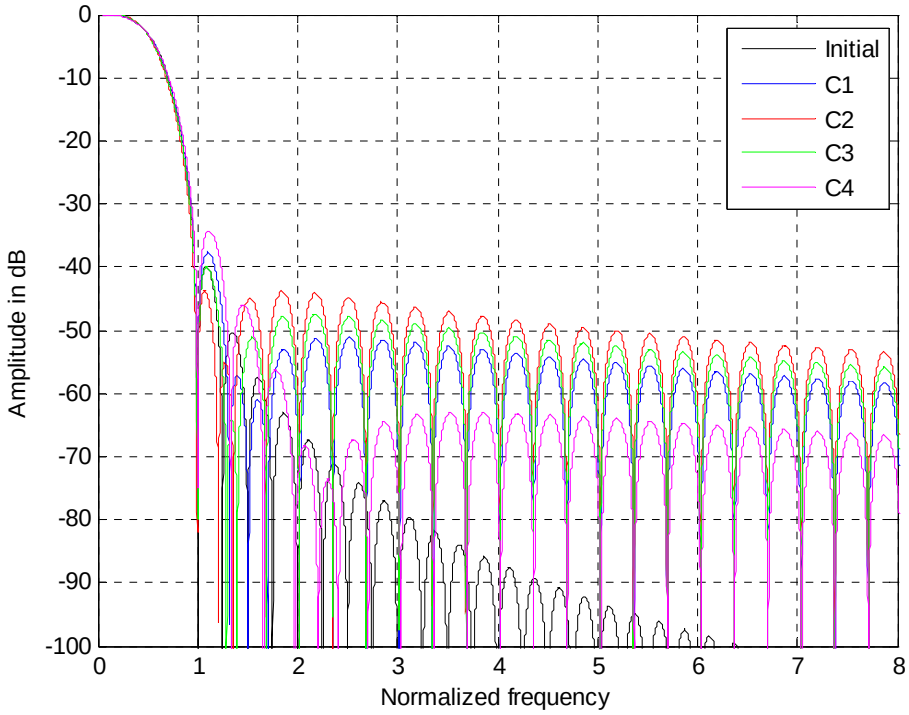

Figure 3-4: Magnitude responses of prototype filters in the case of $K = 3$, $M = 64$, and $L_p = 191$.

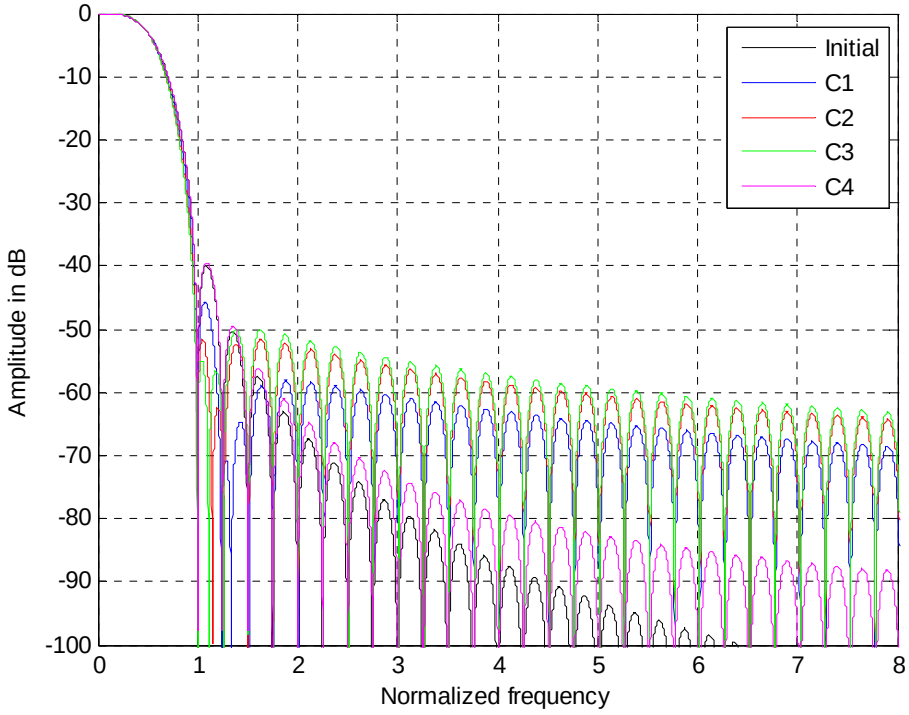

Figure 3-5: Magnitude responses of prototype filters in the case of $K = 4$, $M = 64$, and $L_p = 255$.

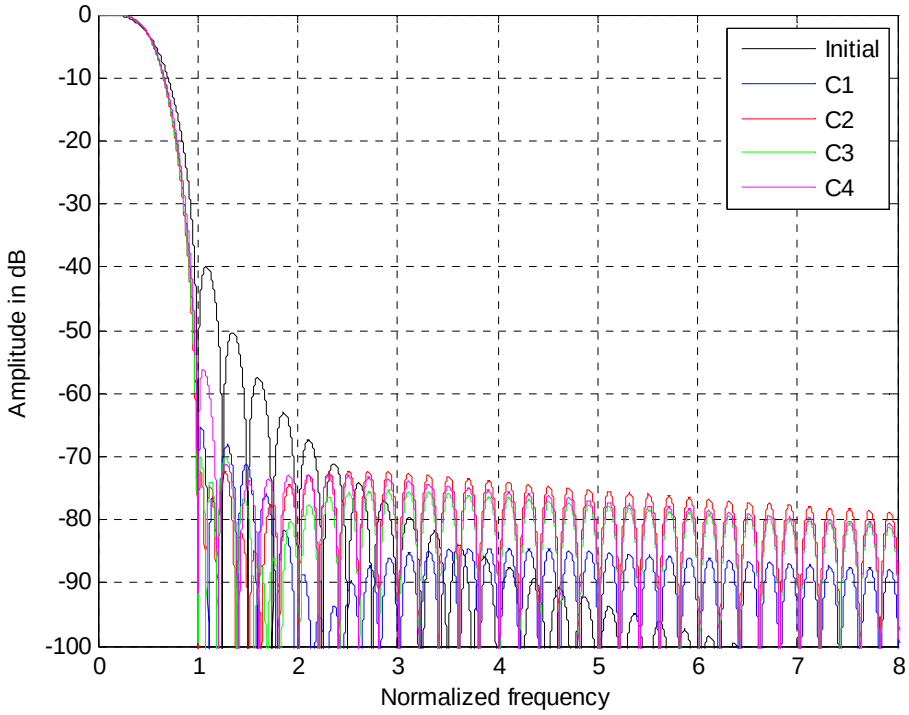

Figure 3-6: Magnitude responses of prototype filters in the case of $K = 5$, $M = 64$, and $L_p = 319$.

Table 3-1: Optimum values for the corresponding optimization criteria.

Criterion	$K = 3$	$K = 4$	$K = 5$	
	$\bar{P}[1]$	$\bar{P}[1]$	$\bar{P}[1]$	$\bar{P}[2]$
C1	0.92492844	0.97741677	0.99630534	0.88280565
C2	0.93433197	0.98040127	0.99712932	0.88818220
C3	0.92915578	0.98146562	0.99688782	0.88645686
C4	0.91697069	0.97143701	0.99561717	0.88101964

Table 3-2: The resulting total interference (TOI), minimum stopband attenuation (MSA), and level of highest stopband ripple (HSR) of the prototype filters optimized using frequency sampling technique.

Criterion	$K = 3$			$K = 4$			$K = 5$		
	TOI	MSA	HSR	TOI	MSA	HSR	TOI	MSA	HSR
C1	-41.4	-37.6	-37.6	-55.1	-45.6	-45.6	-64.4	-65.2	-65.2
C2	-35.8	-43.7	-43.7	-51.5	-51.6	-51.6	-63.6	-72.2	-72.2
C3	-38.7	-40.0	-40.0	-50.4	-50.0	-50.0	-68.0	-70.0	-70.0
C4	-45.5	-34.3	-34.3	-65.4	-39.4	-39.4	-71.6	-56.2	-56.2

3.3.2 Windowing based techniques

In this method, the prototype filter is defined according to

$$p[m] = w[m]p_{id}[m], \quad m = 0, 1, \ldots, L_p - 1.$$

At first, Hann, Hamming, Blackman, and Kaiser window based method are analyzed. By using these windows, there is only freely adjustable parameters, i.e., the cut-off frequency of the ideal prototype filter ω_c. In the case of Kaiser window, the following β-parameters are used: 5.70409414, 7.86159101, and 8.71494184 for $K = 3$, $K = 4$, and $K = 5$, respectively. Figure 3-7, Figure 3-8, and Figure 3-9 show the resulting levels of TOI and MSA. As can be seen, Kaiser window provides the lowest interference level, whereas Hamming window provides the lowest minimum stopband attenuation. Naturally, although Kaiser window has quite limited attenuation at the stopband edge, it has better characteristics when considering the overall stopband region. It should be also mentioned that Blackman window provides quite good performance when $K = 4$ and $K = 5$. Again, it has been noticed that by increasing the filter length from $L_p = KM - 1$ to $L_p = KM$ or $L_p = KM + 1$ the improvement of TOI and MSA levels are very small (only fractions of decibels).

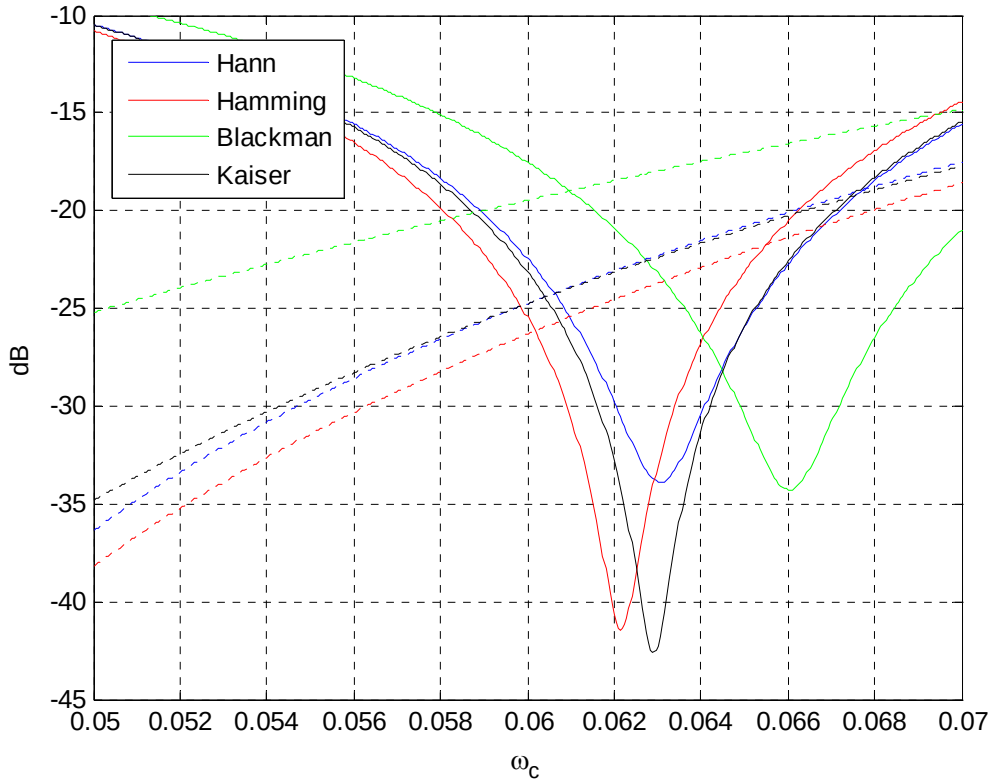

Figure 3-7: The level of TOI (solid line) and MSA (dotted line) in the case of $K = 3$, $M = 64$ and $L_p = 191$.

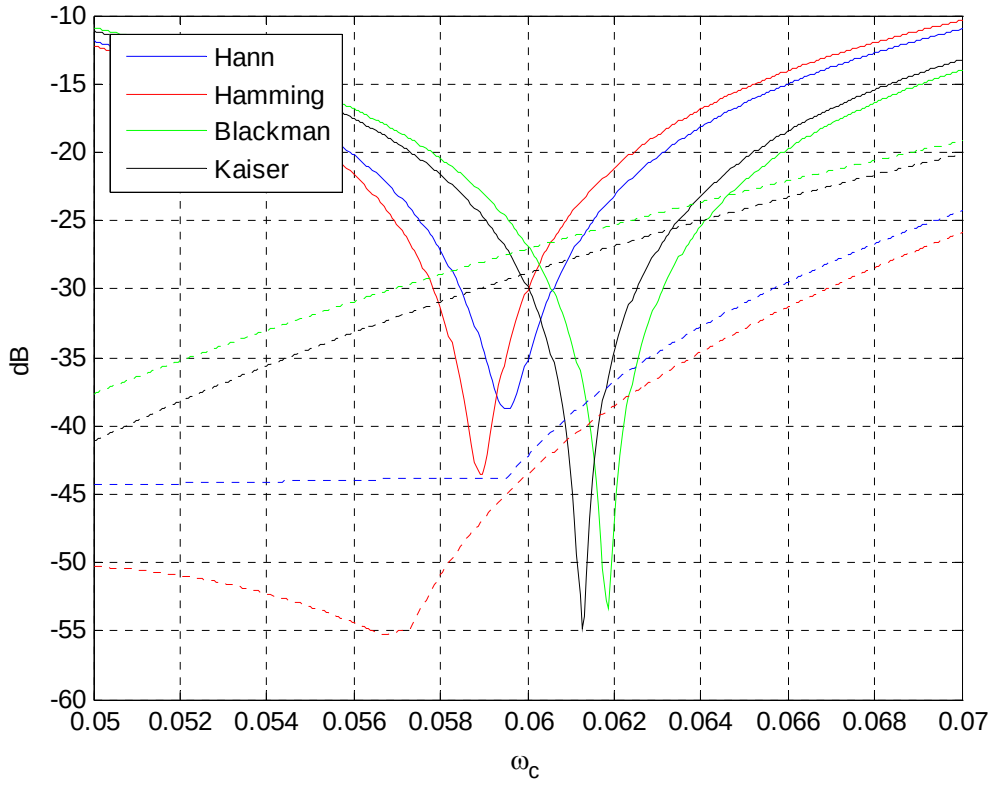

Figure 3-8: The level of TOI (solid line) and MSA (dotted line) in the case of $K = 4$, $M = 64$ and $L_p = 255$.

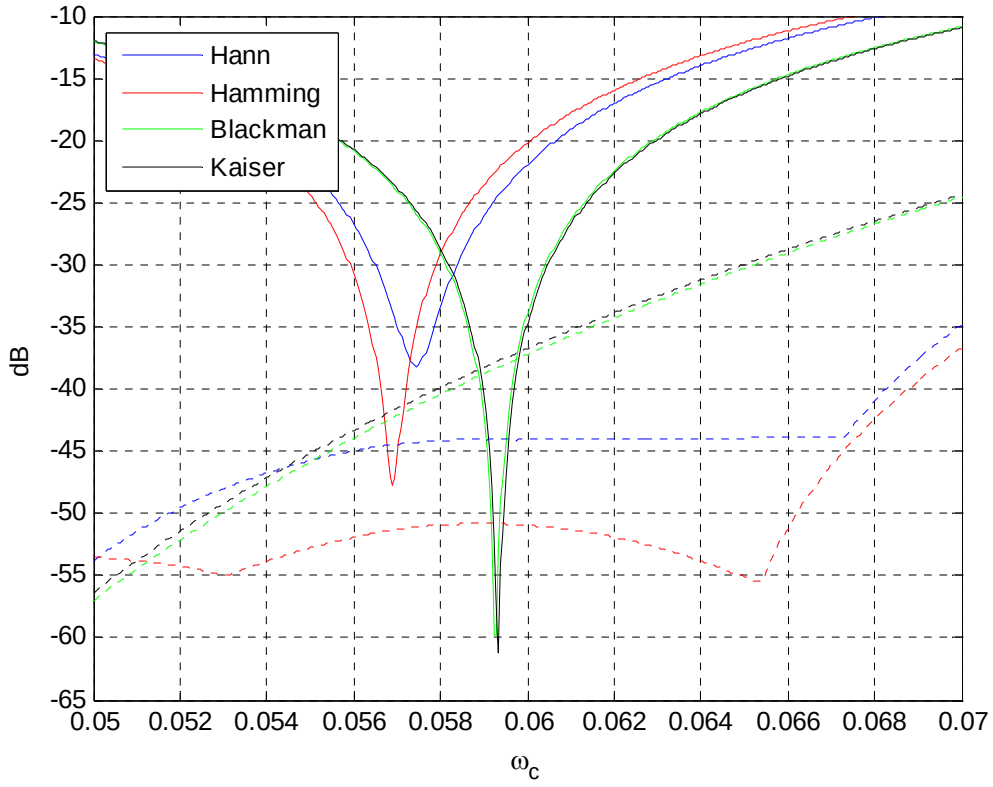

Figure 3-9: The level of TOI (solid line) and MSA (dotted line) in the case of $K = 5$, $M = 64$ and $L_p = 319$.

Next, it is analyzed how optimization affects on the stopband characteristics of the prototype filter. Due to the generalized cosine window, there are four adjustable parameters: A_0, A_1, A_2, and ω_c. Wisely chosen random values are used as initial values for the optimization. Figure 3-10, Figure 3-11, and Figure 3-12 show the magnitude responses of the prototype filters obtained using optimization criteria C1-C4 and the corresponding optimum values are given in
Table 3-3. In addition, the resulting levels of TOI, MSA, and HSR are summarized in

Table 3-4.

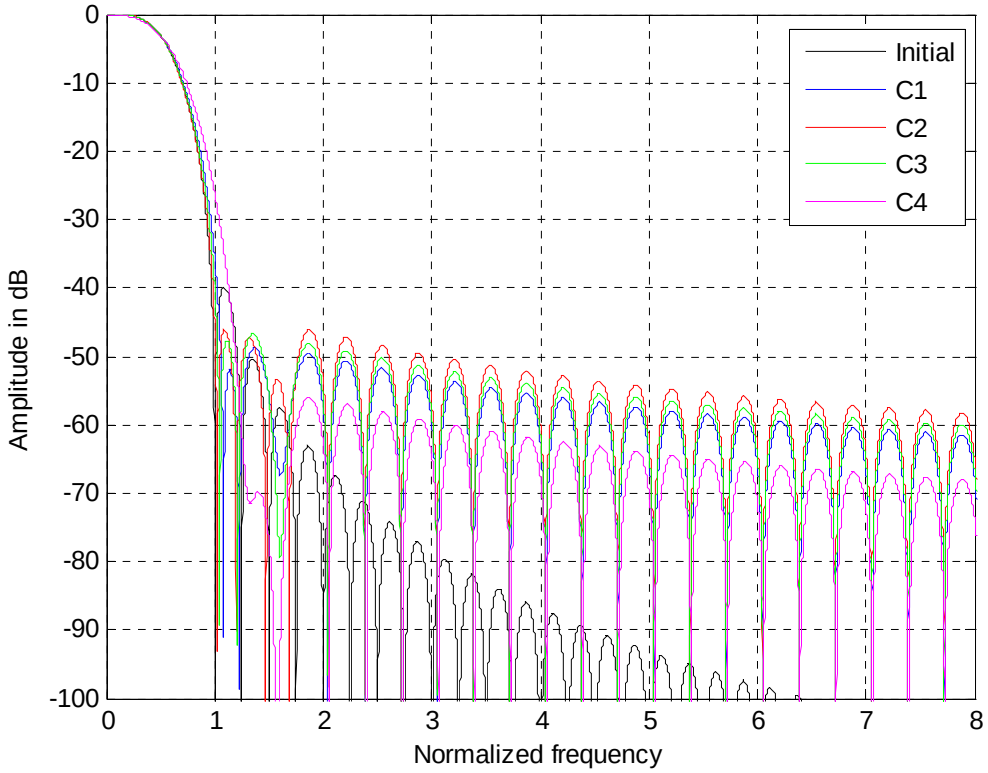

Figure 3-10: Magnitude responses of prototype filters in the case of $K = 3$, $M = 64$, and $L_p = 191$.

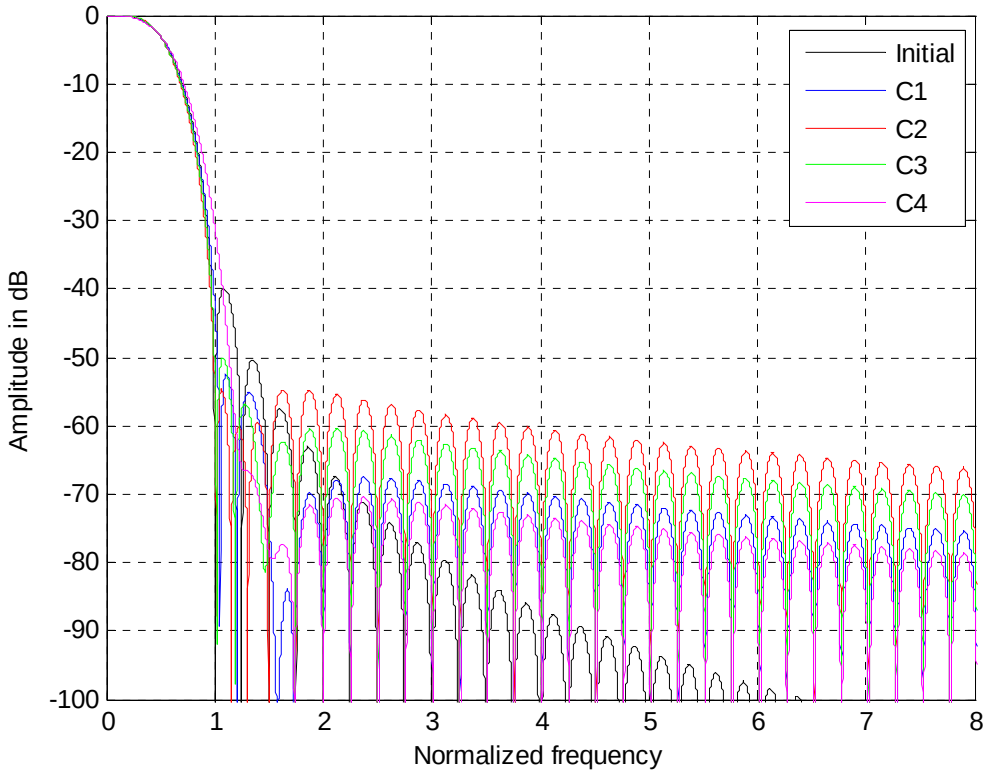

Figure 3-11: Magnitude responses of prototype filters in the case of $K = 4$, $M = 64$, and $L_p = 255$.

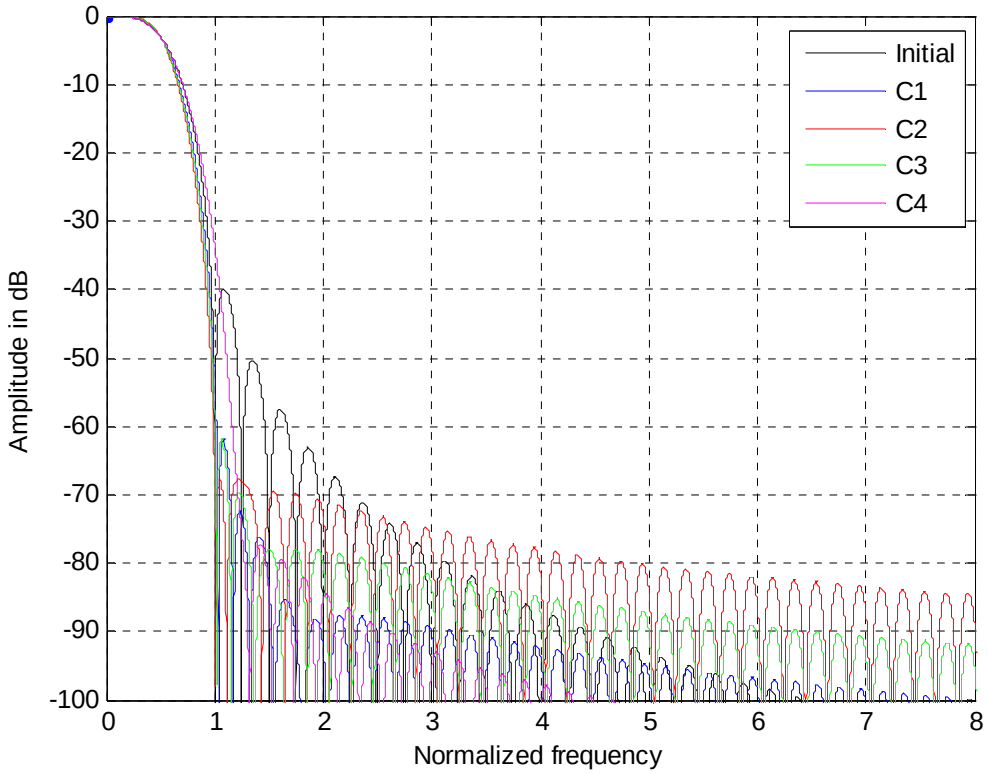

Figure 3-12: Magnitude responses of prototype filters in the case of $K = 5$, $M = 64$, and $L_p = 319$.

Table 3-3: Optimum values for the corresponding optimization criteria.

Criterion		A_0	A_1	A_2	A_3	ω_c
$K = 3$:	C1	0.63344233	0.39158850	−0.03869222	0.01366139	0.06025973
	C2	0.66616437	0.36407302	−0.04224384	0.01200644	0.05961400
	C3	0.65032109	0.37860715	−0.04420796	0.01527972	0.05994344
	C4	0.56460602	0.43691785	−0.00635910	0.00483522	0.06166610
$K = 4$:	C1	0.51378253	0.48255526	−0.00017618	0.00383838	0.05946728
	C2	0.54935496	0.45680916	−0.00921874	0.00305462	0.05882020
	C3	0.53591252	0.47037539	−0.01060960	0.00432169	0.05904375
	C4	0.46815904	0.48979876	−0.04102139	0.00102081	0.06051690
$K = 5$:	C1	0.46314600	0.49459516	0.04390429	−0.00164545	0.05831216
	C2	0.50145447	0.47584676	0.02176952	0.00092926	0.05759992
	C3	0.47987073	0.48752008	0.03337981	−0.00077062	0.05798860
	C4	0.39351190	0.50008798	0.10374506	0.00265505	0.05996216

Table 3-4: The resulting total interference (TOI), minimum stopband attenuation (MSA), and level of highest stopband ripple (HSR) of the prototype filters optimized using generalized windowing technique.

Criterion	$K = 3$			$K = 4$			$K = 5$		
	TOI	MSA	HSR	TOI	MSA	HSR	TOI	MSA	HSR
C1	−42.0	−35.5	−48.7	−43.3	−42.0	−52.4	−51.3	−52.5	−61.8
C2	−38.3	−46.0	−46.0	−42.4	−54.6	−54.6	−60.7	−67.6	−67.6
C3	−40.2	−40.0	−46.6	−41.6	−50.0	−50.0	−53.5	−60.0	−61.8
C4	−50.7	−25.7	−56.0	−62.9	−30.8	−70.3	−66.2	−33.5	−77.2

3.3.3 Direct optimization of filter coefficients

In this method, the prototype filter cannot be written using a closed-form representation. Because of the linear-phase property, a half of the impulse response coefficients are used as adjustable parameters. The initial values for the optimization can be obtained from an experimentally chosen lowpass filter. Figure 3-13, Figure 3-14, and Figure 3-15 show the magnitude responses of the prototype filters obtained using optimization criteria C1-C4. In addition, the resulting levels of TOI, MSA, and HSR are summarized in Table 3-5.

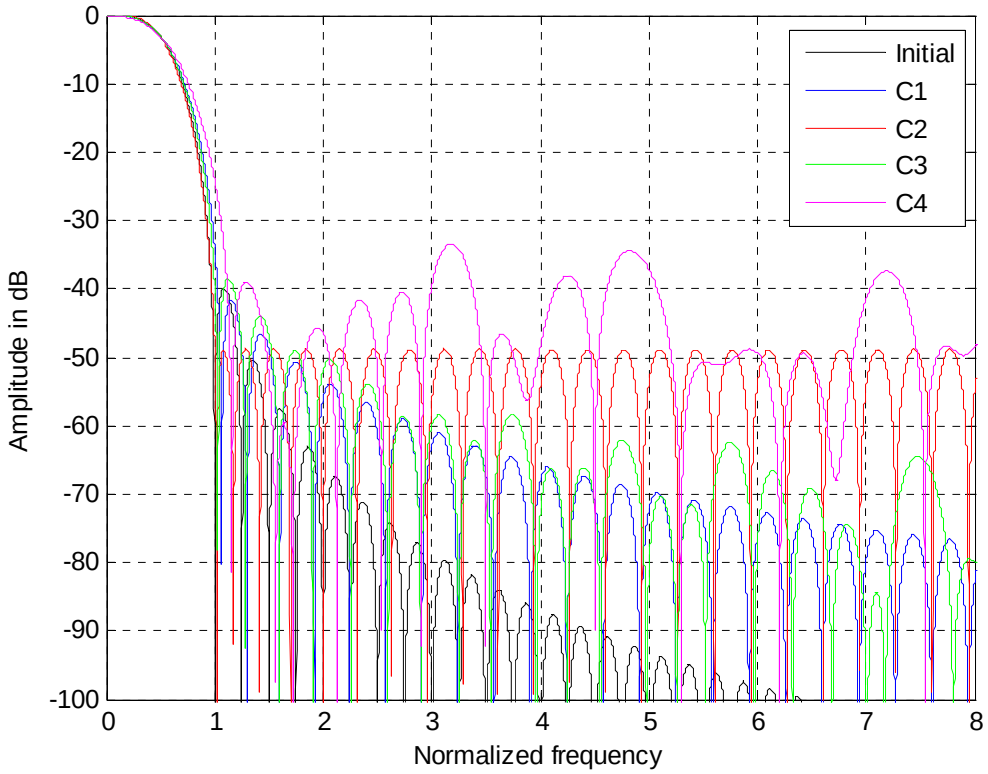

Figure 3-13: Magnitude responses of prototype filters in the case of $K = 3$, $M = 64$, and $L_p = 191$.

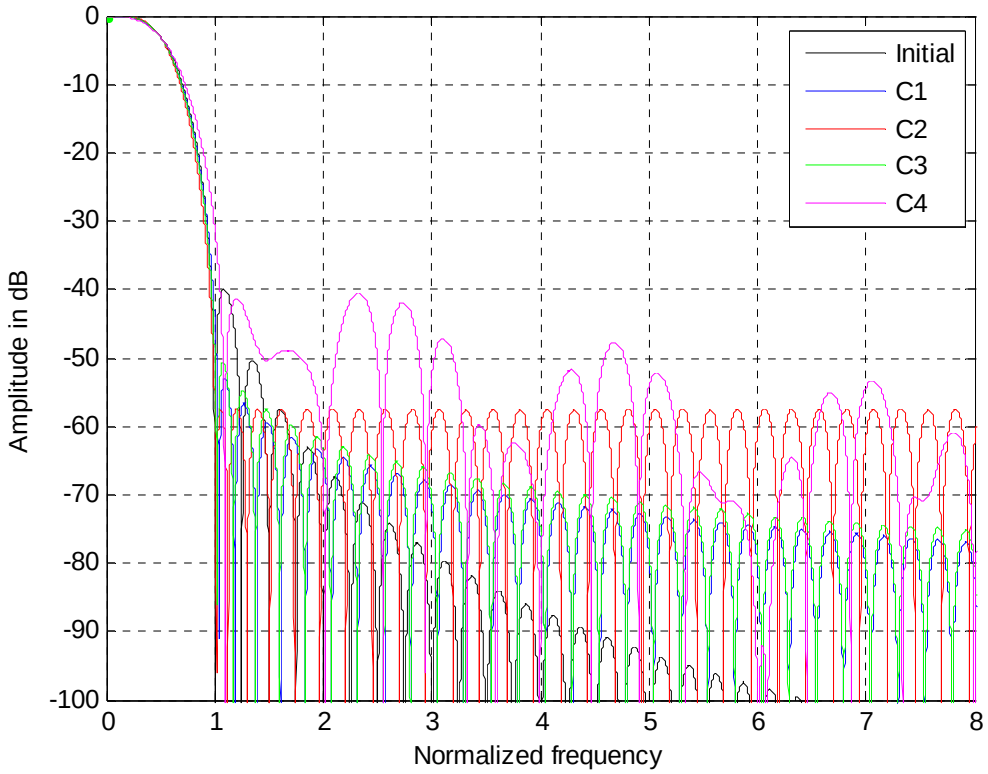

Figure 3-14: Magnitude responses of prototype filters in the case of $K = 4$, $M = 64$, and $L_p = 255$.

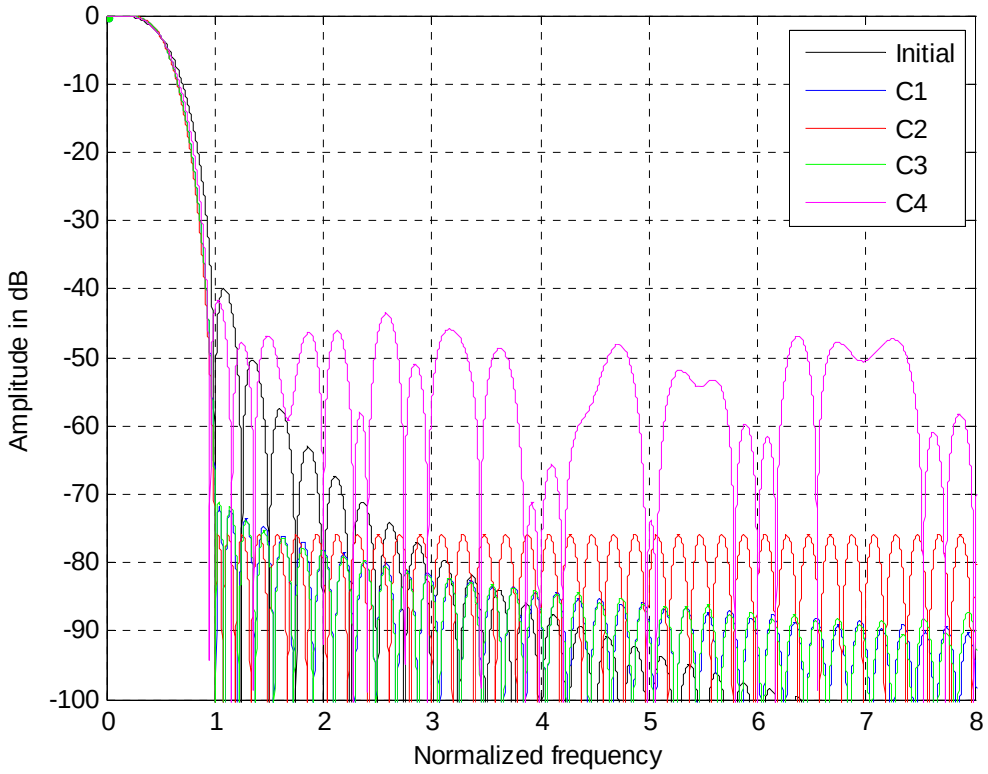

Figure 3-15: Magnitude responses of prototype filters in the case of $K = 5$, $M = 64$, and $L_p = 319$.

Table 3-5: The resulting total interference (TOI), minimum stopband attenuation (MSA), and level of highest stopband ripple (HSR) of the prototype filters optimized using direct optimization of filter coefficients.

Criterion	$K = 3$			$K = 4$			$K = 5$		
	TOI	MSA	HSR	TOI	MSA	HSR	TOI	MSA	HSR
C1	-48.5	-33.9	-41.6	-54.4	-44.3	-52.9	-66.9	-68.8	-72.3
C2	-34.8	-48.7	-48.7	-40.2	-57.3	-57.3	-50.9	-75.7	-75.8
C3	-46.5	-40.0	-40.0	-53.0	-50.0	-50.6	-66.8	-70.0	-71.6
C4	-91.1	-23.9	-33.4	-96.6	-30.8	-40.6	-101.9	-41.6	-43.5

3.3.4 Comparison between initial prototype filter and new prototype filters

The following observations can be done when comparing new prototype filters:

- LS criterion (C1): This criterion provides the second lowest TOI levels when using with frequency sampling technique (D1) and technique based on the direct optimization of filter coefficients (D3). A problem is relatively high MSA level due to low attenuation at the stopband edge. The stopband fall-off rate is quite modest for D1 and generalized windowing based technique (D2).

- Minimax criterion (C2): It is evident that this criterion provides the lowest MSA levels and also the lowest HSR levels. The local minimum attenuation should be almost constant on the overall stopband region as in the case of D3. However, for D1 and D2, the attenuation is clearly increasing steadily when going further from the stopband edge and this is most likely due to closed-form representation of the prototype filter. A drawback is a slower stopband fall-off rate and high level of TOI.

- PCLS criterion (C3): This criterion provides a trade-off between criterion C1 and criterion C2. The attenuation characteristics at the beginning of the stopband region can be improved at the cost of a slightly increased TOI level.

- Total interference criterion (C4): It is evident that this criterion provides the lowest TOI levels. It should be pointed out that the TOI level should approach the PR solution for D3 but the presented results seem to be trapped to a local optimum. A drawback is the highest MSA and HSR levels. However, the stopband fall-off rate is clearly improved when compared to other criteria.

- If the filter length is increased from $L_p = KM - 1$ to $L_p = KM$ or $L_p = KM + 1$ the improvement of TOI, MSA, and HSR levels is very small (only fractions of decibels). On the other hand, the stopband attenuation is slightly increased when going further from the stopband edge.

- It is very obvious that improved stopband characteristics and decreased TOI level can be obtained by using larger overlapping factor.

In general, frequency sampling technique seems to be best option although generalized cosine windowing based technique provides relatively good results. However, the presented optimization criteria cannot provide significant improvements because there is always a trade-off between total interference level and stopband behavior. Naturally, the case is different if the overlapping factor is increased to $K = 5$ but it is not necessarily a good option. On the other hand, the performance with $K = 3$ might not be satisfactory enough. As a conclusion, we can say that although some new prototype filters are quite good, it is very hard to find better solution than our initial prototype filter. It has several desired properties such as scalability, low level of total interference, high frequency selectivity due to superior stopband fall-off rate, and exact stopband zeros. The stopband attenuation at close distances to the transition band can be significantly increased by other design methods, but only with the cost of increased interference and reduced stopband fall-off rate. In any case, this study has provided a number of alternative designs which can be used in the other WPs of PHYDYAS when examing the effects of the filter bank characteristics on the FBMC system performance.

3.4 Performance analysis between OFDM and FBMC with different prototype filters

In this section we examine the effects of the prototype filter design on the peak-to-average power ratio (PAPR) and spectrum sensing characteristics and compare the FBMC performance against OFDM.

3.4.1 PAPR

The PAPR for the zth transmitted length-M symbol block is defined as in [25]:

$$\mathrm{PAPR}_z = \frac{\max\limits_{0\le m\le M-1} \left|s_z[m]\right|^2}{E\left\{\left|s_z[m]\right|^2\right\}},$$

where the numerator evaluates the maximum instantaneous power and the denominator estimates the average power of the signal. Above, $s_z[m]$ denotes the complex-valued baseband signal. For large values of M, the Central Limit Theorem suggests that the symbol samples $s_z[m]$ are approximately Gaussian i.i.d. random variables. In order to capture the stochastic nature of the random variable PAPR_z it is necessary to evaluate its statistical distribution. For this purpose we estimate, through numerical simulations, the Complementary Cumulative Distribution Function (CCDF) defined according to

$$Prob\left\{\mathrm{PAPR}_z > \gamma\right\},$$

where γ is a given threshold level of interest.

For bandpass transmission, the synthesized multicarrier baseband signal is modulated onto a carrier frequency f_c,

$$\begin{aligned} s_{BP}(t) &= \Re\left\{s(t)e^{j2\pi f_c t}\right\} \\ &= \Re\left\{s(t)\right\}\cos(2\pi f_c t) - j\Im\left\{s(t)\right\}\sin(2\pi f_c t) \\ &= s_I(t)\cos(2\pi f_c t) - j s_Q(t)\sin(2\pi f_c t). \end{aligned}$$

For carrier modulated signals with f_c considerably larger than the signal bandwith (this is typically the case), the maximum of the modulated signal is the same as the maximum of the baseband signal. Moreover, for QAM modulation

$$E\left\{\left|s_I(t)\right|^2\right\} = E\left\{\left|s_Q(t)\right|^2\right\} = \frac{1}{2}E\left\{\left|s(t)\right|^2\right\}.$$

Now, the average power of the bandpass signal writes

$$E\left\{\left|s_{BP}(t)\right|^2\right\} = \frac{1}{2}E\left\{\left|s_I(t)\right|^2\right\} + \frac{1}{2}E\left\{\left|s_Q(t)\right|^2\right\} = \frac{E\left\{\left|s(t)\right|^2\right\}}{2}.$$

From the equivalence of the maximum powers and the above equation it results that the PAPR of the bandpass signal is twice compared to that of the corresponding baseband signal.

Figure 3-16 shows the CCDF for OFDM and FBMC with different prototype filter designs. Two cases are included: $M = 1024$ with 160 active subchannels and $M = 128$ with 32 active subchannels. Using a relatively low number of active subchannels corresponds to significant oversampling of the baseband signal or envelope of the RF modulated waveform. Thus the results should predict well the PAPR characteristics observed in the analog domain.

The following prototype designs are included:

- PHYDYAS initial designs with $K = \{3, 4\}$
- Perfect-reconstruction designs with $K = \{3, 5\}$ obtained by using optimization technique described in [21]
- Frequency-sampling based design optimized for maximum stopband attenuation with $K = 4$.

The following conclusions are obvious:

- The prototype filter has only a minor effect on PAPR. This applies to the considered types of prototypes, and is expected to apply more generally to symmetric prototype filter impulse responses with roll-off close to 1. Non-symmetric designs tend to be bad for the PAPR.
- The PAPR characteristics of OFDM and FBMC are very similar.

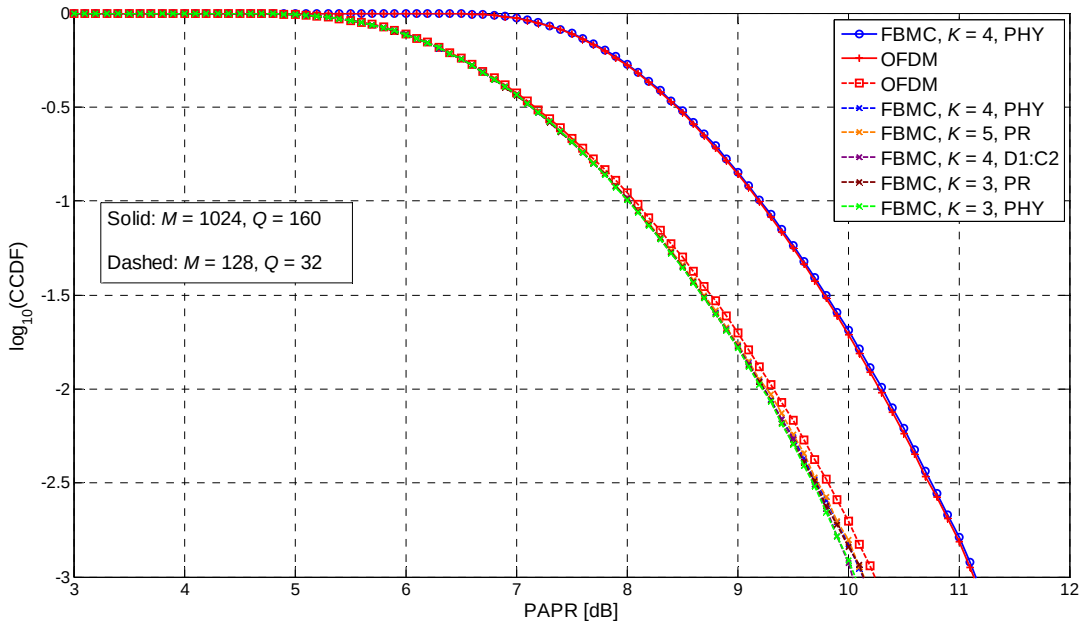

Figure 3-16: CCDF of PAPR for OFDM and FBMC.

3.4.2 Spectrum sensing

In the concept of cognitive radio, secondary user (SU) devices are allowed to transmit and receive data over portions of spectra where/when primary users (PUs) are inactive provided that secondary transmissions do not cause any harmful interference to PUs. In order to facilitate this, SUs have to regularly perform reliable radio scene analysis to detect potential PU signals with high detection and low false alarm probability. A failure to fulfill these requirements would result in bandwidth efficiency loss in primary or secondary transmission, respectively.

In the literature, a number of spectrum sensing techniques have been discussed, which can coarsely be classified as cooperative or non-cooperative detection methods based on whether or not information from multiple CRs are incorporated for primary user detection. The different spectrum awareness schemes can further be categorized into matched filter detection, energy detection, and

cyclostationary feature detection techniques, each with their individual pros and cons [26]. Approaches differ from each other in terms of implementation complexity, amount of prior knowledge required, processing gain obtained, and detection time required.

In PHYDYAS project, it is the objective of the Work Package 8 to develop advanced, robust and efficient spectrum sensing methods. Here, we simply demonstrate the role of the prototype filter selectivity on the performance of the classical energy detection in case of OFDM and FBMC receivers. Energy detection measures the energy of the received signal. In multicarrier receiver exploiting energy detection the samples of the subchannel signals at output of AFB are squared and averaged over the observation interval to obtain an estimate of the received energy for each subband. The obtained values can be then compared to a pre-defined threshold to make subband-wise decisions on whether the PU signal is present on corresponding portion of the signal band or not. In the following example, the simulation set-up is as follows:

Radio scene:	
Number of primary user signals:	3 ([PU1, PU2, PU3])
Type of signals:	RC pulse shaped single-carrier signals
Relative symbol rates:	[R, R, 2xR]
Sampling rate F_s:	16xR
RC roll-off:	[0.15, 0.1, 0.15]
Center frequencies (w.r.t. $F_s/2$):	[-0.25, 0, 0.3]
True band edges:	[-0.32 & -0.18; -0.07 & 0.07; 0.16 & 0.44]
Relative power levels in dB:	[0, -43, -10]
Type of modulation:	[QPSK, BPSK, 16-QAM]
SU receiver:	
Transform size M:	1024
Prototype filter:	rectangular (OFDM), PHYDYAS reference filter design (FBMC)

As can be seen in Figure 3-17, FBMC receiver provides an accurate and reliable analysis of the observed spectrum as also reported in [27]. Contrarily to OFDM receiver, FBMC receiver is not blinded by the presence of high level neighboring signals and is able to identify accurately the edges of the spectrum holes (SH) (frequency bands [-0.18 -0.07] and [0.07 0.16]). It has also been observed that the performance is very similar with other frequency selective prototype filters. On the other hand, OFDM receiver with rectangular prototype filter suffers from power leakage and would likely fail to detect the presence of the weak PU2 signal in the investigated radio scene. The FBMC receiver can be observed to be a superior spectrum analyzer compared to the conventional OFDM receiver when sensing of radio scenes with potentially large power dynamics is considered.

The main advantage of the energy detector is its implementation simplicity. There is virtually no extra implementation cost, in terms of receive filtering, as the same AFB can be used for both data reception and spectrum sensing. Moreover, the processing for obtaining the energy estimates is straightforward and simple. However, an evident disadvantage is that the performance of energy detector is clearly sensitive to background noise. Whenever the level of noise is sufficiently high with respect to the received power of the PU signal, the energy detector fails to discriminate between the signal source and the noise component. This results unavoidably in high detection error rate in case of low SNR. Such low SNR scenarios are appropriate topics for WP8, where more advanced and robust (e.g., against noise) sensing algorithms are developed based on the frequency selectivity of the FBMC.

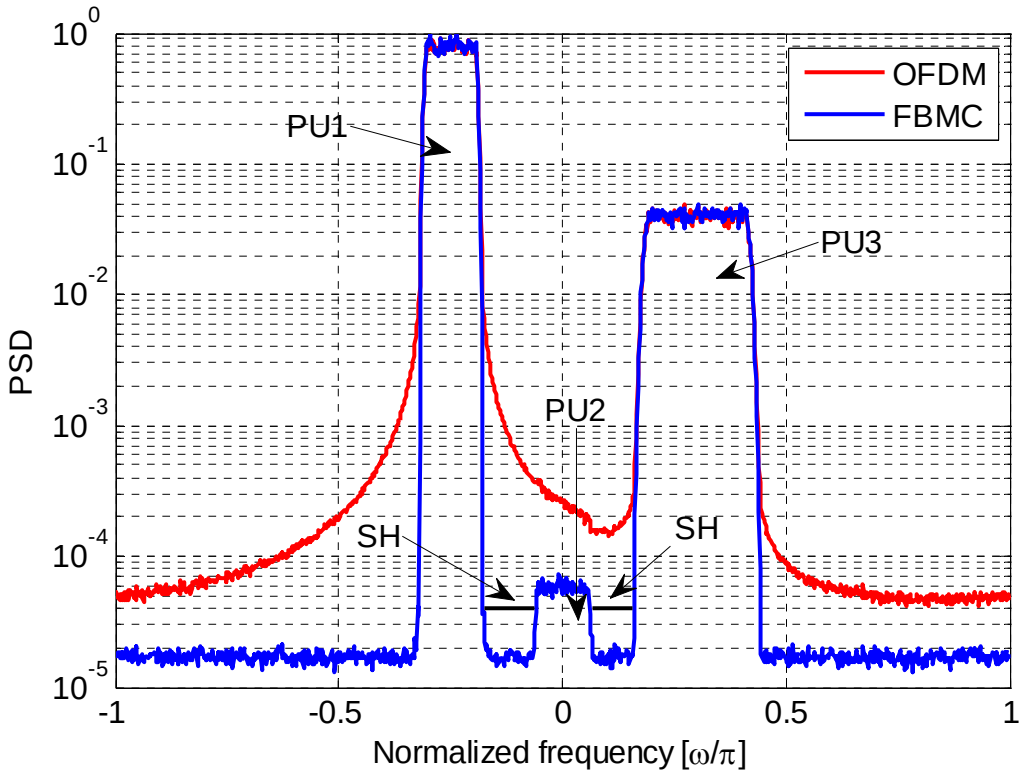

Figure 3-17: Power spectral density (PSD) of an energy detector in the case of OFDM and FBMC.

3.5 On spectrally efficient multiplexing in cognitive radio systems

In this section, it is studied how well different multicarrier schemes are able to exploit the identified time-frequency resource slots (spectrum holes). In particular, we analyze the trade-off between the level of interference caused by secondary transmission to primary user and the spectral efficiency of secondary user as in [28].

3.5.1 Interference analysis

In the interference analysis, the following multicarrier schemes are considered based on the used prototype filters:

1. *OFDM without a cyclic prefix (CP)*

The prototype filter is a rectangular window

$$p_1[m] = 1, \quad m = 0, 1, \ldots, M-1.$$

2. OFDM with a CP

The prototype filter is a temporally extended version of $p_1[m]$, i.e.,

$$p_2[m] = 1, \quad m = 0, 1, \ldots, T-1,$$

where $T = L_{CP} + M$ with L_{CP} being the length of the CP in samples.

3. Raised cosine (RC) windowed OFDM

The adjacent channel leakage can be reduced by multiplying the OFDM symbols with a RC window before transmission. For simplicity, this extra windowing is modeled here with the prototype filter defined in [29]

$$p_3[m] = \begin{cases} \frac{1}{2} + \frac{1}{2}\cos\left(\pi + \frac{\pi m}{\beta T}\right), & 0 \leq m < \beta T \\ 1, & \beta T \leq m < T \\ \frac{1}{2} + \frac{1}{2}\cos\left(\frac{\pi(m-T)}{\beta T}\right), & T \leq m < (1+\beta)T. \end{cases}$$

The considered roll-off values are $\beta = \{0.1, 0.25, 0.75\}$ that correspond to the prototype filters $p_{3a}[m]$, $p_{3b}[m]$, and $p_{3c}[m]$, respectively.

4. NPR FBMC

Here we consider the PHYDYAS reference filter bank designs with *K*={3, 4}.

The overall stopband behavior of different prototype filters can be seen from Figure 3-18, whereas Figure 3-19 shows the details of the mainlobe, transition band, and some of the first sidelobes.

The interference caused by a secondary user transmission to a primary system is analyzed using the frequency domain model shown in Figure 3-20. The principal idea is to use the frequency response(s) of the prototype filter $P_i(e^{j\omega})$ and a frequency domain mask $F_{mask}(e^{j\omega})$ (with unity gain in the passband) to model the secondary user signal and the primary receiver, respectively. The normalized cumulative interference power leaking into the primary user band is obtained by numerically integrating over the mask-weighted power density spectrum (PDS) of the sidelobes within the receiver mask:

$$I_c(i, d, B) = \sum_{l=1}^{B} \int_{\omega_L}^{\omega_H} \left| P_i\left(e^{j(\omega + l\frac{2\pi}{M} + d)}\right) F_{mask}\left(e^{j\omega}\right) \right|^2 d\omega, \tag{47}$$

where $i = 1, 2, \ldots, 4$ and the summation is done over all the active subcarriers in the interfering secondary signal multiplex. The overall power of the prototype filters is normalized to unity, i.e., $\int_{-\pi}^{\pi} |P_i(e^{j\omega})|^2 = 1$ for all i.

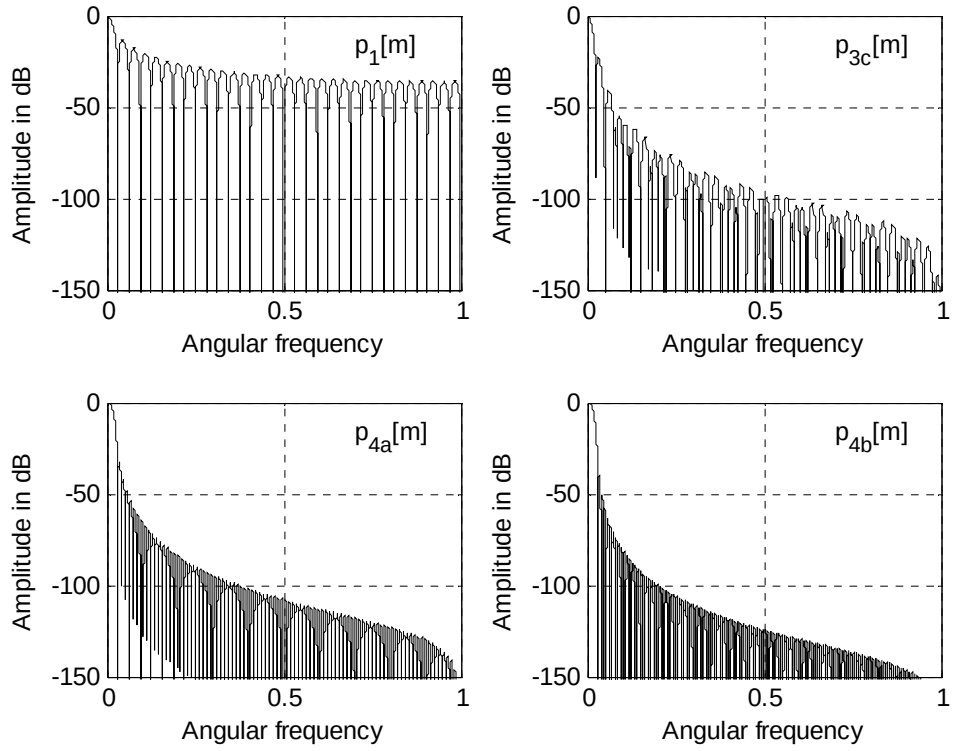

Figure 3-18: Magnitude responses of the prototype filters in the case of $M = 64$. Rectangular window without a CP ($p_1[m]$), RC window with $\beta = 0.75$ ($p_{3c}[m]$), NPR designs with $K = 3$ ($p_{4a}[m]$), and $K = 4$ ($p_{4b}[m]$).

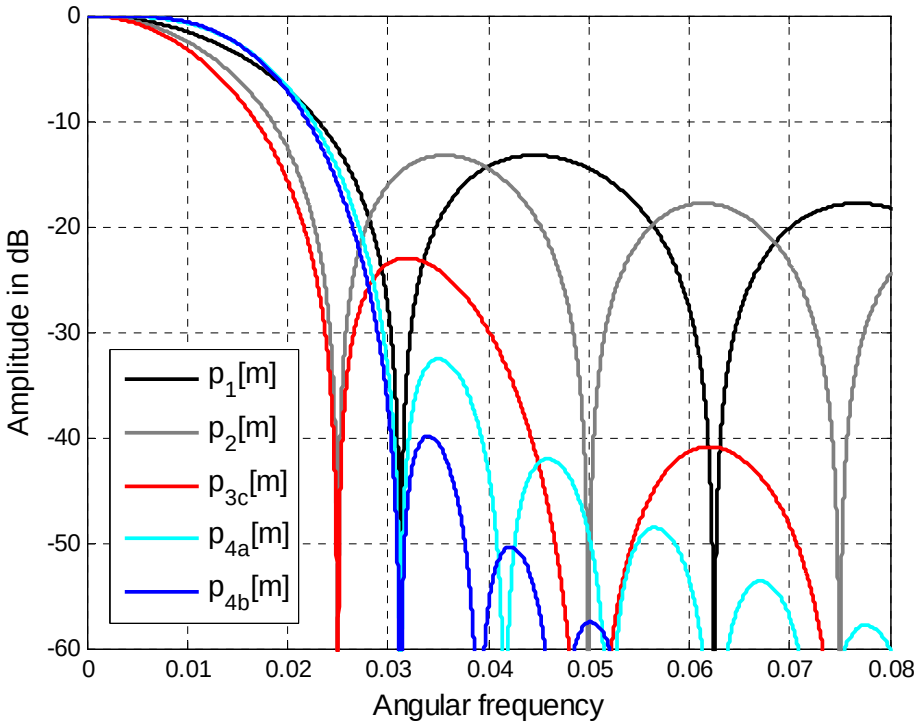

Figure 3-19: Spectral details of the prototype filters.

The model is generic in a sense that one has control on the following:

- Selection of the prototype filter $p_i[m]$ to model different secondary multicarrier schemes.
- The distance d between the center frequency of the last active (band edge) subcarrier in the secondary signal multiplex and the edge of the receiver mask to model the influence of the guard band.
- The number of active subcarriers B to model the cumulative interference contribution.

In the forthcoming analysis, we consider only the ideally bandlimited mask shown in Figure 3-20.

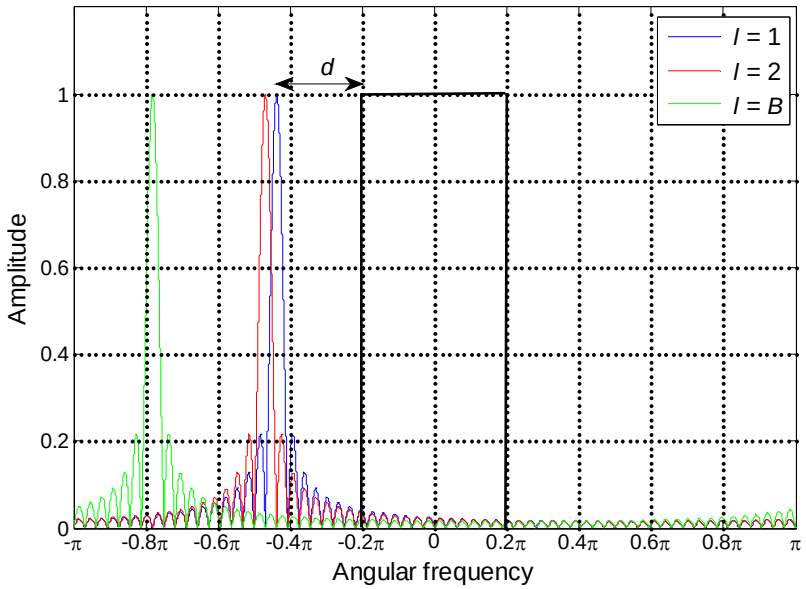

Figure 3-20: The idealized frequency-domain model for the interference analysis.

3.5.2 Numerical results

The sampling rate of $f_s = 30$ MHz and a filter bank consisting of $M = 1024$ subcarriers was used in the simulations. This corresponds to a subcarrier spacing of $\Delta f = 29.3$ kHz. The number of active subcarriers was chosen as $B = 20$. The results are given in terms of the normalized interference power I_c as a function of the normalized width of the guard band $d/\Delta f$. It should be noted that in the analysis, the potentially interfering secondary signal was located only on one side of the primary band. In practice, the primary band may be surrounded by secondary signals on both sides. A CP of length corresponding to 12.5 % of the useful symbol period was used in case of OFDM. The roll-off values of $\beta = \{0.1, 0.25, 0.75\}$ were tested for RC windowed OFDM. For the NPR FBMC design, overlapping factors $K = 3$ and $K = 4$ were used. The obtained simulation results are shown in Figure 3-21.

OFDM with rectangular prototype filter with and without a CP ($p_1[m]$) show very slow decay of the interference power. The RC windowing with increasing β clearly pushes down the level of interference introduced by the OFDM. This is due to improved spectral concentration of the subcarrier filter response ($p_3[m]$). With the NPR prototype ($p_4[m]$), a very fast and consistent decay of interference power can be obtained by allowing a limited amount of ISI and ICI.

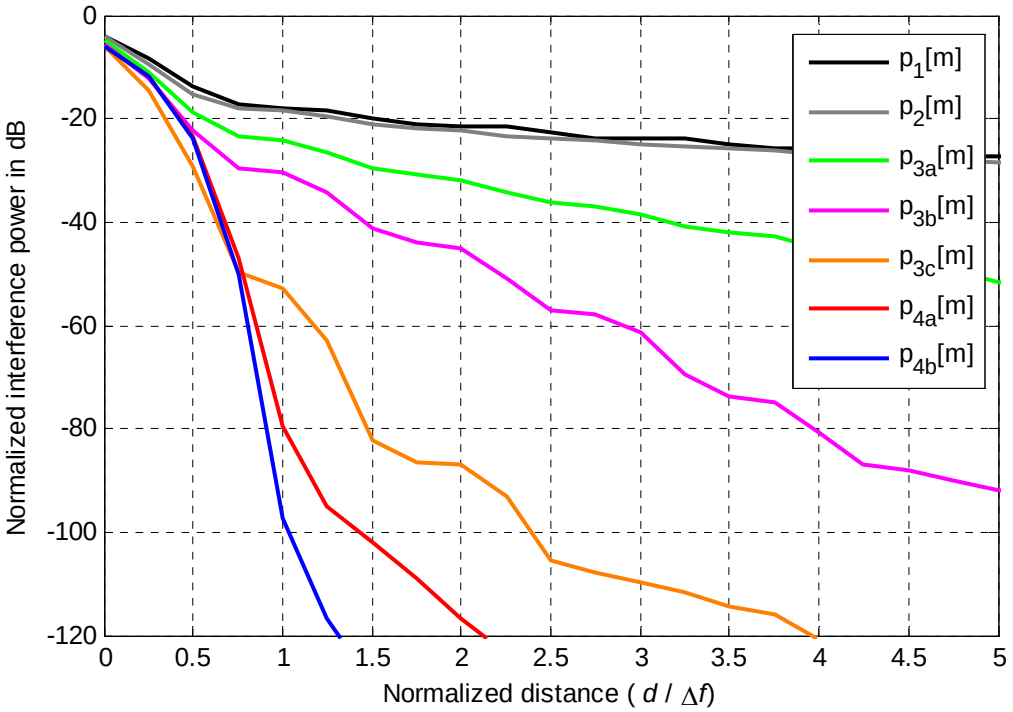

Figure 3-21: Normalized interference power for ideally bandlimited mask.

How to interpret the obtained results? Given an interference power threshold of interest, say -70 dB, one can observe that the different multicarrier schemes reach the threshold with different widths of guard band. The reduction in the required guard bandwidth with NPR prototype, in comparison to windowed OFDM with $\beta = 0.25$, is 2.5 on the normalized scale for the ideally bandlimited mask. The relative gain reduces with increasing value of β. The required guard bandwidth is directly connected to the spectral efficiency of the secondary transmission. Furthermore, in the case of RC windowed OFDM, the narrower guard band in the frequency domain (obtained with higher value of β) is traded with extension of the symbol duration by $(1 + \beta)$ in the time domain. The considered values of $\beta = \{0.1, 0.25, 0.75\}$ correspond to time domain overheads of $\frac{\beta}{1+\beta} = \{9, 20, 43\}\%$, respectively.

Another way to interpret the results is to consider a fixed width of the guard band, say three on the normalized scale, and to inspect the differences in the interference power levels obtained with different multicarrier schemes. The lower the interference power obtained with certain prototype the higher the corresponding secondary signal power can be to fulfill the given constraints of interference. In this way, the frequency selectivity of the prototype is related to relative power of the secondary signal and the primary user receiver.

The above analysis shows that the selection of the prototype filter, used as the basis of the multicarrier modulation in the overlay secondary transmission, plays an important role. With improved spectral concentration of the prototype filter, the level of interference power caused by the secondary transmission to the primary system can be controlled and the required frequency domain guard band can be minimized. The RC windowing enables this in the case of OFDM. However, this becomes at the price of increased symbol period (with increasing β) and thus results

in the loss of spectral efficiency in the time domain. Using filter bank approach, a low-interference secondary transmission can be obtained without sacrificing the bandwidth efficiency. Therefore, the additional complexity of the FB approach, due to introduced pulse shaping, can be seen to be well profitable in the CR context.

The analysis here assumed idealized frequency selectivity for the primary user. Naturally, the study should be extended by considering the channel selectivity characteristics of practical primary user receivers.

4 Analog and digital front-end

In this chapter we focus on the RF stages and analog and digital baseband processing following the synthesis bank on the transmitter side and preceding the AFB on the receiver side. First, Section 4.1 addresses the baseband digital channel selection filter stage, especially in the cognitive radio context. The usefulness of the filter banks for implementing the channelization filtering in a flexible manner is emphasized. Section 4.2 gives a general overview of receiver RF architectures and Section 4.3 examines the effects of central RF impairments on FBMC transmission.

4.1 Flexible channel selection

Traditional wireless communication systems are characterized by dedicated frequency bands and well-defined frequency channels. After analog and digital receiver front-ends, the signal contains only the transmissions allocated to that channel, which have well-controlled dynamics under the radio resource management (RRM) functionalities of the wireless network. No strong interfering spectral components due to other kinds of waveforms are expected to be present. In OFDM systems, different user signals are quasi-synchronous due to the use of cyclic prefixes, and can be separated using FFT-based processing. Naturally, there are distorting effects which, e.g., introduce ICI, but these effects are kept under control by proper system and algorithm designs.

In this context of flexible spectrum usage, the used frequency band is not anymore dedicated to a specific service and specific waveforms. The band cannot be expected anymore to be free of other waveforms, the utilized frequency spectrum may be discontinuous, and the dynamics of signal power levels are not well-controlled anymore. This calls for efficient means to separate the portions of the frequency spectrum, which are utilized in a specific transmission, from other portions which are considered as interference. Filter banks are ideal for this purpose.

In OFDM systems, the FFT provides fairly good selectivity to signal elements which are synchronized to the CP structure, but not to any other spectral components. Therefore, the frequency selectivity has to be implemented in the analog and digital front-end, as in traditional receiver architectures. Filter banks don't have this limitation, and they can be used for implementing major part of the channel selectivity, thus relaxing the digital front-end complexity. Furthermore, in dynamic spectrum use scenarios, filter banks are superior in terms of flexibility, in comparison to any other digital filtering structure: The channel selectivity is implemented simply by selecting the desired subchannels from the analysis filter bank output.

To be able to utilize the analysis filter bank for implementing the receiver selectivity, most of the synchronization and signal detection related functionalities should be implemented in frequency domain, by processing the subchannel signals only. This is one important theme in all the other signal processing Work Packages of PHYDYAS. One alternative is to convert the signal back to time-domain using a synthesis filter bank after selecting the needed subchannels. This would lead to very high computational complexity and increased latency, but there might be some interest to consider this approach for specific functions, e.g., during the initial synchronization phase.

When using a filter bank for implementing the channel selectivity, the resulting transition bandwidth is primarily determined by the transition bandwidth of the prototype filter. In the following we examine the efficiency of using the analysis filter bank for implementing the receiver selectivity through simplified numerical examples.

Numerical example of using AFB for implementing the receiver selectivity

We consider the WiMAX-like case with the FFT-size of $M = 1024$ and sampling rate of $f_s = 11.2$ MHz in OFDM-OQAM modulation. The PHYDYAS reference filter bank with $K = 4$ is used. Assuming the extreme case that just one subcarrier is used as a guardband between different users, then 913 subcarriers can be fitted to the 10 MHz bandwidth.

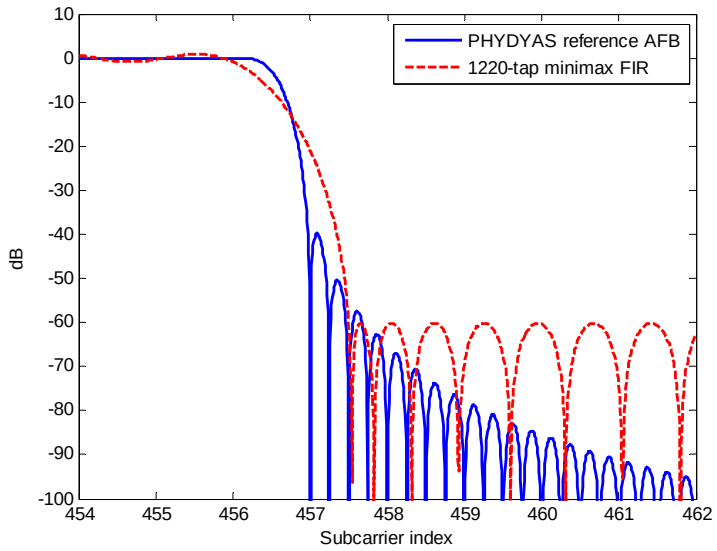

Figure 4-1: Comparison of the selectivity of PHYDYAS reference filter bank design and a linear-phase FIR filter of length 1220.

First we design a linear-phase FIR filter, using to the minimax criterion and 0.1 dB maximum passband ripple, such that it approximately matches the transition band of the filter bank design. As can be seen from Figure 4-1, the match is good regarding the attenuation of the second subchannel (with subcarrier index 458) from the band edge, but the AFB design has the useful characteristic of increasing stopband attenuation with increasing distance from the passband. The frequency response of the FIR filter is inferior to the FB design in every respect, but it serves the purpose of giving a rough estimate of a direct-form FIR filter length having similar selectivity as what can be achieved with the filter bank. The required FIR filter length is 1220. As a linear phase filter, it can be implemented for a complex input signal with about 1220 multiplications per input sample. On the other hand, utilizing the expression of Section 2.4 Eq. (17) for the complexity of the analysis filter bank, we see that about 34 real multiplications per input sample are needed. Reduced-complexity FIR filter designs would be possible (e.g., using the complementary response of narrowband lowpass filter designed using the frequency response masking approach [32]). In any case, it is not easy to reach the multiplication rate of the filter bank in an FIR filter design. Furthermore, it would be extremely difficult to reach the flexibility of the filter bank with any other filter design approach and similar complexity.

Similar selectivity could be implemented using an elliptic IIR filter of order 12. At least 24 real multiplications per complex input sample would be needed in the implementation. However, such an IIR filter would have highly nonlinear phase response and it would be very sensitive to the finite wordlength effects.

Advanced communication receiver designs are often based on oversampling in the analog-to-digital converter (ADC), leading to reduced analog filter complexity and further flexibility in selecting the desired part of the spectrum from a wider frequency band. As another example, we can consider a case where the signal (possibly after some preprocessing with low-complexity decimation filters) is sampled at two times the sampling rate specified for multicarrier processing, i.e., at $2f_s = 22.4$ MHz. Now we consider two alternative structures:

1. Using an AFB with $2M = 2048$ subchannels and input at rate $2f_s$. Now 68 real multiplications are needed at the rate of f_s. As will be discussed in Section 5.1, there are no problems in combining SFB and AFB of different sizes, e.g., when utilizing PHYDYAS reference filter bank designs.
2. Using a halfband FIR decimating filter and the basic AFB with $M = 1024$. The required length of the halfband filter for 60 dB stopband attenuation is 63. It has 33 nonzero taps, one out of which is trivial. Due to coefficient symmetry, it can be implemented with 32 real multiplications per output sample (at rate f_s) for a complex input signal. Thus, the overall rate of real multiplications is 66 per sample at rate f_s.

We can see that these two approaches have practically the same computational complexity in terms of real multiplications. However, the filter bank approach enjoys of much higher flexibility:

- In the second approach, the desired signal is assumed to be located within a 10 MHz bandwidth centered around 0. The bandwidth is limited to $f_s = 11.2$ MHz, and the decimation filter complexity grows rapidly when this value is approached.
- In the filter bank approach, there are no such strict limitations for the useful frequency band and the center frequency. The useful frequency band is basically limited by the analog filter, ADC and preceding decimation filter stages.

4.2 RF architectures

4.2.1 Key constraints

There exists a plurality of potential RF architectures in order to integrate a transceiver. The final choice is imposed by some key constraints which are most of the time linked to some economical or technological motivations. They have to be pointed out before comparing the different RF candidate architectures.

4.2.1.1 Fully integrated transceiver

Although improvements of RF silicon technologies have received considerable attention during the past ten years, there are still some building blocks which cannot be integrated on the same die with

the core circuit. They are mainly the antennas, the duplexer, the application SAW filter and the power-amplifier. There are some exceptions for each of these blocks: antennas are integrated in 60 GHz products, duplexer and BAW filters have been reported on chip in WCDMA applications and for low-power applications, such as Bluetooth and ZigBee, the power amplifier is fully integrated. However, most of the time, these building blocks are not available on chip. As a consequence, the duplication of such components increases the size, the cost of the terminal (component and the assembling costs) as well as the overall power consumption (power is consumed to get out of chip because of the 50 Ohms required impedance).

4.2.1.2 CMOS technology

The CMOS technology is the preferred solution because the associated development cost is much lower than in the bipolar technology. However, the MOS transistor has got a number of drawbacks listed below. The RF architecture should be selected keeping in mind those disadvantages.
A major drawback of the MOS transistor is its low-frequency behaviour. In a differential pair, the input offset voltage is high (about 1mV for a 100 μ^2 NMOS transistor) compared to a Bipolar transistor. In 0.35um CMOS technology, an NMOS transistor with 0.5 μm length and bias current of 50 μA exhibits a 1/f noise corner frequency in the vicinity of 10 MHz. Transconductance matching between two MOS transistors is also much lower (0.2% for a 100 μ^2 NMOS transistor) than for bipolar one. However, all this performance issues may be improved by increasing the transistor length, with the cost of much higher parasitic capacitances. The input impedance of a MOS transistor is much higher than the input impedance of a bipolar transistor at low frequencies. However, as frequency is increased, its input impedance decreases since it is mostly capacitive. The equivalent frequency between MOS and bipolar, depending on transistor area, is in the range of one hundred MHz. Lastly, to obtain the same transconductance value with a MOS transistor in saturation mode, a higher current is needed compared to bipolar transistor.

4.2.1.3 Multi-Standard capability

With the increase of the number of wireless applications in the recent years, in order to reach a seamless communication network, the future terminals will have to integrate several wireless standards on the same die. This puts stringent requirements on the RF transceiver, since it is not possible to multiply the number of RF front-ends, otherwise, the power consumption and cost of the terminal would increase drastically. As a consequence, the RF architecture should bring some reconfiguration capability in order to allow covering several standards with the same front-end, which is a difficult task since radio frequency design and tunability are hardly compatible. Therefore, the reconfiguration should be eased with a judicious choice of the RF architecture. The following paragraph is going to present the different architectural solutions for the integration of a transceiver and the associated drawbacks and advantages according to the above mentioned criteria.

4.2.2 Architecture overview

This chapter deals with the comparison of possible architectures for the integration of the RF front-end in the context of a WiMAX standard. This part presents advantages and drawbacks of four architectures, taking into account the previously defined criteria. For the sake of simplicity, to illustrate the basic principles of the different architectures, amplification stages and A/D conversion are not shown in the different schemes. This architecture study mainly concentrates on the receiver

part since it is the most critical in a wireless system. The receiver has to demodulate a very low desired received power in the presence of strong out of band blockers with a wideband spectrum, whereas the transmitter is only treating the desired signal which needs to be emitted. The bottleneck of the transmitter is evidently the power amplifier whose linearity has to be considered. This issue is going to be analyzed and modelled in the following chapter.

4.2.2.1 Heterodyne architecture

Basic principle

The heterodyne architecture was the most frequently used for RF front-end in wireless communications. In a simple heterodyne architecture (cf. Figure 4-2) the RF signal is applied to a low-noise amplifier (LNA) and subsequently an image-reject filter. The result is then down-converted to the intermediate frequency (IF) using a mixer with the output of a local oscillator (LO). The desired channel is then selected by an IF filter that suppresses out-of-channel interferers. This well known structure provides high sensitivity and high selectivity.

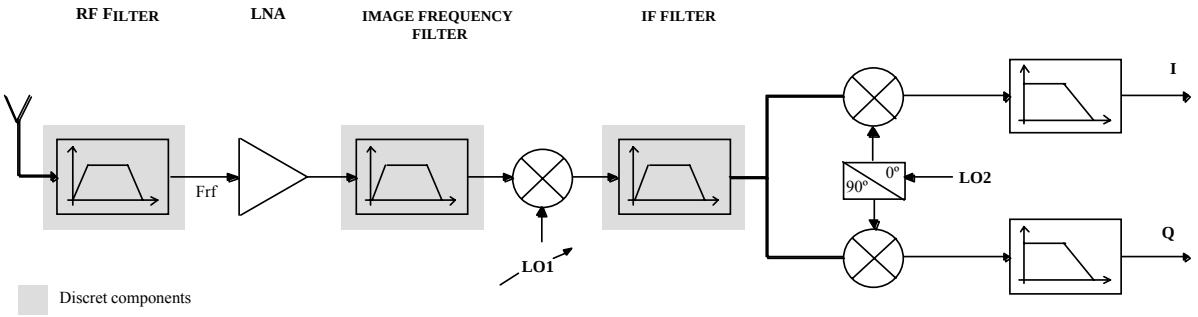

Figure 4-2: Simple IF heterodyne architecture.

The main problem in heterodyne architecture is the trade-off between image rejection and adjacent channel suppression. For given filter quality factors, if the IF is high the image is greatly attenuated whereas nearby interferers remain at a significant level. Conversely, if the IF is low, the image corrupts the down-converted signal but interferers are suppressed. For this reason, both the image-reject filter and the IF filter require good selectivity, thus they are impossible to integrate. So these filters are usually external filters such as surface acoustic wave (SAW) devices. Furthermore, the off-chip filter increases the constraint on the LNA and mixer that must drive a 50 Ω load. Therefore, the trade-offs between noise, linearity, gain and power dissipation of the amplifier become more difficult. A system designed with a heterodyne structure requires many external components so it can't be fully integrated.

Possible improvement

The image frequency filter may be replaced by an emerging solution which is the use of image reject mixer. This mixer consists of two de-phased signal paths. In the two branches the spectra contain the desired signal with the same polarity and the image signal with opposite polarity. The sum of the two branches is then free from the image signal. The problem of this architecture is that the gain and phase mismatches between the two signal paths results in an imperfect image rejection. To get rid of the IF filter, different solution may be possible depending on overall parameters (zero-IF, band-pass sigma delta conversion, filtering and sub-sampling ...)

4.2.2.2 Homodyne architecture

Basic principle

In the direct conversion (or zero-IF) architecture, the RF band of interest is directly translated to baseband, and the nearby interferers are suppressed by a low-pass filter (cf. Figure 4-3). The direct conversion receiver architecture has become popular for existing cellular and WLAN systems due to the high level of integration. This architecture presents many advantages. First, it is very simple and requires few components: an RF filter, a LNA, a mixer, a LO, and a low-pass filter to select the channel. Furthermore, direct conversion requires no image-reject filter because the IF is zero. As there is no image signal, the constraint of selectivity on the RF filter is also relaxed. The other advantage of direct conversion is that the IF filters and IF amplifier can be integrated because the IF signal is at base-band. The power consumption is also low because most of the power gain is obtain at base-band. So, direct conversion architecture is a good solution to integrate the entire RF front-end of a receiver.

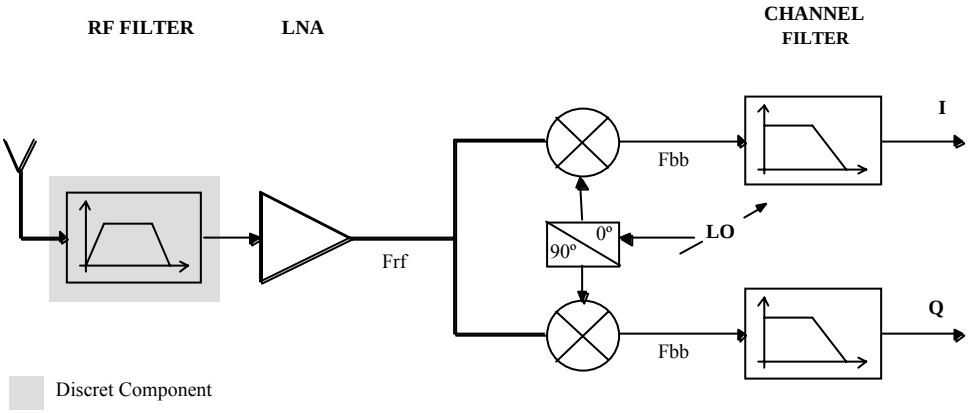

Figure 4-3: Homodyne Architecture.

This architecture can be considered as a very good candidate for the integration of the receiver in the context of the kind of system covered by the PHYDYAS project. That's the reason why we have made a deeper analysis of its advantages and drawbacks.

Advantages

- Image Rejection

  In homodyne architecture, the wanted channel is directly down-converted to base-band. To distinguish between positive and negative IF frequencies which correspond to the upper and lower side-band of the RF signal, two mixers are used to generate a complex signal. The IF is supposed to be zero. Therefore, the image frequency of a channel consists of this channel itself. By this way, the problem of image rejection is circumvented.

- Channel Selectivity Filters

  The need of high quality factor band-pass filters is alleviated since the channel selectivity filter consists, now, of a low-pass filter. Therefore, the passive component does no longer

determine the centre frequency of the bandwidth of the filter which is now 0 Hz. Consequently, the channel selectivity filter can be fully integrated since there is no more need in accurate and high quality passive components. Power consumption of the filter is reduced since filter poles are located at the minimum possible frequency.

- Reduction of complexity

  Several key advantages can be deducted from the reduction of the complexity of the receiver architecture.
  - External Components: If external components are avoided, it allows higher impedance levels to be used between cascaded blocks. The power consumption will be reduced accordingly. Full integration of the receiver also reduces possible cross-talk between stages. This cross-talk is even more reduced as the IF is very low.

  - Local Oscillator: In zero-IF architecture, only one oscillator is required in the receiver (with in-phase and quadrature component). Moreover, it may have the same frequency as the transmitter in Time Division Duplex Systems. However, full compatibility will depends on the switching time accorded between reception and transmission.

Drawbacks

- Multi-path System

  In zero-IF architecture, as in all multi-path systems, the image rejection depends on the matching between the two paths, as well as on the phase and amplitude precision in the quadrature oscillator. The use of a two path topology also results in an increase of the power consumption. Moreover, for most phase and frequency modulation schemes, the front-end incorporates quadrature down-conversion. Any mismatch between the amplitude and/or phase of the two paths (I and Q) degrades the SNR. But this is much less troublesome in direct conversion than in image-reject architectures.

- Low-Frequency Components

  - LO Leakage: A major problem in zero-IF receivers is the DC-offset which is created during the down-conversion. The isolation between the LO-port and the RF-port of the mixer is not perfect (due to capacitive and substrate coupling). The leakage signal mixes with itself, which gives a DC component superimposed on the wanted signal in the base-band. A similar effect may occur if a large interferer leaks from the LNA to the LO-port of the mixer. A change in frequency and environment (coupling) changes the amount of cross-talk and the resulting DC level. This phenomenon has two consequences. The high level of the DC signal will cause saturation of the following stages and the low-frequency noise will degrade the sensitivity of the receiver. A low frequency high-pass filter may remove these components for modulations compatible with such filters.

  - Flicker noise: As only modest filtering occurs before the down-conversion, the dynamic range of the following stages is quite important. In CMOS technology, the input noise of these stages will be dominated by $1/f$ noise (which can be

easily orders of magnitude larger than thermal noise). The reduction of this noise will be obtained by an increase in the area of MOS transistor, which will result in an increase in power consumption. Flicker noise can be cancelled in switched capacitor circuitry using correlated double sampling. However, a continuous time anti-alias filter will still be needed.

- Zero-IF Particularity

  In classical front-end architecture, inter-modulation products in the desired channel are generated only by odd-order harmonics. In homodyne architecture, even-order distortion can also be a source of noise. Therefore, constraints on the IP2 (second-order intercept point) may be even more severe than for the third-order one.

4.2.2.3 Low-IF architecture

Basic principle

The low-IF architecture is based on the direct conversion. However, the IF is not zero but a low frequency in the order of the signal bandwidth to get rid of low frequency troubles. The basic principle is illustrated in Figure 4-4. To take advantage of the two-path architecture, it is possible to use complex analog filtering as well as complex analog-to-digital conversion.

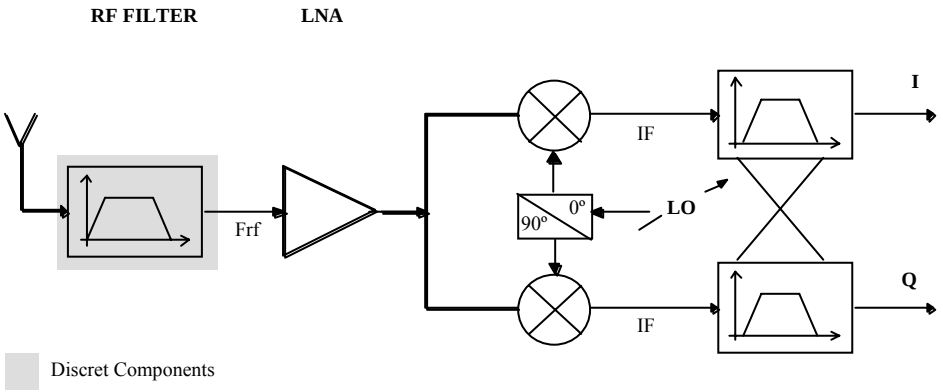

Figure 4-4: Low-IF architecture.

A low IF in a heterodyne architecture would imply very high constraints on the RF filter, which makes it unrealizable. In the low-IF architecture, by using a multi-path topology, the mirror signal and the desired signal are easily separable so the mirror signal suppression can be done in the IF part. The constraint on the RF filter is then relaxed so that it can be realizable with this low IF. Furthermore, the IF filters are low Q band-pass filters that can be integrated as easily as the IF low-pass filters in zero-IF topology. One of the key points, namely the high level of integration is reached with a low-IF architecture since no expensive external high Q filters are used and most of the blocks are integrated. Moreover, this architecture consumes low power because most of the components work at low frequency, the main gain is obtained at this low frequency and simple filters are used. The low IF topology is also a good way to resolve the main drawback of zero-IF which is its sensitivity to DC offset. Indeed, the low-IF topology is insensitive to parasitic baseband signals like DC offset voltages and self-mixing products caused by crosstalk between the RF and

LO signals. The major limitation of the low-if architecture is its requirement of good image signal suppression, because in contarst to zero-IF, the image signal exists and can be larger than the wanted signal as it is located out of desired channel. The image rejection capability is directly linked to the matching between the two paths.

As the low-IF architecture is very close to the zero-IF architecture, which is the primary candidate for full integration, we have extracted advantages and drawbacks of this topology compared to the previous one.

Advantages

- Low-Frequency Components

  The most important advantage of such an architecture is the desensitization to the existing low-frequency components (DC offsets and $1/f$ noise). This is a critical point in CMOS implementation of an RF front-end.

- Multi-Path System

  A good way to relax constraints on mirror signal suppression is to put this undesired signal band where it is known that the power spectrum will be lower than that of the desired signal. So, a judicious choice of the IF is such that the unwanted mirror band is situated at frequencies where no signal exists. In this case, the matching requirements are even relaxed compared to zero-IF architecture. However, this is not always possible.

- Zero-IF Specificity

  Depending of the exact value of the IF, the constraints specific to the zero-IF architecture may be relaxed.

Drawbacks

- Multi-path System

  If it is not possible to find free frequencies, the image frequency will be probably located in an adjacent channel which may be much higher than the desired one. In that case, image rejection will give stringent constraints on the matching which are most often unfeasible.

  Depending of the channel bandwidth, the low-pass filter (of the zero-IF topology) may be replaced by a band-pass filter or have its bandwidth increased (which means in both cases an increase in the power consumption) .

4.2.2.4 Wide-Band IF architecture

Basic principle

An alternative architecture well suited for full integration is the wideband IF with double conversion. As in the super-heterodyne architecture, the frequency translation is made in two steps, according to the basic scheme given in Figure 4-5. At the first step, the whole received spectrum is translated to the intermediate frequency by means of fixed oscillator frequency. A low-pass filter is then used to remove the up-converted frequency component. Thereafter, a second conversion stage translates the desired channel to base-band. The second oscillator is used to tune the channel. After that, the channel filtering can be done at base-band just like in the zero-IF architecture.

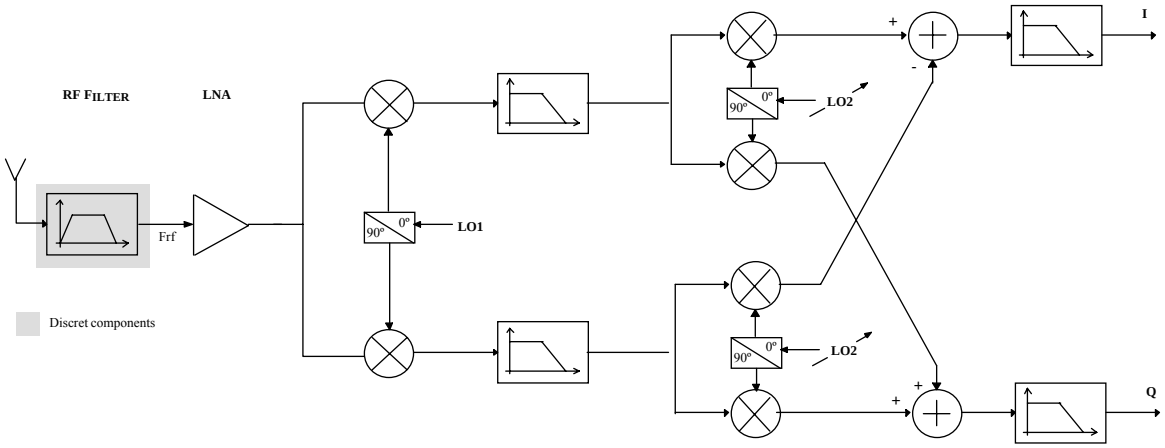

Figure 4-5: Wide-band IF with double conversion architecture.

As the channel selection is realized with the lower frequency tunable second LO, in order not to apply stringent constraints on the frequency oscillator, the intermediate frequency has to be high enough to keep a reasonable ratio between the tunable frequency range and the center frequency. Once more, this architecture is very close to the zero-IF architecture and analysis will be made by a close comparison to this previous architecture.

Advantages

- Frequency synthesizer

  The most important advantage of such an architecture is the relaxation of the requirements of the first oscillator whose integration is often critical. As, according to Figure 4-5, the frequency generated by the first oscillator is fixed, the noise requirements are easier to reach with an integrated VCO.

- Low-Frequency Components

  As the down-conversion to baseband is done in two steps, the mixer which translates the signal to zero-IF works at a much lower frequency than in the zero-IF architecture. Consequently, LO leakage is less critical and relatively constant, therefore, cancellation is easier.

Drawbacks

- Power consumption

  Compared to zero-IF architecture, this solution is much more complex (two oscillators are needed and 6 mixers) which leads to a high increase in power consumption.

- Multi-path System

  Due to the higher complexity of this multi-path system, the image rejection is more difficult to achieve because more cells are involved in the gain and phase matching. However, as the IF frequency is supposed to be quite high, the image rejection may be split between RF filter attenuation and two-path cancellation.

4.2.3 Sources of impairments

This section will first list the different RF impairment sources, explaining the origins of these impairments. Then, the modelling approach will be described. It has the advantage of being non architecture dependent.

4.2.3.1 DC offset

DC offsets mainly come from non-ideal isolation of the local oscillator, interference transposed in baseband by inter-modulation products in the mixer (direct conversion), and bad (or non-ideal) components. It is mainly dominant in the zero-IF architecture. DC offsets can be divided into a static part and a dynamic part: $V_s(t) = V_e(t) + \text{Statique}_{DC} + \text{Dynamique}_{DC}$. The static DC offset is applied during the whole simulation while the dynamic DC offset can be applied during a certain number of symbols. The static DC offset can also be considered to take into account the low frequency noise of the MOS transistor. This impairment is the main reason for having the central carrier unused in most multicarrier systems. This allows the RF designer to resort to zero-IF architecture in order to reduce the number of external components.

4.2.3.2 Phase noise

The phase noise is the noise which affects on the local oscillator signal and which is multiplied to the received signal when down-converting the RF signal to baseband. Its effect depends on the way down-conversions are applied to the received signal, as shown in the previous section. The phase noise also translates into jitter when the reference frequency is used to generate the clock of an ADC. The jitter is sometimes considered as a Gaussian error in time, which is a mistake. Moreover, the noise jitter can be correlated to the phase noise or not. This depends on the considered frequency. It is important to take into account the architecture of the used frequency synthesizer to have a good model of the frequency characteristics of this noise. This is discussed in the following section.

4.2.3.3 Spurious effects

Parasitic signals, like harmonics or sub-harmonics of strong spectral components, are generated by different active components in the receiver. They are considered often as pure sinusoids. Their frequencies are usually proportional to the reference, LO or IF frequency.

4.2.3.4 IQ Mismatch

The two quadrature paths (I and Q) of a receiver are usually unbalanced in analog implementations: There is an amplitude mismatch ε and a phase mismatch $\Delta\Phi$ between I and Q branches. This imbalance is mainly due to the imprecise generation of the quadrature signal by the local oscillator. The gain and phase imbalance is also partly due to the mismatch of gains and phases in the two amplification, filtering and AD-conversion chains. The mismatch is usually very critical in the low-IF architecture, and also in zero-IF architecture with high-order modulations.

4.2.3.5 Frequency offset

The frequency offset between the receiver and the transmitter is due to the local oscillator quartz imprecision and temporal variations between two terminals. This is a well know problem covered by the baseband synchronization algorithms.

4.2.3.6 Non-linearities

The RF and analog active building blocks (from the LNA to the ADC) are, in practice, non-linear. This is well known for both the transmitter and the receiver. The main nonlinearities are the second-order and the third-order ones. The third-order non-linearity generates inter-modulation as shown in Figure 4-6.

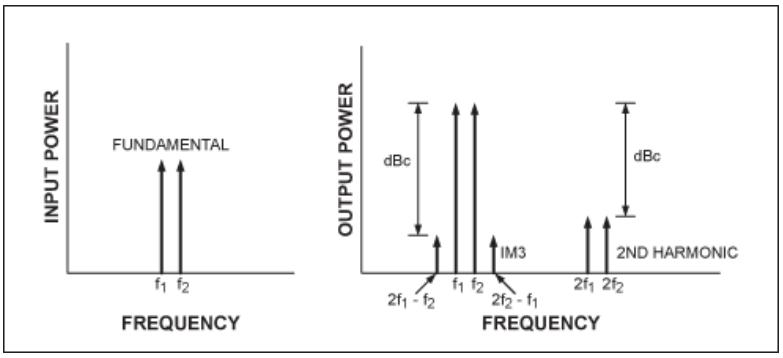

Figure 4-6: Intermodulation due to the receiver non-linearity.

4.2.3.7 Channel filter

The objective of the channel filter is to attenuate the adjacent channel signals in order to reduce the dynamic range of the incoming signal, and to allow the implementation of the analog to digital converter. This filter is characterized by a filter frequency response shape which can be represented as shown in Figure 4-7.

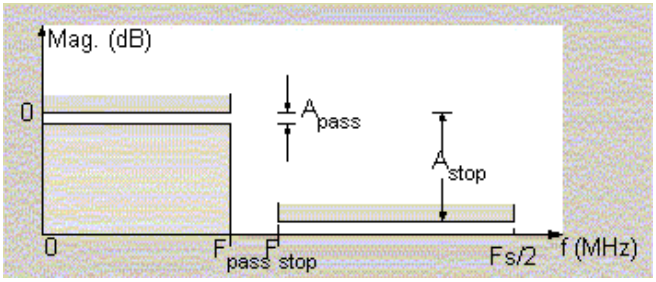

Figure 4-7: Filter frequency response shape.

In the transition band, the group delay of the filter may vary quite rapidly, which can be difficult to handle for the channel estimation system. As a consequence, some margin is needed between the highest carrier frequency and the frequency at which the gain of the filter start to decrease.

4.2.3.8 ADC impairments: clipping, quantisation noise

The analog to digital converter is a well known block. The saturation of this block is taken into account by adjusting the received signal level through automatic gain control. The quantization noise is also considered in the overall noise which is added in the receiver. The nonlinearity and the cyclic jitter should be also taken into account.

4.2.4 Modelling procedure

Even if the major sources of RF imperfections can be pointed out, it is relevant to consider imperfections as global consequences in a black box model in order to avoid architecture concerns. The chosen approach is illustrated in Figure 4-8.

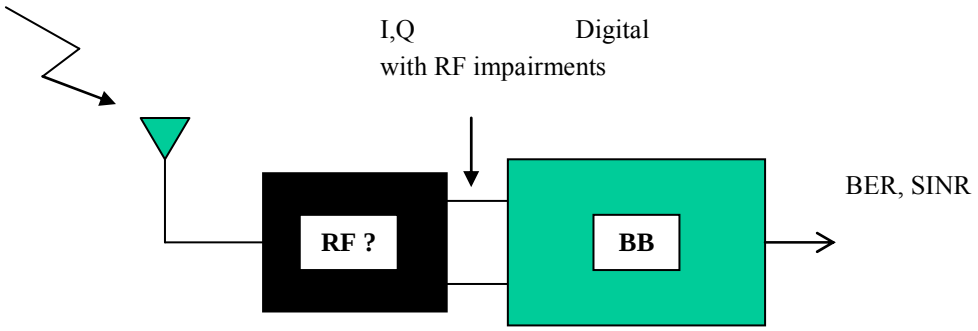

Figure 4-8: Chosen approach.

The idea is to evaluate the influence of RF impairments independently of the architecture itself by gathering all the potential impairments in the same black box model. Moreover, the idea is also to develop for each impairment some specific baseband level model in order to guarantee the feasibility of bit error rate (BER) level simulations. When using classical RF simulation tools, the simulations would be too slow to do BER simulations. The developed time-domain models are willingly simple and generic for low computational load, and easy analyse, without architecture concerns. More complex or dedicated ones could be implemented later. Some models developed are presented in the following section.

4.3 RF impairments

The aim of this section is to evaluate the sensitivity of the FBMC scheme against the impairments caused by the analog RF components of the transceiver front-ends and to compare the performance of FBMC with an equivalent system based on OFDM. Three RF impairments are studied below: the phase noise introduced by the oscillator and the mixers, the amplitude and phase imbalance between I and Q branches which typically occur in zero-IF receiver architecture and the non-linearity of the power amplifier located at the transmitter side. These impairments are considered because they can significantly impact the RF architectures described in Section 4.2 and have not yet been studied in the case on FBMC.

The first section presents a simulation framework set up in order to run RF impairment simulations with both FBMC and OFDM in identical conditions and with the same parameters. As a result, FBMC can be compared to OFDM in terms of error vector magnitude (EVM) at the receiver or by the gain or degradation of the signal to noise ratio (SNR) required for achieving a given BER.

The three next sections are devoted to each of the studied RF impairments. For each one, a numerical model is developed and implemented in the baseband simulation [33]; we present the model with its significance, expression and parameters and we explain their respective impacts on the FBMC system. Preliminary simulation results have been obtained and indications are given on the importance of each of the studied impairments on the FBMC system.

In the case of the phase noise, an analytical study of its impact on the FBMC modulation scheme is presented. Following an approach already developed in the literature in the case of OFDM [34], it is shown that the effect of the phase noise in an FBMC system can be separated in three components in the frequency domain: the common phase error (CPE), the inter carrier interferences (ICI) and the inter symbol interference (ISI). This last term is specific to FBMC. Analytical expressions are derived for the three components and we also provide expressions of two weighting functions which allow computing accurately CPE and ICI contributions from the knowledge of the power spectral density of the phase noise.

4.3.1 Baseband simulation framework

A baseband simulation chain of the FBMC system is developed under Matlab based on the filter bank structure described in Chapter 2 of this document. In parallel to this FBMC modulation/demodulation, a code was added in order to process an OFDM signal in identical simulation conditions and with the same parameters. Both FBMC and OFDM signals are synthesized, subjected to the same RF impairment model and demodulated. As a result, FBMC can be compared to OFDM in terms of error vector magnitude (EVM) at the receiver or by the gain or degradation of the signal to noise ratio (SNR) required for achieving a given BER.

A schematic of the FBMC/OFDM simulation framework is illustrated in Figure 4-9. Simulation parameters which are common to the generation of OFDM and FBMC signals are summarized in Table 4-1 and parameters which are specific to the FBMC system are given in Table 4-2.

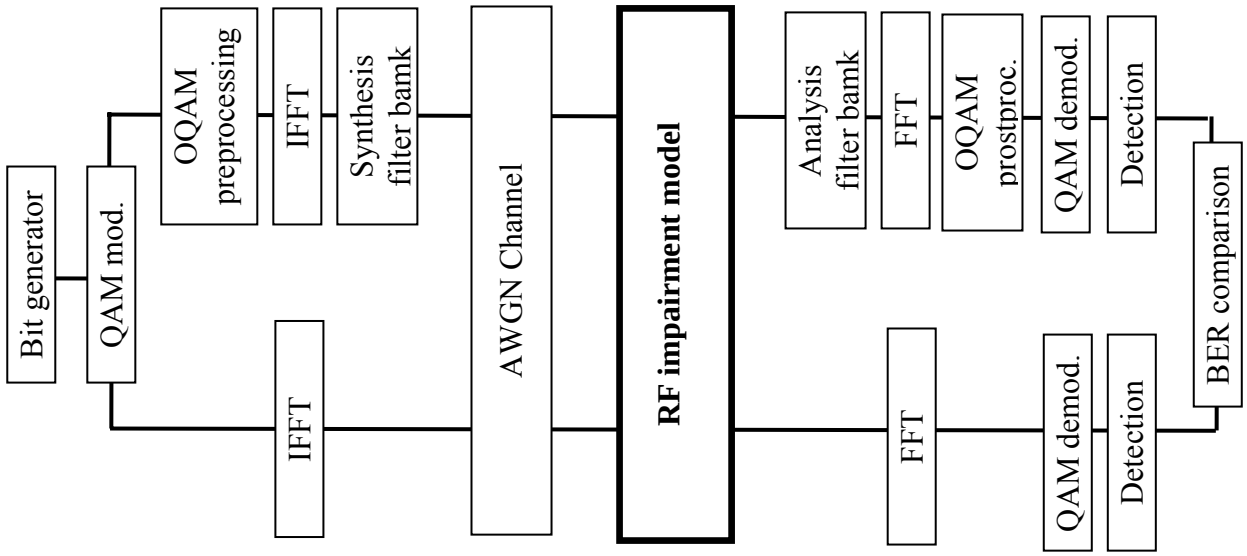

Figure 4-9: Schematic of the FBMC/OFDM baseband simulation framework for RF impairments studies.

Table 4-1: Common parameters for generation of OFDM and FBMC signals.

Parameter	OFDM	FBMC
# OFDM / FBMC symbols	800	
# data bits	4.10^5	
Sampling frequency	10 MHz	
Subcarrier modulation	QPSK	
FFT size	256	
# data sub carriers	250	
Bandwidth	9.76 MHz	
Sub-carrier spacing	39.06 KHz	
SNR range	[-5,30] dB	

Table 4-2: Parameters for filter bank prototype synthesis.

Parameter	Value
M	256
α	1
K	4
$\overline{P}_0$	1
$\overline{P}_1$	0.97195983
$\overline{P}_2$	1/sqrt(2)
$\overline{P}_3$	0.23514695

Limitation: The present simulation chain does not take every aspects of a real communication system into account. The synchronization is ideal. The propagation channel is modeled as Additive White Gaussian Noise (AWGN). Only one RF impairment is simulated at the same time. No interleaving, or coding scheme is used. Using such an ideal simulation, we expect to be able to understand how each impairment impacts the system and to explain how both FBMC and OFDM modulations schemes can be differently impacted.

Reference simulation: A reference simulation is run in order to validate the modulation and demodulation process for each modulation scheme. In this reference simulation, no RF impairment is modelled, the channel is AWGN, and the SNR is varied in order to obtain a curve of BER as a function pf the SNR. In such condition, it can be verified that both OFDM and FBMC modulation schemes give identical performances in terms of BER versus SNR.

Numerical accuracy: The number of OFDM/FBMC symbols (see Table 4-1) of each simulation is chosen in order to obtain a numerical accuracy below 1 dB for the SNR for a BER of 10^{-4}. The number of symbol is a trade-off between accuracy and the simulation time.

4.3.2 Phase noise

4.3.2.1 Analytical studies

The effect of the phase noise in an OFDM system has been extensively studied in the literature, as in [34]. It can be separated in two contributions: CPE and ICI. In this section, we first present the calculation of these expressions in the case of the OFDM and based on the same approach, we show that similar expressions of these phase noise components can be calculated for FBMC. Closed form expressions are given for the CPE and ICI and it is shown that a third contribution of the phase noise also appears in term of inter symbol interference (ISI). This ISI phase noise component is specific to FBMC. Finally, following an approach developed in [34] for OFDM, we show that the amount of these effects (CPE, ICI and ISI) in an FBMC system can be evaluated from the knowledge of the phase noise spectrum using weighting functions.

Phase noise components in OFDM systems

Phase noise in a given OFDM receiver brings two components in frequency domain: CPE and ICI. These components are pointed out in the calculus beneath.

Let's $[X_1, X_2, \ldots, X_N]$ be the OFDM signal (or pilot) to be transmited over N sub carriers. At the transmitter, the IFFT output can be written as: $x_n = \frac{1}{N}\sum_{k=1}^{N} X_k e^{j2\pi\frac{kn}{N}}$. At the channel output and after RF to base band transposition, the signal is impaired by phase noise: $y_n = \frac{1}{N}\sum_{k=1}^{N} X_k H_k e^{j2\pi\frac{kn}{N}+\phi(n)} + w_n$ with $\phi(n+1) = \phi(n) + \varphi(n+1)$ (where $\varphi(n)$ is the realization of phase noise random variable).

At the FFT output: $Y_p = \frac{1}{N}\sum_{n=1}^{N}\sum_{k=1}^{N} X_k H_k e^{j2\pi\frac{k-p}{N}n} e^{j\phi(n)} + W_p$. By inverting the two sums, CPE and ICI can be separated and highlighted:

$$
\begin{aligned}
Y_p &= \frac{1}{N}\sum_{k=1}^{N} X_k H_k \sum_{n=1}^{N} e^{j2\pi\frac{k-p}{N}n} e^{j\phi(n)} + W_p \\
&= \frac{1}{N} X_p H_p \sum_{n=1}^{N} e^{j\phi(n)} + \frac{1}{N}\sum_{k=1,k\neq p}^{N} X_k H_k \sum_{n=1}^{N} e^{j2\pi\frac{k-p}{N}n} e^{j\phi(n)} + W_p \\
&= X_p H_p I_{CPE} + \sum_{k=1,k\neq p}^{N} X_k H_k I_{ICI,k}(p) + W_p.
\end{aligned}
$$

Common Phase Error: $I_{CPE} = \frac{1}{N}\sum_{n=1}^{N} e^{j\phi(n)}$

This complex gain is common to all sub carriers. It is the DC part of the phase noise for the considered symbol. It must be understood that this value is a realization from a random variable, which differs from one symbol to another.

Inter Carrier Interference: $I_{ICI,k}(p) = \frac{1}{N}\sum_{n=1}^{N} e^{j2\pi\frac{k-p}{N}n} e^{j\phi(n)}$

This subcarrier interference term can be seen as a white Gaussian phase noise when the number of sub carriers is large enough. It also differs from one subcarrier symbol p to another.

The frequency domain signal is then given by: $Y_p = X_p H_p I_{CPE} + \sum_{k=1-p,k\neq 0}^{N-p} X_k H_k I_{ICI,k}(p) + W_p$

Figure 4-10 illustrates where the resulting frequency components of phase noise come from in time domain. The mean of the phase noise realization brings the CPE value. The higher order components of the phase noise realization, decomposed in DFT base, bring interference from adjacent sub carriers.

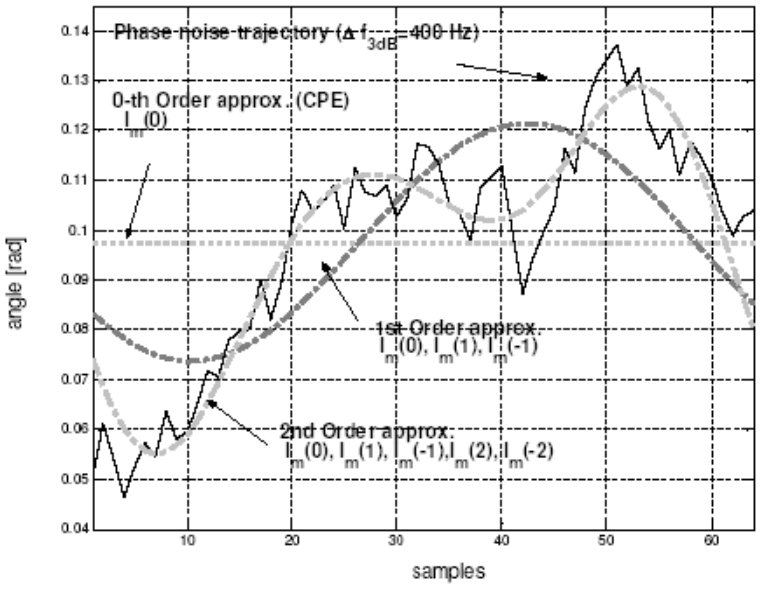

Figure 4-10: Phase noise realization and approximation in DFT base.

Thus phase noise realization can be approximated by the CPE and a few inter carrier interference terms, brought back to time domain.

Effect on channel estimation:

CPE and ICI cause degradation on channel estimation. Channel estimation roughly gives: $\hat{H}_p = H_p I_0 + \sum_{k=1-p,k\neq 0}^{N-p} \frac{X_k}{X_p} H_k I_k + \frac{W_p}{X_p}$. If channel estimation is made for every symbol thanks to scattered pilots, receiver perceives a common phase error different for each symbol included in the channel and corrects it along with equalization. If not, CPE has to be detected and compensated. Inter carrier interference behaves like a white Gaussian noise which can be combined with thermal white Gaussian noise in an MMSE equalizer.

Phase noise components in FBMC systems

Let $x_k(n)$ be the FBMC signal to be transmitted over M sub carriers. Index k refers to the kth path, while index n refers to the FBMC symbol number in time.

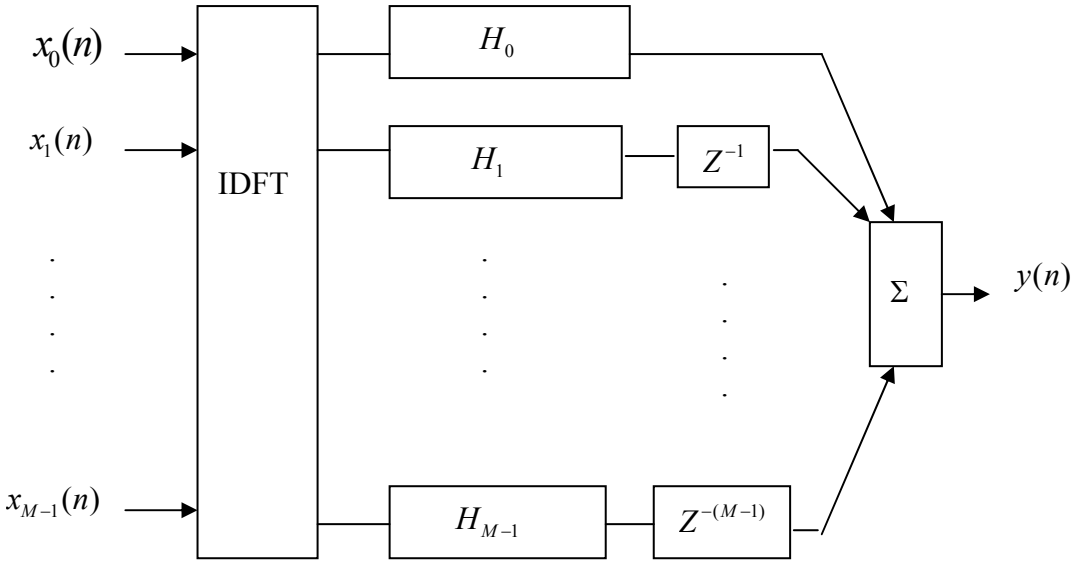

Figure 4-11: Synthesis filter bank.

At the transmitter, the synthesis filter bank output can be written as:

$$y(n) = \frac{1}{M} \sum_{m=0}^{M-1} \sum_{k=0}^{K-1} h_m(n-k) x_m(k) e^{j2\pi \frac{mn}{M}}.$$

At the channel output and after RF to base band conversion, the signal is impaired by phase noise:

$$yc(n) = \frac{1}{M} \sum_{m=0}^{M-1} \sum_{k=0}^{K-1} h_m(n-k) x_m(k) e^{j2\pi \frac{mn}{M} + \phi(n)} + w_n.$$

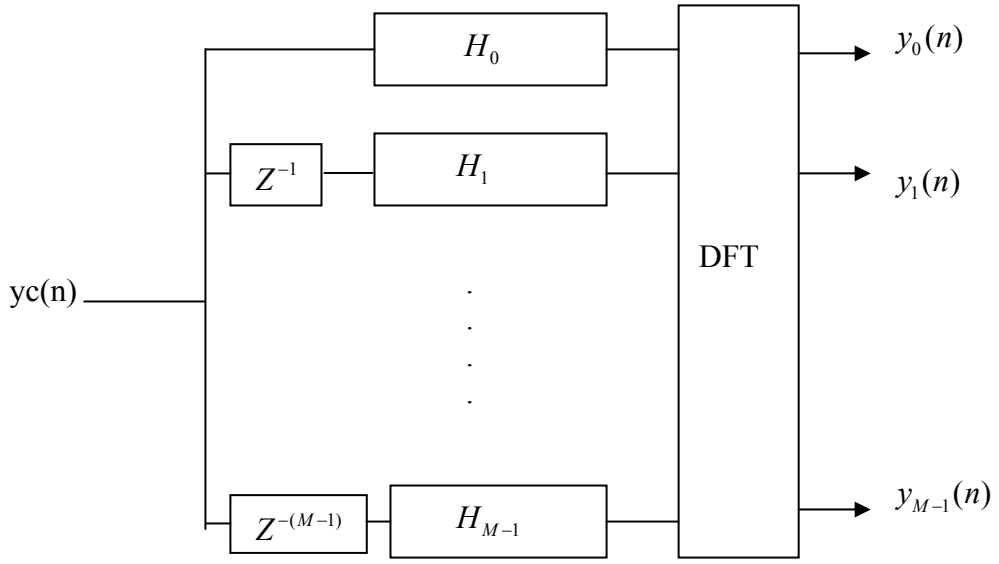

Figure 4-12: Uniform analysis filter bank.

At the analysis filter bank output:

$$y_p(n) = \sum_{q=0}^{M-1}\sum_{l=0}^{K-1} g_q(n-l)yc(l)e^{-j2\pi\frac{pq}{M}}$$
$$= \frac{1}{M}\sum_{q=0}^{M-1}\sum_{m=0}^{M-1}\sum_{l=0}^{K-1}\sum_{k=0}^{K-1} g_q(n-l)h_m(l-k)x_m(k)e^{j2\pi\frac{ml-pq}{M}+\phi(l)} + W_p.$$

One can take apart CPE, ISI, and ICI:

$$y_p(n) = x_p(n)\cdot\frac{1}{M}\sum_{q=0}^{K-1}\sum_{l=0}^{K-1} g_q(n-l)h_p(l-n)e^{j\phi(l)}$$
$$+\frac{1}{M}\sum_{k\neq n}^{K-1} x_p(k)\sum_{q=0}^{K-1}\sum_{l=0}^{K-1} g_q(n-l)h_p(l-k)e^{j\phi(l)}$$
$$+\frac{1}{M}\sum_{m\neq p}^{M-1}\sum_{q=0}^{M-1}\sum_{l=0}^{K-1}\sum_{k=0}^{K-1} g_q(n-l)h_m(l-k)x_m(k)e^{j2\pi\frac{m-p}{M}q+\phi(l)} + W_p$$
$$= x_p(n)\cdot I_{CPE} + \sum_{k\neq n}^{K-1} x_p(k)\cdot I_{ISI,k} + \sum_{m\neq p}^{M-1}\sum_{k=0}^{K-1} x_m(k)\cdot I_{ICI,m,k}(p) + W_p.$$

The PR condition of the filter banks assumes that:

$$\frac{1}{M}\sum_{q=0}^{K-1}\sum_{l=0}^{K-1} g_q(n-l)h_p(l-n) = 1.$$

.

When considering phase noise, the received signal is impaired by a random complex gain on every subchannel (i.e., CPE), and interference.

Common Phase Error: $I_{CPE} = \frac{1}{M}\sum_{q=0}^{K-1}\sum_{l=0}^{K-1} g_q(n-l)h_p(l-n)e^{j\phi(l)}$

The same way as in OFDM, this complex gain is common to all sub carriers. It is the DC part of phase noise for the considered symbol. It must be understood that this value is a realization from a random variable, which differs from one symbol to another.

Inter Symbol Interference: $I_{ISI,k} = \frac{1}{M}\sum_{q=0}^{K-1}\sum_{l=0}^{K-1} g_q(n-l)h_p(l-k)e^{j\phi(l)}$

Inter Symbol Interference correspond to the interference symbols received in the same subchannel due to time jitter in the filter bank.

Inter Carrier interference: $I_{ICI,m,k}(p) = \frac{1}{M}\sum_{q=0}^{K-1}\sum_{l=0}^{K-1} g_q(n-l)h_m(l-k)e^{j2\pi\frac{m-p}{M}q+\phi(l)}$

These terms are a mixture of ICI from the considered symbol and from neighbour symbols.

Weighting functions in OFDM systems

The phase noise weighting functions have been defined in [34] for OFDM systems. With the assumption of weak phase noise with respect to the carrier, the normalized variance of CPE and ICI are defined in OFDM systems by:

$$\sigma_{CPE} = \int_{-\infty}^{\infty} \mathrm{sinc}^2\left(\frac{f}{f_u}\right)|\Phi(f)|^2\,df \quad \text{(CPE)}$$

$$\sigma_{ICI,p} = \sum_{k\neq p}^{N}\int_{-\infty}^{\infty} \mathrm{sinc}^2\left(\frac{f}{f_u}\right)|\Phi(f-|k-p|\cdot f_u)|^2\,df \quad \text{(ICI)}$$

where f_u is the symbol frequency and $\Phi(f)$ the power spectral density of the phase noise. Then the phase noise weighing functions are expressed by:

$$W_{CPE}(f) = \mathrm{sinc}^2\left(\frac{f}{f_u}\right)$$

$$W_{ICI,p}(f) = \sum_{k\neq p}^{N}\mathrm{sinc}^2\left(\frac{f}{f_u}-|k-p|\right).$$

The integration of the "weighted" phase noise PSD over the signal bandwidth gives the signal to interference plus noise ratio in the presence of phase noise is shown in Figure 4-13

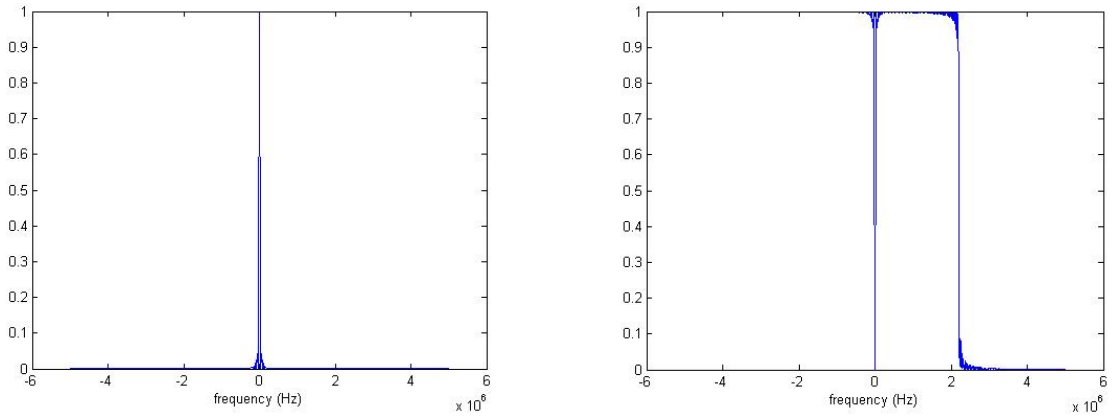

Figure 4-13: Phase noise weighting functions for OFDM. Left: CPE weighting function, right: 200th sub carrier ICI weighting function.

Weighting functions in FBMC systems

In the same way, in FBMC systems, CPE, ISI and ICI can be expressed by weighting functions. The expression for the CPE weighting function is:

$$I_{CPE} = \frac{1}{M}\sum_{q=0}^{K-1}\sum_{l=0}^{K-1} g_q(n-l)h_p(l-n)e^{j\phi(l)} \approx 1 + j\frac{1}{M}\sum_{l=0}^{K-1} g_p(n-l)h_p(l-n)\phi(l).$$

As $g_p(n-l) = h_p^*(l-n)$, we get:

$$I_{CPE} \approx 1 + j\frac{1}{M}\sum_{l=0}^{K-1} |g_p(n-l)|^2\phi(l).$$

Then

$$\sigma_{CPE} \approx \int_{-\infty}^{\infty} \mathrm{sinc}^2\left(\frac{f}{f_u}\right)|H(f)|^4\,|\Phi(f)|^2\,df$$

As a result if $H(f)$ if almost flat over the bandwidth of one sub carrier, the CPE variance of FBMC becomes equal to the CPE variance of OFDM. The expression for the ISI weighting function is:

$$\begin{aligned} I_{ISI,k} &= \frac{1}{M}\sum_{q=0}^{K-1}\sum_{l=0}^{K-1} g_q(n-l)h_p(l-k)e^{j\phi(l)} \\ &\approx \frac{1}{M}\sum_{q=0}^{K-1}\sum_{l=0}^{K-1} g_q(n-l)h_p(l-k) + j\frac{1}{M}\sum_{q=0}^{K-1}\sum_{l=0}^{K-1} g_q(n-l)h_p(l-k)\phi(l). \end{aligned}$$

$$\sigma_{ISI,p} = E[X_p]\sum_{k\neq n}^{M}\int_{-\infty}^{\infty} \mathrm{sinc}^2\left(\frac{f}{f_u}\right)|G(f)|^2\,|H(f+|k-n|\cdot f_u)|^2\,|\Phi(f)|^2\,df \quad \text{(ISI)}.$$

Conclusion

It was shown how the phase noise effects in an OFDM system can be expressed analytically, broken down in several contributions and quantified from the knowledge of the phase noise spectrum using analytical weighting functions easy to implement. Using a similar approach, the same expressions can be obtained in the case of FBMC and lead to specific tools useful in order to specify the RF subsystem phase noise requirements in the frame of an FBMC implementation. A next study in the frame of PHYDYAS will aim at finalizing the derivation, validation and implementation of these closed form expressions.

4.3.2.2 Baseband model

The local oscillator introduces a random phase rotation $\Delta\Phi(t)$ to the received signal when it is down converted. Phase noise broadens oscillator spectrum as illustrated in Figure 4-14.

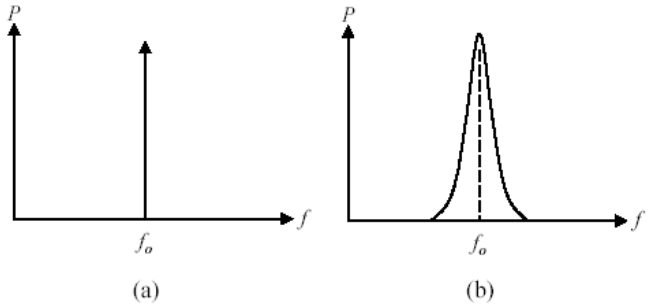

Figure 4-14: Oscillator spectrum. (a) Ideal, (b) With phase noise

The phase noise power spectral density of a free running oscillator is commonly modelled as the addition of two components (See Figure 4-15):

- A Gaussian Wiener process whose contribution asymptotically decays as $1/f^2$. In the following simulations, this contribution is parameterized by the power spectrum density relative to the carrier frequency (in dBc/Hz) at 1 MHz offset from the carrier frequency.
- A White Gaussian Noise Floor parameterized by its power spectrum density relatively to the carrier (in dBc/Hz).

In the time domain, the variance of the Wiener phase noise is a linear function of the time: $\sigma^2_{\Delta\Phi}(t) = 2Dt$ where D is the diffusion factor of the free running oscillator. Thus $\Delta\Phi(t)$ is modelled as a normal Gaussian random variable the variance of which increases linearly with the time. In order to integrate the diffusion factor in simulations, it must be scaled to the sampling frequency:$D_{Ts}(s) = D/f_s$. The Wiener phase noise is computed iteratively as follows:

$$\Delta\Phi_1(n+1) = \Delta\Phi_1(n) + X(n), \text{where } X(n) \sim N(0, 2D_{Ts}).$$

The noise floor is modelled by a white Gaussian noise of variance σ^2. Finally, the total phase noise is: $\Delta\Phi(n) = \Delta\Phi_1(n) + \mathrm{randn}(\sigma^2)$. A typical representation of the upper single side band of the phase noise is represented in Figure 4-15.

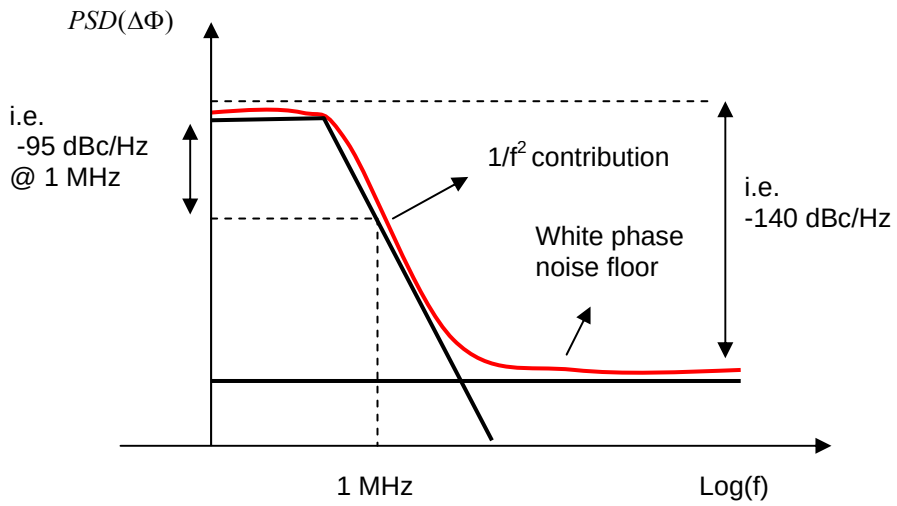

Figure 4-15: Typical power density spectrum (PSD) of a phase noise modelled as a Wiener process ($1/f^2$) and a noise floor.

In a multicarrier system, the $1/f^2$ phase noise is mainly localized below the subcarrier spacing and therefore it is essentially responsible for the CPE. This can be understood by observing the expression given for the CPE above, which is an integration of the phase noise spectrum within the subcarrier spacing. As a consequence, the sensitivity of the modulation scheme to the $1/f^2$ phase noise level can be qualitatively interpreted as its sensitivity to the CPE.

Contrary to the $1/f^2$ phase noise studied before, which rapidly decreases to become negligible at frequencies far away from the sub carrier, the white phase noise remains by definition constant on the spectrum. As a consequence, the white phase noise generated by a given sub carrier cause equal interference to all other sub carriers regardless of their distance to this sub carrier. On the other hand, it power level around the carrier frequency is negligible compared to the $1/f^2$ component. Thus the white phase noise will impact the system essentially by causing ICI and no CPE.

In a real system, the oscillator is usually controlled by a phase locked loop (PLL). As a consequence, the phase noise in the low part of its spectrum is dependent on the PLL which acts as a high pass filter. The frequency response of the PLL depends on a specific implementation and its effects are not taken into account in the present simulation. This means that the simulation is representative of a free running oscillator driven system.

4.3.2.3 Sensitivity of FBMC to phase noise

In practical receiver designs, the phase noise should not have a dominating effect on the link performance. Preliminary simulation results indicate that, if we consider the interesting uncoded BER region (around 1… 10%) and impairment values where the OFDM system has reasonable performance (e.g., performance degradation less than 2 dB due to RF imperfections), the phase noise sensitivity differences between FBMC and OFDM are not very significant. However, further studies are needed to confirm the results.

4.3.3 IQ imbalance

4.3.3.1 Base band model

The two quadrature paths of a receiver can be unbalanced: In analog implementations, there is usually amplitude mismatch ε and phase mismatch $\Delta\Phi$ between the I and Q branches. This can be illustrated by the figure below.

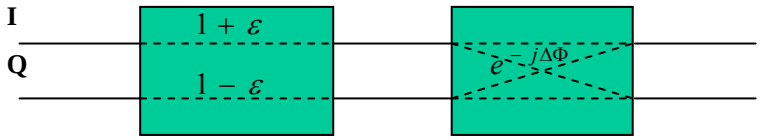

Figure 4-16 : IQ gain and phase mismatches.

Let's define the coefficients: $\alpha = \cos(\Delta\Phi) + j\varepsilon \sin(\Delta\Phi)$ and $\beta = \varepsilon \cos(\Delta\Phi) - j \sin(\Delta\Phi)$. Then, the output signal in time domain is: $V_s(t) = \alpha V_e(t) + \beta V_e(t)^*$

In the RF impairment model, α and β are calculated based on the gain and phase mismatch parameters. Then, the received signal is disturbed by its complex conjugate.

4.3.3.2 Sensitivity of FBMC to IQ imbalance

In OFDM systems, it is shown that the signal impaired by IQ imbalance can be expressed in the frequency domain as a linear mixture of the not-impaired signal and of a complex conjugate image of itself being flipped along the frequency axis. The two coefficients of this linear combination are linked to the value of the amplitude and phase imbalance between I and Q branches.

Since the subcarrier processing in the FBMC system operates differently than in classical QAM/OFDM, it is not straightforward to interpret how the IQ imbalance will affect the system and if the effect will be the same as in OFDM. In order to determine if IQ imbalance have a particular impact on FBMC regarding theses specificities, it appears feasible to carry out an investigation based on the analytical expression of the FBMC modulated signal to see if the contribution of the IQ imbalance impairment can be isolated. This will be a topic of a subsequent study.

Preliminary simulation results show that, in the interesting operation region, the I/Q imbalance sensitivity of OFDM and FBMC are rather similar. In modern RF design, the compensation of RF impairments is a serious possibility. This is especially true for I/Q imbalance compensation in multicarrier systems with high-order constellations. However, in such cases (i.e., when considering the performance with significant I/Q imbalance) the compensated performance and sensitivity to RF impairments are not necessarily very much related, so separate studies are needed to develop proper compensation methods and compare the resulting compensation performance.

4.3.4 Power amplifier non-linearity

4.3.4.1 Base band model

Front-end RF non-linearities come from all the active components at the receiver (low noise amplifier, mixer, etc…). These impairments are simulated by a polynomial function whose coefficients are computed based on the inter-modulation (IM) product values:

$$V_s(t) = \sum_{k=1}^{M} a_k V_e(t)^k.$$

For a 2-tones signal $V_e(t) = A\cos(w1t) + A\cos(w2t)$, inter modulation products appears when developing the third order polynomial $a_1 x + a_3 x^3$:

$$V_s(t) = \left(a_1 + \frac{9}{4}a_3A^2\right) A\cos(w1t) + \left(a_1 + \frac{9}{4}a_3A^2\right) A\cos(w2t) + \frac{3}{4}a_3A^3\cos(2w1 - w2) + \frac{3}{4}a_3A^3\cos(2w2 - w1).$$

The third order interception point (IP3) amplitude is computed thanks to polynomial coefficients:

$$A_{IP3} = \sqrt{\frac{4}{3}\left|\frac{a_1}{a_3}\right|}.$$

For $a_1 = 1$, we get:

$$a3 = \frac{4}{3A_{IP3}^2}.$$

With further developments we have also: $a5 = \frac{8}{5A_{IP5}^4}$.

IP3 determination:

Let's note $A_{IP3,s}$ the output IP3 amplitude, $A_{IP3,e}$ the input IP3 amplitude, A_s the output signal amplitude and A_e the input signal amplitude. We assume that output over input amplitude ratio are quite similar for inter modulation products and for signals.

Then, $A_{IP3,s} \approx A_{IP3,e}\frac{A_s}{A_e}$ so we get $a3 = \frac{4Gain^2}{3A_{IP3,s}^2}$. A_{IP3} is obtained by cascading the IP3 of the different reception chain components with the Norton formula (component by component).

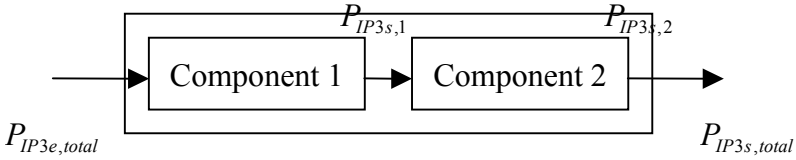

Figure 4-17: Norton formula illustration.

$$P_{IP3,total} = P_{IP3s,2} - 10\log\left(1 + \frac{1}{G2}\frac{P_{IP3s,2}}{P_{IP3s,1}}\right), \quad \text{where G2 is the gain of component 2.}$$

In the RF impairments model, only IM3 and IM5 are taken into account. Polynomial coefficients a_3 and a_5 are computed thanks to fifth order odd polynomial coefficients.

4.3.4.2 Sensitivity of FBMC to non-linearity

Again, in the interesting operation region where the link performance is not significantly affected, the differences between OFDM and FBMC are not very significant. In fact, the spectral re-growth effect due to the power amplifier linearity is expected to be more significant in determining the minimum back-off value. This will be an important topic in future studies.

4.3.5 Conclusion

A baseband simulation framework has been developed which allows carrying out comparative studies of FBMC and OFDM modulation schemes for different RF impairments in identical conditions. Three most significant RF impairments are addressed in this study: Phase noise, IQ imbalance and power amplifier non-linearity. Baseband simulation models were presented for each of them.

In the case of the phase noise impairment, an analytical study has been carried out. Closed-form expressions for calculating the impact of the phase noise in an FBMC system have been established. It is shown the phase noise impact can be broken down into several contributions: CPE, ICI, and ISI. These effects can be quantified from the knowledge of the phase noise spectrum using analytical weighting functions. This could lead in the development of a useful tool in order to specify the RF subsystem phase noise requirements in the frame of an FBMC implementation.

The preliminary results show that in the interesting operation regions, the differences between OFDM and FBMC are not very significant. However, due to some pecularities observed between FBMC and OFDM with respect to the studied RF impairments, the simulation chain needs additional improvement and validation in order to provide meaningful comparisons and general conclusions. Aspects needing further improvements include the choice of the common simulation parameters, the effects of various filter bank parameters, and the detection method used in the receiver. The final results of this study will thus be provided in the framework of the WP9 related to the demonstrator.

Perspectives following from this study include:

- Study of the spectral re-growth due to amplifier non-linearities.
- Completion of the analytical derivation, implementation and validation of the phase noise spectrum weighting functions.
- Analytical study of the IQ imbalance following an approach similar to the one proposed for the phase noise. That is to say, injecting the RF impairment expression in the analytical expression of the FBMC modulated signal and attempt to explicit its contribution in the new expression.

- Establish possible relationships of the filter bank system parameters (L, K, α, number of subcarriers, subcarrier interspacing) to the sensitivity to RF impairments and search for optimum solutions.
- The aim is to combine the simulation results with the analytical expressions in order to make the whole quantitatively consistent.
- The compensation of RF impairments is an interesting possibility in advanced RF designs. This is especially true for I/Q imbalance compensation with high-order constellations. However, in this context the compensated performance and the sensitivity to RF impairments are not necessarily very much related. Thus the RF impairment compensation possibilities have to be examined separately for FBMC systems.

5 Advanced TMUX techniques

In this section, certain advanced ideas and techniques related to FBMC are investigated. First, Section 5.1 explores possibilities to combine AFB and SFB of different sizes in the transmultiplexer configuration. Then Section 5.2 studies the use of a group of adjacent FBMC subcarriers in single-carrier -like transmission mode with reduced PAPR. This approach is an adaptation of the DFT-spread OFDM method, which has been selected for uplink transmission in 3GPP LTE.

5.1 Partial TMUX

This section presents a new approach to generate FBMC-modulated waveform. We focus on contiguous narrowband subcarrier allocation, which is often encountered in the uplink. Instead of using an M-subchannel SFB, the proposed scheme relies on a cascade of P-subchannel SFB ($P \ll M$), time domain interpolation, and a user-specific frequency shift. The new method allows constructing an uplink transmitter-receiver pair using synthesis and analysis filter banks of different sizes. The presented approach will be shown to provide notable computational complexity savings over a wide range of practical user bandwidth allocations when compared to the conventional implementation consisting of equally sized filter banks. Therefore, this novel scheme provides efficient and low-complexity synthesis of narrowband uplink waveforms well appreciated in mobile devices of future broadband communications.

5.1.1 Signal model

An efficient implementation structure for the FBMC transmitter processing is shown again in Figure 5-1.

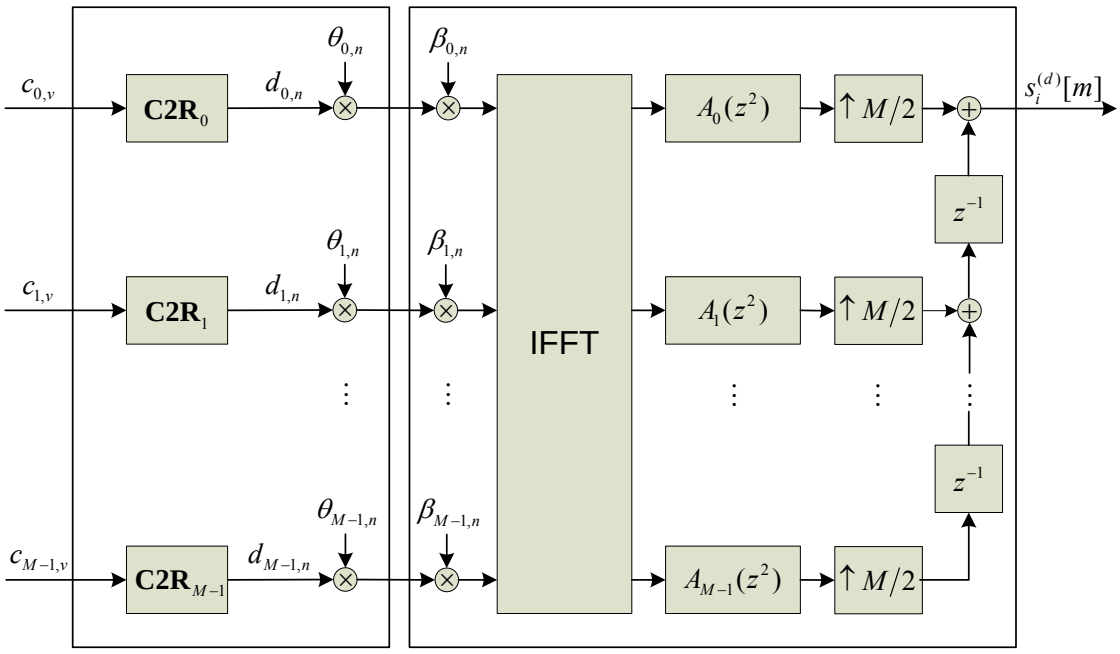

Figure 5-1: Efficient implementation structure of the transmitter processing in FBMC.

The discrete-time baseband signal of the ith uplink user, at the output of the M-subchannel (full-size) synthesis bank of an FBMC transmitter based on OQAM modulation, can be expressed as

$$s_i^{(d)}[m] = \sum_{k \in M_u^i} \sum_{n=-\infty}^{\infty} d_{k,n} \theta_{k,n} \beta_{k,n} p[m - n\frac{M}{2}] e^{j\frac{2\pi}{M}km}, \tag{48}$$

where

$$\theta_{k,n} = e^{j\frac{\pi}{2}(k+n)} = j^{k+n} \tag{49}$$

$$\beta_{k,n} = (-1)^{kn} \cdot e^{-j\frac{2\pi k}{M}(\frac{L_p-1}{2})}. \tag{50}$$

Here, m, M_u^i, $d_{k,n}$, and $\theta_{k,n}$ denote the sample index at high-rate (at the output of SFB), the set of active subcarriers of the ith user, the real-valued symbol modulated (at rate $2/T$) on the kth subcarrier during the nth symbol interval, and the phase mapping between the real-valued data sequence and the complex-valued input samples of the synthesis bank, respectively. T denotes the signaling interval defined as the inverse of the subcarrier spacing, i.e., $T = 1/\Delta f$. Symbols $d_{k,n}$ and $d_{k,n+1}$ can be interpreted to carry the in-phase and quadrature (I/Q) components, with a relative time offset of $T/2$ of a complex-valued symbol $c_{k,v}$ (of rate $1/T$) from a QAM alphabet.

5.1.2 Uplink waveform synthesis

Let us assume that the ith user is scheduled to a frequency-time slot that corresponds to an FBMC waveform carrying N_s OQAM multicarrier symbols on Q subcarriers, consecutive in frequency, according to a given band allocation $M_u^i = (\mathbf{q} + \xi) \bmod M$, where $\mathbf{q} = [0\ 1\ \cdots\ Q-1]^T$, $\xi \in \{0, 1, \ldots, M-1\}$ is the index of the active band edge subcarrier, and mod stands for the modulo operation. In practice, guard band subcarriers around the system band impose the following additional constraint for valid band allocations: $\xi + Q - 1 \leq M/2 - M_g$ or $\xi > M/2 + M_g$, where M_g denotes the number of guard band subcarriers.

5.1.2.1 Direct synthesis using M-subchannel filter bank

In the direct approach, the high-rate waveform is straightforwardly obtained by applying the M-subchannel synthesis structure of Figure 5-1. The length- M input vectors $\mathbf{c}(v)$ (for $v = 0, 1, \ldots, N_s - 1$) in accordance with the band allocation M_u^i, can be expressed as

$$\begin{aligned} \mathbf{c}(v) &= \mathbf{B}^{(d)} \mathbf{c}'(v) \\ &= [0\ \cdots\ 0\ c'_{0,v}\ \cdots\ c'_{Q-1,v}\ 0\ \cdots\ 0]^T \end{aligned} \tag{51}$$

where

$\mathbf{c}'(v) = [c'_{0,v}\ c'_{1,v}\ \cdots\ c'_{Q-1,v}]^T$ denotes a length-Q complex-valued symbol vector and

$$\mathbf{B}^{(d)} = \begin{bmatrix} \mathbf{0}_{\xi \times Q} \\ - - - - - \\ \mathbf{e}_1^T \\ \vdots \\ \mathbf{e}_Q^T \\ - - - - - \\ \mathbf{0}_{(M-\xi-Q)\times Q} \end{bmatrix} \tag{52}$$

denotes a $M \times Q$ permutation and expansion matrix. Moreover, $\mathbf{0}$ is a zero-matrix and $\mathbf{e}_i = [0\ \cdots\ 0\ 1\ 0\ \cdots\ 0]^T$ denotes the ith length-Q natural basis vector (with one as the ith element).

5.1.2.2 Generation based on partial synthesis using P-subchannel filter bank and time-domain interpolation

Figure 5-2 shows a block diagram of an alternative baseband processing for the generation of an FBMC uplink waveform.

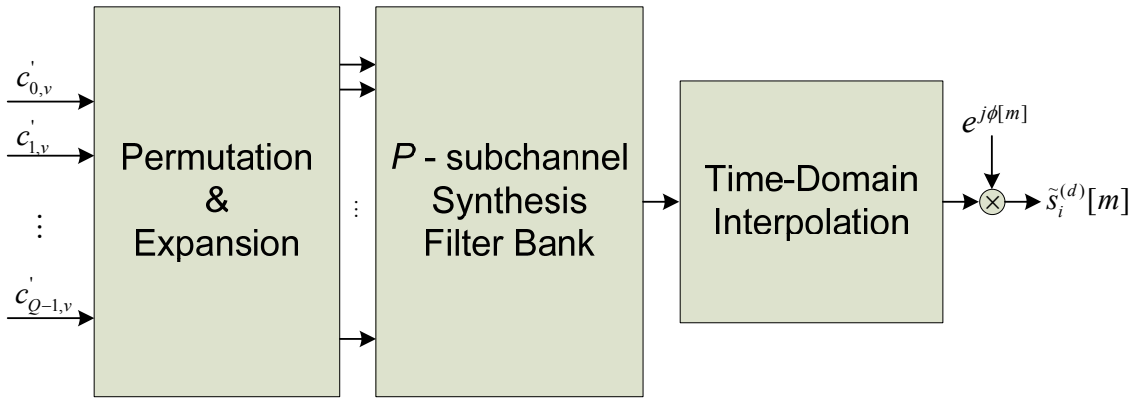

Figure 5-2: Block diagram of the partial synthesis scheme.

In the structure, referred hereafter to as the partial synthesis scheme, the high-rate waveform is constructed progressively using a cascade of initial waveform synthesis, time-domain interpolation, and user-specific frequency shift.

Initial waveform synthesis

At first, an initial low-rate waveform is obtained by means of a P-subchannel SFB, where the transform size (IFFT size) is defined by

$$P = 2^{\lceil \log_2 Q+1 \rceil}. \tag{53}$$

A baseband waveform, centered around the zero-frequency (exactly around zero for odd values of Q and with an offset of $\Delta f/2$ to the right of zero for even values of Q), is obtained by allocating the

data vectors $\mathbf{c}^{'}(v)$ to the last $\alpha_l = \lfloor (Q-1)/2 \rfloor$ and the first $\alpha_r = \lceil (Q+1)/2 \rceil$subcarriers (here $\lfloor \cdot \rfloor$ and $\lceil \cdot \rceil$ denote the floor and the ceil operation, respectively). Now, the chosen subcarrier allocation and the corresponding length-P input vectors $\mathbf{c}(v)$ are related through

$$\begin{aligned} \mathbf{c}(v) &= \mathbf{B}^{(p)}\mathbf{c}^{'}(v) \\ &= [c^{'}_{\alpha_l,v} \ \cdots \ c^{'}_{Q-1,v} \ 0 \ \cdots \ 0 \ c^{'}_{0,v} \ \cdots \ c^{'}_{\alpha_l-1,v}]^T, \end{aligned} \tag{54}$$

where

$$\mathbf{B}^{(p)} = \begin{bmatrix} \mathbf{e}^T_{\alpha_l+1} \\ \vdots \\ \mathbf{e}^T_{Q} \\ - - - - - \\ \mathbf{0}_{(P-Q)\times Q} \\ - - - - - \\ \mathbf{e}^T_{1} \\ \vdots \\ \mathbf{e}^T_{\alpha_l} \end{bmatrix} \tag{55}$$

denotes a $P \times Q$ permutation and expansion matrix. Moreover, a special attention must be paid to the pre-processing performed on the data vectors $\mathbf{c}^{'}(v)$ prior to the partial waveform synthesis using the P-subchannel synthesis bank. Specifically, it is necessary to match the subcarrier index and symbol index (denoted by k and n, respectively) -dependent pre-processing at the transmitter with that of the post-processing performed during demodulation in the M-subchannel analysis bank at the receiver. The required matching can be conveniently accomplished by performing for the kth subcarrier ($k = 0, 1, \ldots, P-1$) pre-processing of the subcarrier index

$$k^{'} = \big(k + \zeta\big) \mod M, \tag{56}$$

where

$$\zeta = \alpha_l + \xi \tag{57}$$

depends on both the bandwidth allocated (Q) and the desired position in the overall system band (ξ).

Time-domain interpolation

When the whole $Q \times N_s$ data segment, permutated, expanded, and pre-processed, is fed into the P-subchannel synthesis bank, an initial waveform $s_i^{(p)}[q]$ of $L_b^{(p)} = L_d^{(p)} + 2L_t^{(p)}$ samples in length is obtained. Here, $L_d^{(p)} = N_s P$ and $L_t^{(p)} = (K-1)P/2 + P/4$, denote the length of the body and the pre/post-tail of the waveform, respectively, where pre/post-tail refers to the pre/post- transient phase samples at the beginning/end of the waveform imposed by the impulse response of the prototype filter.

The synthesized low-rate partial waveform consists of samples, spaced $\Lambda = M/P$ samples apart, in the waveform generated by the M-subchannel reference design with zero-centered subcarrier allocation, i.e.,

$$s_i^{(p)}[q] = s_i^{(d)}[q\Lambda], \quad q = 0, 1, \ldots, L_b^{(p)} - 1. \tag{58}$$

This relationship is shown in Figure 5-3, where a short segment of the partial waveform $s_i^{(p)}[q]$, after upsampling by Λ, is compared to the high-rate reference waveform $s_i^{(d)}[m]$.

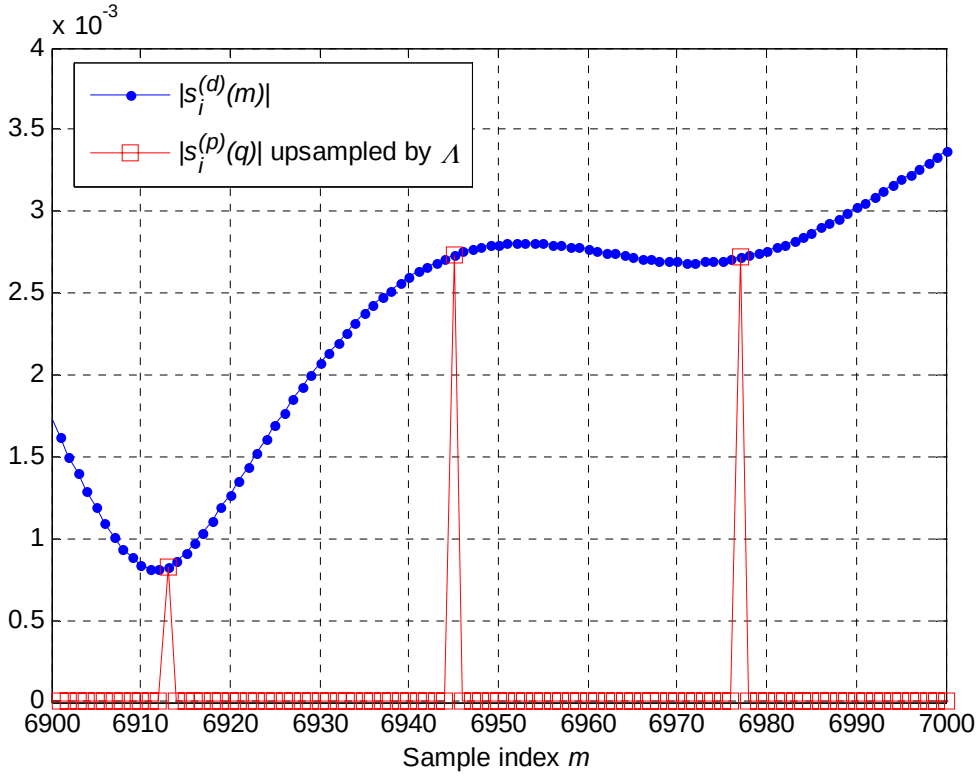

Figure 5-3: Relation between the low-rate partial ($s_i^{(p)}[q]$) and the high-rate reference waveform ($s_i^{(d)}[m]$): $Q = 15$, $P = 32$, and $M = 1024$ ($\Lambda = 32$).

Equation (58), therefore, clearly suggests time-domain interpolation by a power-of-two factor Λ, which is implementable as a cascade of upsampling by Λ and lowpass filtering, to obtain the high-rate waveform. Moreover, it turns the remaining partial synthesis problem into that of an interpolator design. The task of the interpolation filter is two-fold: to preserve the desired signal component at the baseband and to remove the spectral images due to the upsampling. The subcarrier allocation in Eq. (54), centers the user spectrum around the zero-frequency and therefore facilitates the use of a real-valued lowpass filter.

One choice for the required interpolation filter is a Λth-band (Nyquist) filter in which every Λth impulse response value is zero except for the center tap which is equal to $1/\Lambda$. When the required upsampling factor is large, the order of the filter becomes very high, since a filter with a very narrow transition band is required to meet the specifications. It is possible, however, to increase the sampling rate in a number of stages if Λ can be factorized into a product of integers. Such multi-

stage interpolation allows a gradual increase of the sampling rate leading to reduced computational/storage requirements and a significant relaxation in the characteristics of the anti-imaging filter at each stage. In our case, Λ is a power-of-two that results in $R = \log_2(\Lambda)$ stages. In every stage the upsampling factor is equal to two and each required filter, $H_r(z)$ for $r = 1, 2, \ldots, R$, can be a low-order halfband filter. The first halfband filter $H_1(z)$ takes care of the passband shaping, whereas the rest of the filters are used to attenuate the interfering images.

User-Specific Frequency Shift

During interpolation the spectrum of the waveform remains centered around the zero-frequency. In order to obtain the targeted waveform $\tilde{s}_i^{(d)}[m] \approx s_i^{(d)}[m]$, in accordance to the scheduled band allocation M_u^i, the interpolated high-rate baseband waveform $s_i^{(p)}[m]$ is transferred to the allocated position in the overall system band through a user-specific frequency shift, i.e.,

$$\tilde{s}_i^{(d)}[m] = s_i^{(p)}[m] e^{j\phi[m]}, \tag{59}$$

where

$$e^{j\phi[m]} = \exp\left(j\frac{2\pi\zeta}{M}m\right), \quad m = 0, 1, \ldots, L_b^{(d)} - 1$$

and $L_b^{(d)} = \Lambda L_b^{(p)}$.

5.1.3 Computational complexity

In this section, we compare the conventional direct and the presented partial approach, referred to as the FBMC-DS and FBMC-PS, respectively, from the arithmetic complexity point of view. The computational complexity of FBMC-DS and FBMC-PS are evaluated by calculating the number of real multiplications (C) required to generate a length-$L_b^{(d)}$ complex-valued high-rate waveform carrying N_s OQAM multicarrier symbols over a bandwidth allocation of Q-subchannels. FBMC-DS consists of the Q-point pre-processing, the Q-point multiplication by $\beta_{k,n}$-coefficients, the M-point IFFT, and the M-branch polyphase section. The overall number of real multiplications for the FBMC-DS structure, assuming IFFT implementation based on the Split-Radix algorithm [1], is

$$C^{(d)}(Q, M, N_s) = C_{SFB}(M) \cdot N_s \cdot 2, \tag{60}$$

where

$$C_{SFB}(M) = Q \cdot 2 + M\big(\log_2(M) - 3\big) + 4 + MK \cdot 2.$$

Correspondingly for the FBMC-PS, the overall number of real multiplications is obtained as a sum of the multiplications in different processing stages; the Q-point pre-processing, the Q-point multiplication by $\beta_{k,n}$-coefficients, the P-point IFFT, the P-branch polyphase section, the time domain interpolation, and the user-specific frequency shift:

$$C^{(p)}(Q, M, N_s) = C_{SFB}(P) \cdot N_s \cdot 2 + C_{int}(Q, M, N_s) + C_{fs}(M, K, N_s), \tag{61}$$

where

$$C_{SFB}(P) = Q \cdot 2 + P\big(\log_2(P) - 3\big) + 4 + PK \cdot 2$$
$$C_{int}(Q, M, N_s) = \sum_{r=1}^{R} \Big(\frac{N_r/2 + 1}{2}\Big) L_b^{(p)} \cdot 2^{(r-1)} \cdot 2$$
$$C_{fs}(M, K, N_s) = L_b^{(d)} \cdot 3.$$

Here again, the Split-Radix algorithm is assumed for the IFFT implementation. Moreover, the time-domain interpolator is considered to be implemented as a cascade of N_rth order halfband filters. The computational complexity estimate C_{int} ignores the trivial center tap (of a constant value of $1/2$) and exploits both the coefficient symmetry and the fact that every second sample of the input sequence is zero-valued. The frequency shift requires $L_b^{(d)}$ complex multiplications each of which can be calculated with three real multiplications and three real additions as shown in [1].

The computational savings of FBMC-PS are estimated using the following metric

$$\gamma(\%) = \frac{C^{(d)} - C^{(p)}}{C^{(d)}} \times 100. \tag{62}$$

It measures the relative reduction in the number of required real multiplications, by evaluating the percentage of the saved multiplication with respect to the amount required in FBMC-DS.

Figure 5-4 shows the computational savings γ as a function of waveform length in OQAM symbols $N_s \in \{5 : 5 : 100\}$ for various bandwidth allocations $Q \in \{5 : 20 : 245\}$ in case of filter bank design with $M = 1024$ and $K = 4$.

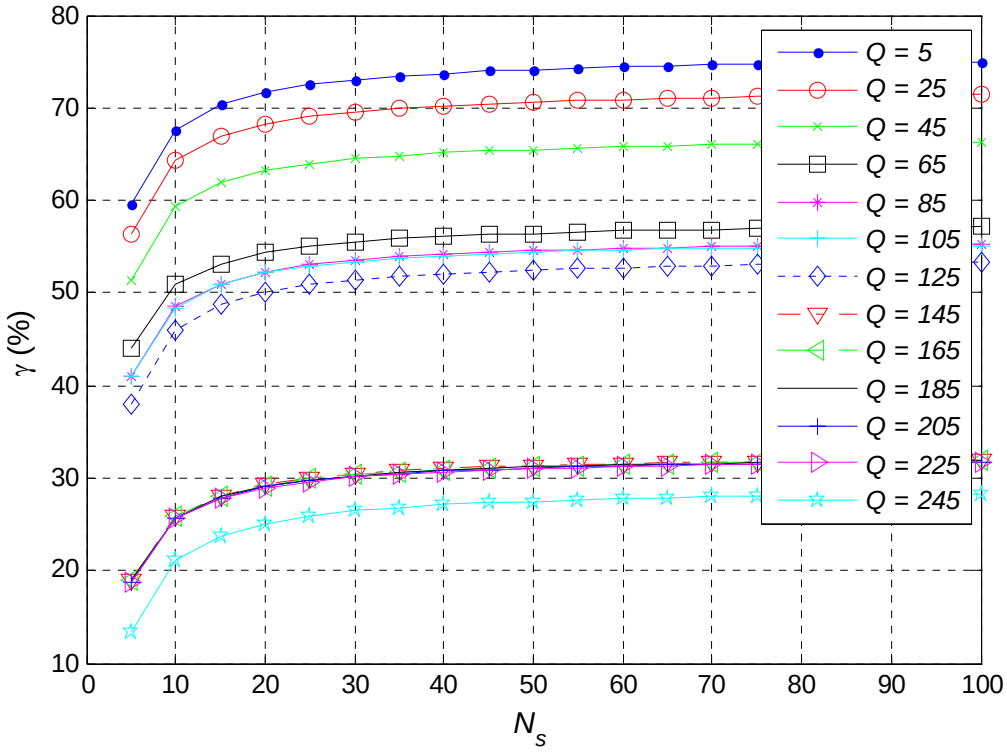

Figure 5-4: Computational savings (γ) of partial processing over direct approach as a function of waveform length in OQAM symbols (N_s) for various bandwidth allocations (Q) assuming filter bank design with transform size $M = 1024$ and overlapping factor $K = 4$.

It should be noted here that, the complexity of the interpolation stage depends on the order(s) of anti-imaging filter(s) through the specified stopband attenuation requirement(s). Here we consider an example design, where a cascade of halfband filters, providing a minimum of 70 dB attenuation on the image band(s) at different stages of the filter cascade, is assumed for time-domain interpolation. This specific choice of attenuation will be justified by the performance evaluations in the following section. Moreover, in the forthcoming numerical examples, we complemented the definition of the transform size of the partial synthesis in Eq. (53) with the following additional constraint: $P = 32$, for $Q \leq 16$. This condition provides a practical trade-off between the computational complexity savings and the latency introduced by the halfband interpolator for the most narrow band allocations. From Figure 5-4 the computational saving can be observed to be a gradually decreasing function of the allocated bandwidth. This trend is due to fact that with increasing bandwidth allocation the processing of FBMC-PS becomes gradually closer to that performed in FBMC-DS. The FBMC-PS structure, however, can be noticed to provide significant savings for bandwidth allocations up to approximately one fourth of the transform size $M = 1024$ of the direct synthesis.

The standard FFT algorithms inherently assume that the length of the input and output sequences are equal. This is clearly not an accurate assumption in the considered waveform generation context. Recall that only Q samples in the length-M (length-P) input vectors of the M-point (P-point) IFFT in the direct (partial) synthesis, are non-zero. In the literature, algorithms have been proposed to take advantage of the redundancy in the input sequence to improve the computational efficiency of the DFT. We refer to [35], where a comparison between a number of algorithms, developed for computing the DFT with only a subset of input or output points, is performed.

Here, we perform a computational complexity comparison between the direct and the partial waveform generation based on two DFT computation algorithms, discussed in [35] and found relevant to the problem in hand due to sparse IFFT input vectors. Specifically, we consider the FFT pruning algorithm developed by Skinner and the transform decomposition algorithm proposed by Sorensen and Burrus. Skinner's algorithm is obtained by pruning the decimation-in-frequency algorithm, whereas the transform decomposition algorithm is based on a mixture of a Cooley-Tukey FFT and Horner's polynomial evaluation scheme. A reader interested in details of these algorithms is guided to [35] and the references therein.

Figure 5-5 shows the computational savings, with respect to the direct approach based on the Split-Radix algorithm (S-R), as a function of bandwidth allocation (Q) assuming IDFT implementation based on the Skinner's FFT pruning algorithm (SP), and the transform decomposition algorithm (TD).

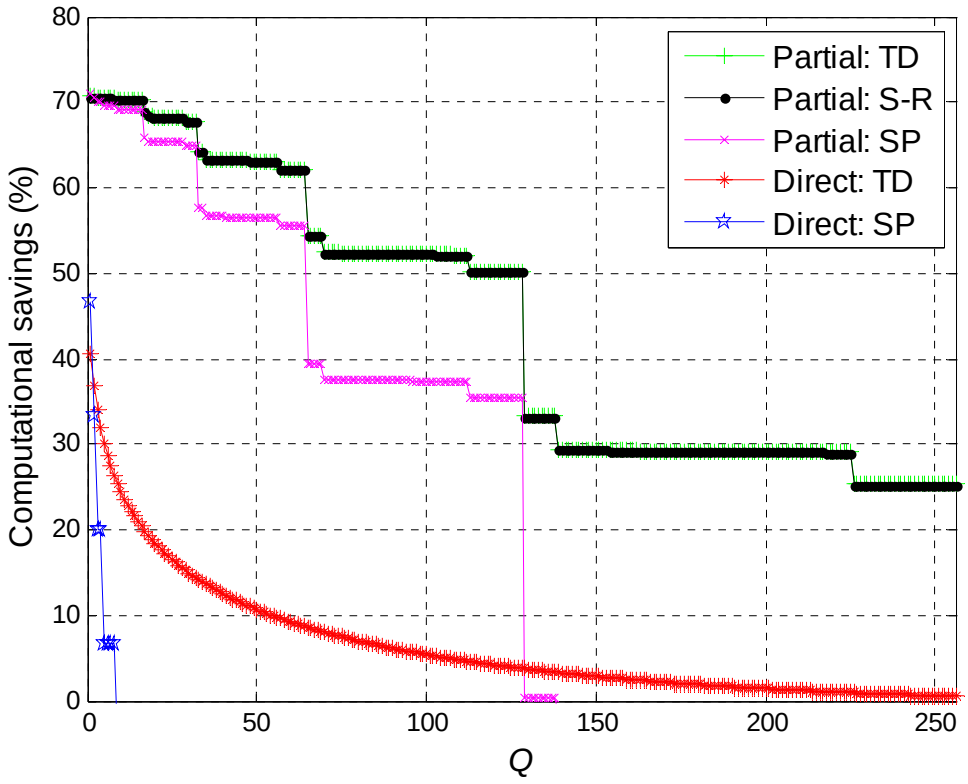

Figure 5-5: Influence of the DFT computation algorithm on the computational savings of partial and direct processing, over the direct approach based on S-R algorithm, for a waveform of $N_s = 20$ OQAM symbols in length assuming filter bank design with transform size $M = 1024$ and overlapping factor $K = 4$.

The Skinner's pruning algorithm provides computational savings over the Split-Radix FFT only for a very limited set of most narrow band allocations. The transform decomposition algorithm, on the other hand, provides savings of gradually decreasing amount with increasing bandwidth, over wider range of band allocations. Both the direct reference and the partial synthesis scheme can exploit the redundancy in the input vectors ($\mathbf{c}(v)$) to lower the IFFT implementation cost of narrow band allocations. The savings obtained are greater for the reference design due to higher relative sparseness of the input vector (for a given number of scheduled subcarriers ratio $Q/M < Q/P$) as a

result of bigger IFFT transform size (recall that $P \ll M$). However, regardless of the chosen DFT computation algorithm, the overall computational savings obtained with the partial synthesis scheme are notable.

5.1.4 Performance evaluation

Here, the FBMC-PS technique is compared to the direct reference design (FBMC-DS) for generating an equivalent FBMC uplink waveform. The performance is analyzed by evaluating the impact of the approximation error introduced by the non-ideality of the time-domain interpolation in the FBMC-PS structure. Note that the initial P-subchannel synthesis bank provides waveforms without approximation error for the subsequent processing stages. Therefore, what remains open is to demonstrate that the required time-domain interpolation can be accomplished efficiently and with sufficient accuracy, compared to the reference design based on the M-subchannel synthesis bank. The level and the impact of the approximation error are studied both in single-user and in multi-user cases.

5.1.4.1 Single-user case

We begin the analysis by considering the approximation error in a single-user case. In the following numerical example we consider the generation of FBMC uplink waveforms, each carrying $N_s = 20$ OQAM symbols over band allocations of various bandwidths $Q \in \{1 : 1 : M/4\}$, where the transform (IFFT) size in the full-size reference transmitter is $M = 1024$. Moreover, in the analysis we use our initial NPR prototype filter (overlapping factor is $K = 4$). Time-domain interpolation is performed using a cascade of halfband filters. We consider three different design cases, referred to as D_1, D_2, and D_3, where the minimum order filters that satisfy a stopband ripple requirement of $\delta_s \leq 0.001$, $\delta_s \leq 0.0003$, and $\delta_s \leq 0.0001$, (yielding approximately 60, 70, and 80 dB of image band attenuation, respectively) are used at different stages of the cascade.

The significance of the approximation error is evaluated through the detection of FBMC-PS generated uplink waveforms. At the receiver, processing corresponding to that of the full-size reference transmitter is carried out. In principle, inverse operations, with respect to those applied at the transmitter, are performed in reversed order. More specifically, the baseband processing at the receiver consists of the M-branch polyphase-filtering, the M-point FFT, subcarrier selection, the Q-point multiplication by $\beta_{k,n}^*$-coefficients, and the Q-point OQAM post-processing. Moreover, the signal transmission is assumed to be ideal in a sense that the effects of channel distortion and additive noise are not considered and perfect time synchronization is assumed. As a result, the non-ideality of the time-domain interpolation forms the only source of errors in the considered example, in addition to the background noise floor of approximately -65 dB set by the NPR prototype.

In order to estimate the average level of signal distortion, arising from the approximation errors, an error vector magnitude (EVM)[1] was evaluated according to [36]

[1] EVM is a well defined and widely adopted metric to measure the signal quality/purity. Moreover, as the estimated level of EVM is well below the level of thermal noise encountered in practice, the BER performance would dominantly be determined by the SNR operation point instead of the signal dispersion by the fractional interpolation.

$$\mathrm{EVM} = \sqrt{\frac{E\left\{\left|\tilde{c}[r]-c[r]\right|^2\right\}}{E\left\{\left|c[r]\right|^2\right\}}} \approx \sqrt{\frac{\frac{1}{N}\sum_{r=1}^{N}\left|\tilde{c}[r]-c[r]\right|^2}{\frac{1}{N}\sum_{r=1}^{N}\left|c[r]\right|^2}}, \tag{63}$$

where $E\{.\}$, $\tilde{c}[r]$, $c[r]$, and N denote the expectation of ensemble averages, the actual (measured) and the ideal symbols, and the length of the symbol sequence, respectively. Moreover, the mean squared error is normalized by the average power of the ideal signal. Figure 5-6 shows the evaluated (average) EVM in decibels for FBMC-PS as a function of bandwidth allocation Q.

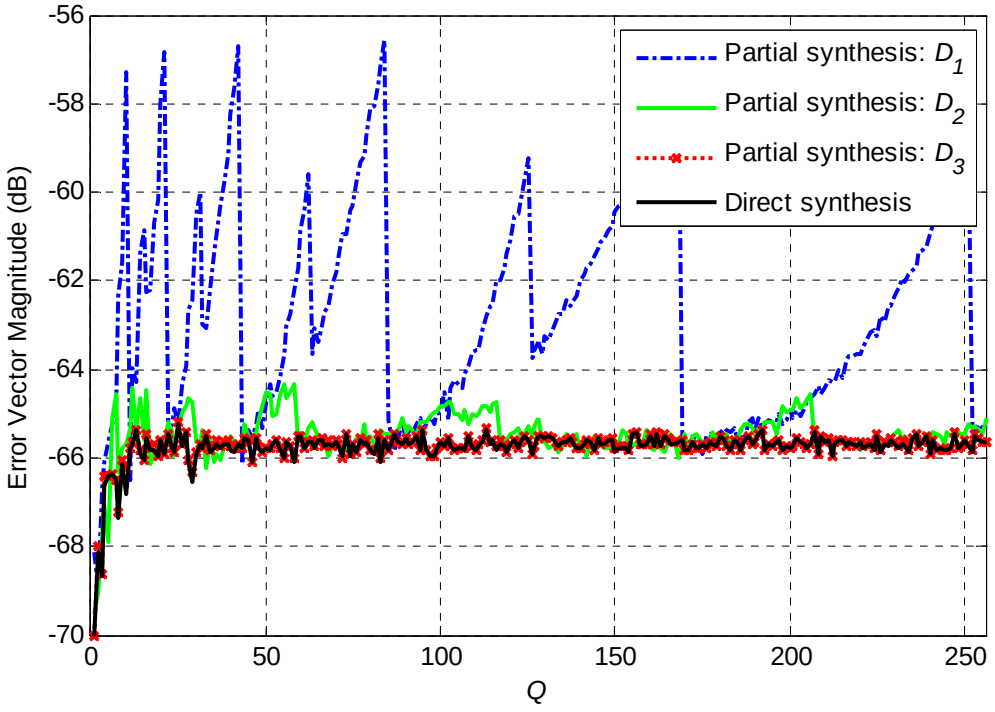

Figure 5-6: EVM as a function of bandwidth allocation Q with different time domain interpolator designs.

It can be observed that the resulting EVM is below -56 dB, -64 dB, and -65 dB, over the whole range of Q values, for interpolator designs D_1, D_2, and D_3, respectively. It should be emphasized that the level of EVM can be controlled by adjusting the specifications of the interpolation filtering. This enables various complexity-performance tradeoffs for the system design. In the literature, a variety of different interpolation filter designs have been proposed, each with its own performance-complexity tradeoff. It is the primary aim of this section, however, to demonstrate the feasibility and potential of the proposed processing structure through an example design based on a cascade of halfband filters, rather than to suggest a specific interpolator solution.

5.1.4.2 Multi-user case

In a multi-user case, the other users can be considered as potential sources of multiple access interference (MAI) due to a finite image band attenuation of the FBMC-PS interpolator. Since MAI degrades the detection performance of a specific uplink signal, it was numerically estimated from

the received compound multiple access (MA) signal at the receiver. A synchronous MA reception of ten FBMC-PS uplink waveforms with consecutive frequency band allocations (with a single subcarrier guard band in between) was considered. Furthermore, a perfect power control was assumed among the received uplink signals.

From a single-user detection point of view, other uplink users can be regarded as potentially interfering additive noise sources. In order to evaluate the variance of MAI, the mean-squared error (MSE) was estimated at the subcarriers allocated to a selected user being detected at a given time while there were transmissions on all subcarriers allocated to the rest of the uplink users. The average MSE was estimated over a set of one hundred random MA profiles (each with a randomly picked sequence of bandwidth allocations (Q) and modulation orders (4-, 16-, or 64-QAM alphabets) for different uplink users). Moreover, all the considered MA profiles were full bandwidth scenarios, i.e., the frequency bands allocated to the ten users (with the nine guard band subcarriers) summed up to the bandwidth of the IFFT size M in the direct synthesis. The level of MAI for halfband interpolator designs D_1, D_2, and D_3, were estimated to be -64 dB, -73 dB, and -75 dB, respectively.

5.2 On mixing multicarrier and single carrier modulations

The independence of subchannels permitted by FBMC gives the possibility to mix multicarrier and single carrier modulations in the same transmitted signal. This is a crucial feature in some situations, such as uplink when the mobile is far from the base station and low PAPR is mandatory in the transmission. Several approaches can be considered to implement the concept.

5.2.1 Single carrier modem

A basic scheme is illustrated in Figure 5-7.

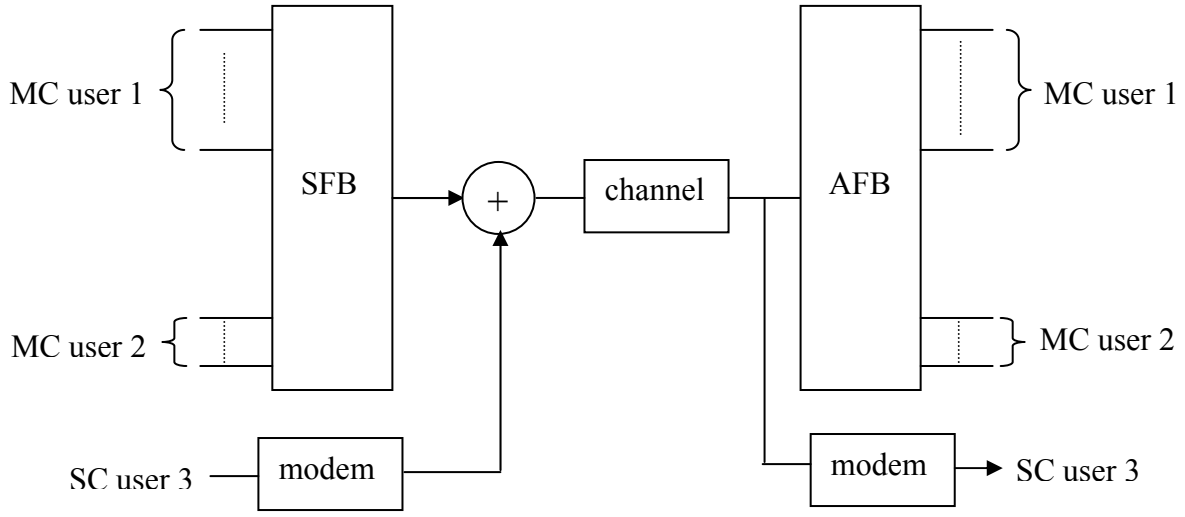

Figure 5-7: Mixing a single carrier user with multicarrier users.

A conventional modem with a low PAPR modulation (GMSK, EDGE, ...) can exploit the bandwidth which is available between the multicarrier users. The transmitter modem must include the proper filtering for insertion in the multicarrier signal which is fed to the channel. At the receiver, proper filtering must be included at modem input to prevent interference from the multicarrier signals. In fact, at both ends, these filtering operations are performed by the half-Nyquist filters of the modem. The approach is very flexible and efficient, but it means extra complexity. An alternative integrated technique can be considered.

5.2.2 DFT spreading

Several subchannels can be aggregated to yield a wide transmission bandwidth, in which a low PAPR signal is transmitted. In fact, it is the scheme adopted by 3 GPP-LTE for the uplink which is applied to FBMC. The principle is illustrated in Figure 5-8.

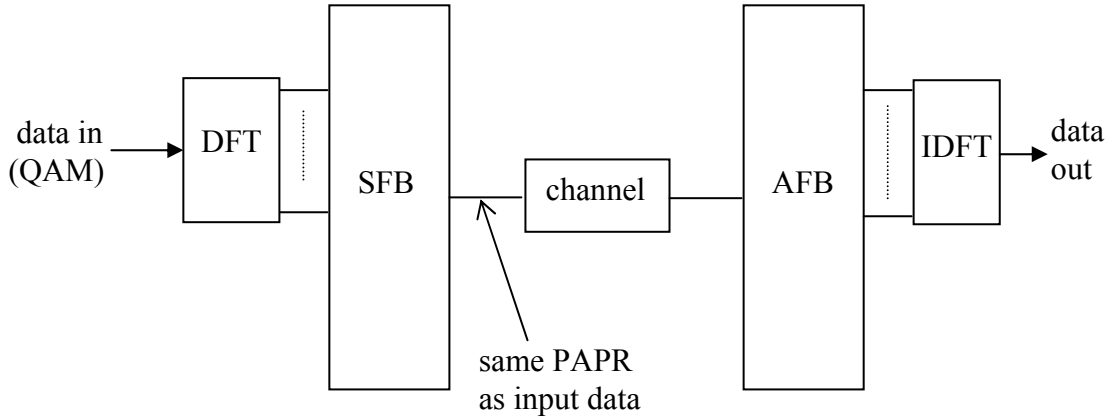

Figure 5-8: The concept of DFT spreading applied to FBMC.

The input data signal is applied to a DFT processor whose outputs are fed to the input of the SFB. In the DFT-s-OFDM case the synthesis filter bank is equivalent to an inverse FFT, and the input signal is restored at the SFB output, with a shift in frequency and a higher sampling rate. In these conditions, the low PAPR of the input signal is kept at the channel input. The inverse process takes place in the receiver.

As a first approach to implement the scheme in an FBMC system, independent subchannels are considered, with QAM modulation. This implies that, if the FFT in the transmitter has order N, then $2N$ subchannels of the FBMC system are needed. In this way, the Nyquist property of the subchannels is preserved and the system works as a set of N parallel independent subchannels.

An illustration is given in Figure 5-9 which shows the real transmitted signal with QPSK as the input data modulation. The number of subchannels actually used is $N = 32$ and 64 are reserved out of the total $M = 128$ subchannels. The complex samples coming out of the 32-FFT are applied to the inputs of SFB at a rate equal to the inverse of the subchannel frequency spacing. The emitted signal has the root-mean-square value RMS=90.7 and a peak value such that PAPR=$(2.91)^2$ (i.e., 9.3 dB). With this scheme, the PAPR is almost independent of the number of used subchannels. With $N = 8$, PAPR=$(2.81)^2$.

The minimum PAPR that can be obtained with QPSK modulation, comes from two effects:

- the complex-to-real conversion (carrier modulation), which introduces the factor $\sqrt{2}$,
- the half-Nyquist filter whose contribution in the peak value is the sum of the absolute values of the impulse response samples, about 2 in the above example. This factor can be reduced if the roll-off of the Nyquist filter is extended, at the cost of more spectral occupation.

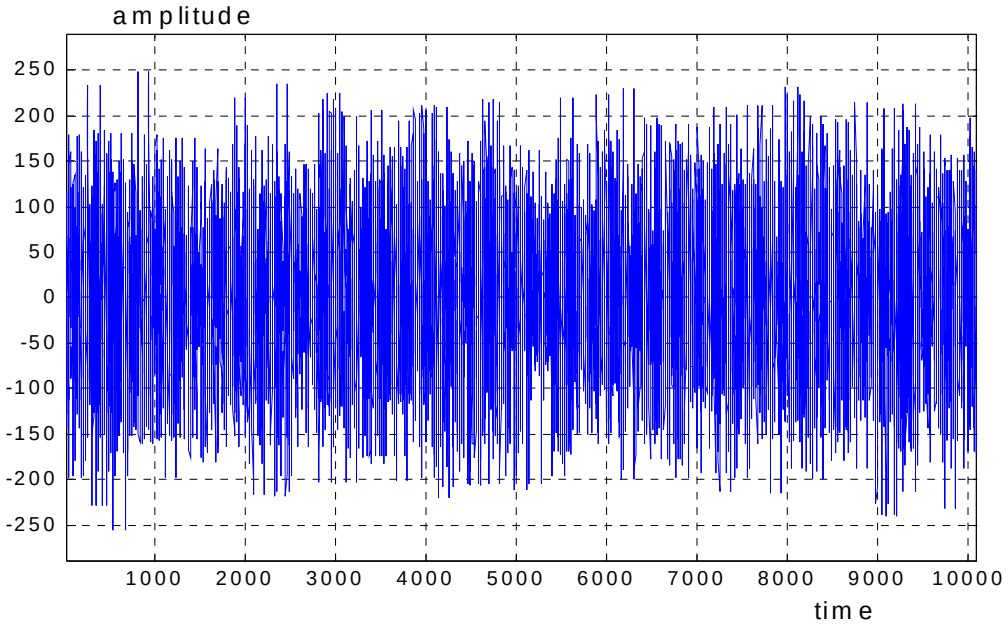

Figure 5-9: Transmitted signal with DFT-spreading (32/128 subchannels, RMS=90.7, PAPR=9.3 dB).

5.2.3 Filter bank spreading

In this section, we continue looking into the problem of mixing the multicarrier and single carrier modulations. Specifically, the complementary cumulative distribution function (CCDF) of PAPR of the synthesized signal is analyzed. Moreover, two different types of spreading are considered to be performed on the transmitted data prior to applying it into the FBMC transmitter, namely spreading by DFT and by an analysis filter bank. We refer to the latter approach as filter bank spreading. The following block diagrams show the models under investigation.

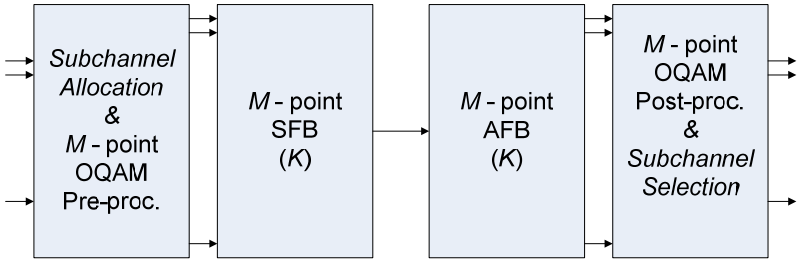

Figure 5-10: FBMC transmultiplexer core.

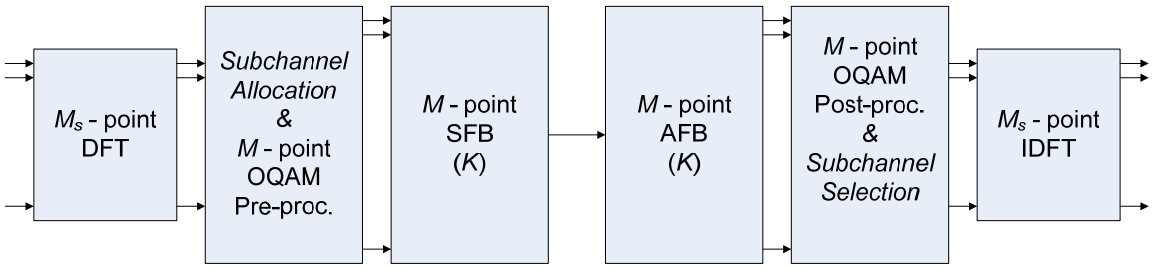

Figure 5-11: DFT-spread FBMC system (DFT-s-FBMC).

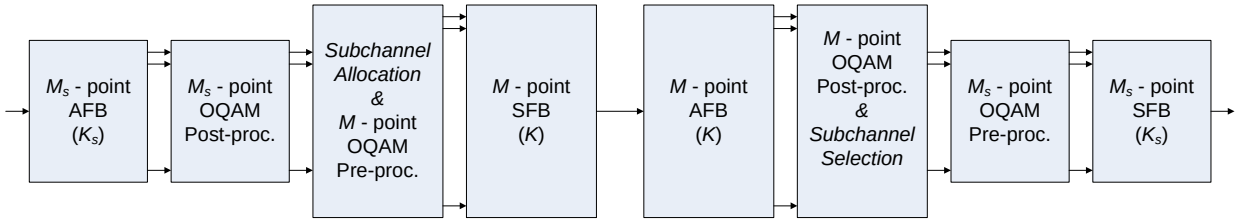

Figure 5-12: Filter bank –spread FBMC system (FB-s-FBMC).

In the models of Figure 5-11 and Figure 5-12, the spreading and the de-spreading operations performed in the transmitter and receiver, respectively, can be considered as additional pre-/post-processing blocks outside and independent of the FBMC transmultiplexer (TMUX) core shown in Figure 5-10. It should be noted that for the models of Figure 5-11 and Figure 5-12 the complex-valued samples from the spreading operator are allocated into the consecutive subchannels of the FBMC transmitter using OQAM modulation, in the same way as in the PHYDYAS FBMC model.

The CCDF analysis of the PAPR have been performed for the DFT –spread FBMC (DFT-s-FBMC) and the filter bank –spread FBMC (FB-s-FBMC) models considering two simulation setups with the following system parameters

Setup 1:

$M = 1024$	transform size in FBMC
$K = 4$	overlapping factor in FBMC
$M_s = 160$	number of allocated subchannels for a single-carrier user
$K_s = \{1, 3\}$	overlapping factor in the spreading/de-spreading FB (with $K_s = 4$, the performance is very similar to the case of $K_s = 3$)
$QPSK$	modulation type
$h_p = PHY$	prototype filter (PHY: PHYDYAS default filter, PR: perfect reconst-ruction, D1:C2: frequency sampling design with minimax criterion

Setup 2:

$M = 128$	transform size in FBMC
$K = \{3, 4, 5\}$	overlapping factor in FBMC
$M_s = 32$	number of allocated subchannels for a single-carrier user
$K_s = \{1, 3\}$	overlapping factor in the spreading/de-spreading FB (with $K_s = 4$, the performance is very similar to the case of $K_s = 3$)
$QPSK$	modulation type
$h_p = \{PHY, PR, D1 : C2\}$	prototype filter (PHY: PHYDYAS default filter, PR: perfect reconstruction, D1:C2: frequency sampling design with minimax criterion

The obtained results are shown in and Figure 5-14, respectively. Also, for the reference, shown are the corresponding CCDF curves for the DFT –spread OFDM (DFT-s-OFDM), OFDM and FBMC.

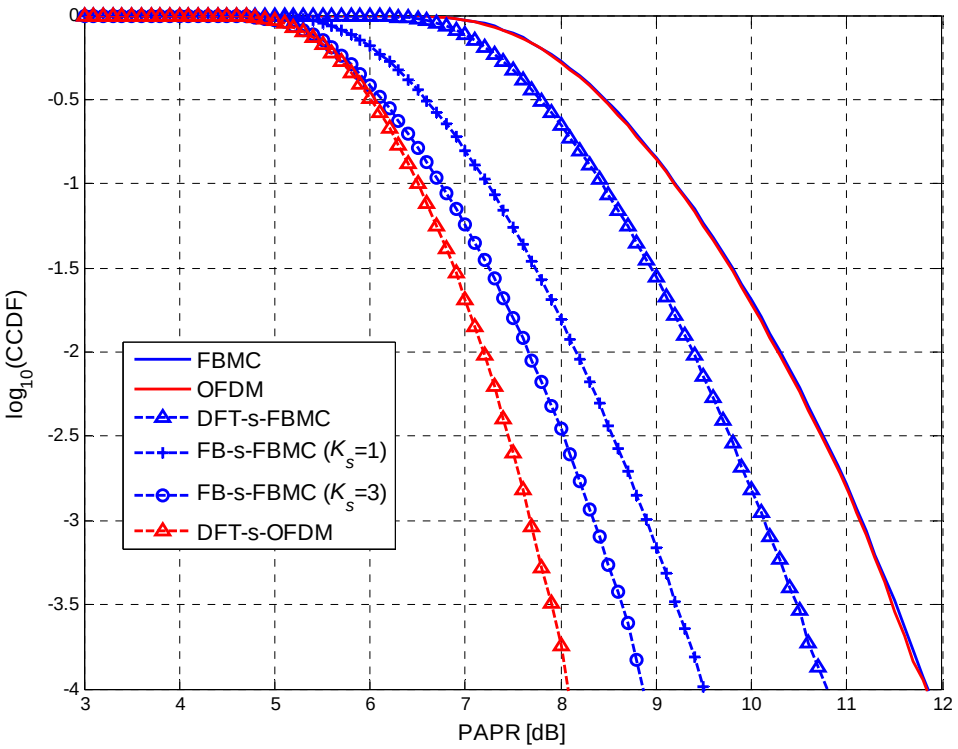

Figure 5-13: CCDF of PAPR for $M = 1024, K = 4$ and $M_s = 160$.

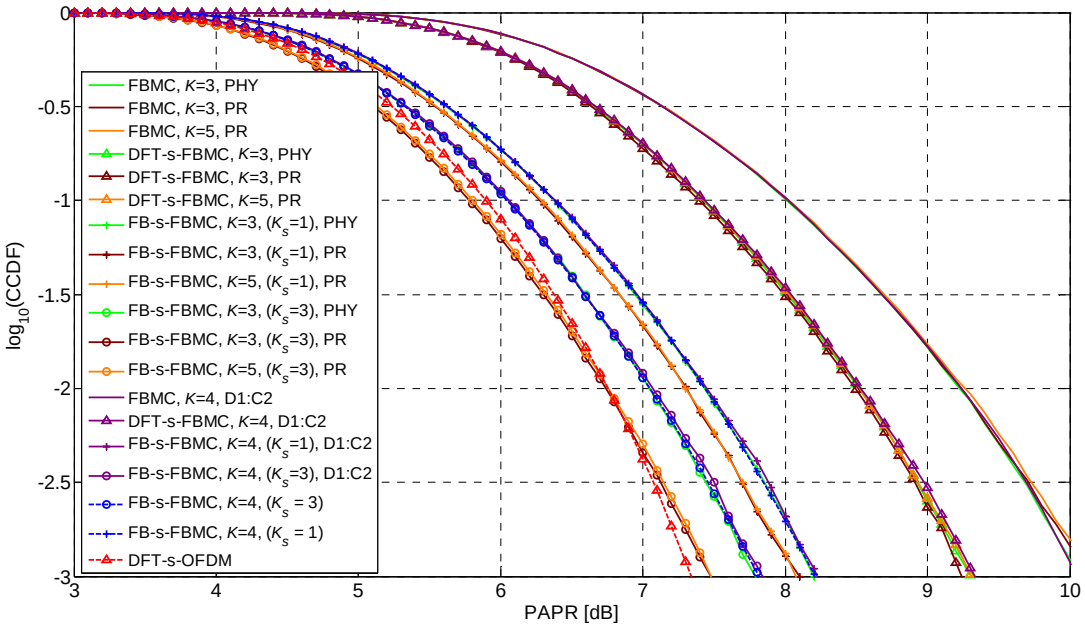

Figure 5-14: CCDF of PAPR for $M = 128$ and $M_s = 32$.

Based on the analysis, simply spreading the data with the DFT is not sufficient for FBMC (DFT-s-FBMC), at least when consecutive subchannel allocation is applied. The resulting reduction in the PAPR distribution is significantly lower compared to that obtained in case of DFT-s-OFDM. The spreading performance for FBMC can be improved using a structure of Figure 5-12 where, instead of M_s -point DFT, an M_s -point analysis FB and OQAM post-processing are used to spread the data prior to the FBMC transmitter. In the receiver side, the corresponding M_s -point OQAM pre-processing and synthesis FB are used for de-spreading the data. We denote this processing by FB-s-FBMC. It is possible to apply filter bank design with smaller overlapping factor (K_s) for the spreading operation compared to that (K) used in FBMC TMUX. The value K_s=3 gives a good tradeoff. It is obvious that FB-s-FBMC is computationally more demanding compared to DFT-s-FBMC. Also there is some overhead in data transmission capacity due to the "tails" of the spreading transform. However, the resulting performance is clearly better than with DFT-s-FBMC. It is also seen that the prototype filter has a bigger effect on the PAPR in the FB-s-FBMC than in FBMC transmission. With suitable certain prototype filters, it is possible to reach the performance of DFT-s-OFDM.

6 Achievements and conclusion

From the interactions with the other Work Packages in the first year of the project, it has become apparent that the prototype filter should have several essential characteristics

1) linear-phase Nyquist filter with unity roll-off, to minimize delay and complexity,
2) transmission zeros at the frequencies which are integer multiples of the subchannel spacing, for independent and accurate channel measurements,
3) attenuation increasing with frequency, to offer increasing level of protection from/to primary users in cognitive radio.

With these constraints, the main flexibility parameters in the system design are

1) the number of subchannels,
2) the overlapping factor, which determines the total number of filter coefficients,
3) the option for partial filter bank design, for example to equip a low rate user in uplink in an efficient manner.

The work in WP5 has taken into account both the constraints and the degrees of freedom, to offer to the system designer specific signal processing tools as well as helpful investigation results. The main signal processing tools are

- a complete characterization of the PHYDYAS reference prototype filter bank family,
- a set of techniques for alternative designs and optimization with various criteria,
- a software package for simulation and implementation in the demonstrator.

Performance analysis has been performed on several important aspects, particularly concerning peak-to-average power ratio, spectrum sensing performance, and interference rejection characteristics in cognitive radio.

A flexible single-carrier like transmission mode, similar to the DFT spread OFDM model adopted to the 3GPP-LTE uplink, has been defined for FBMC and shown to provide reduced PAPR characteristics approaching those of DFT spread OFDM.

The impact on the RF front end has been studied using analytical studies. Also a simulation platform has been developed for comparing the FBMC to OFDM with respect to the sensitivity to RF impairments. The preliminary results still have to completed and confirmed before making conclusions about the differences, which will be reported in a future PHYDYAS deliverable.

The MATLAB simulation software which has been delivered to WP9 includes the following items:

- Analysis and synthesis filter banks following the unified signal models described in Chapter 2. The FB software is split into four modules: pre-processing, SFB, AFB and post-processing, which makes it easy to integrate various transmitter and receiver subcarrier processing algorithms. Currently, prototype filter lengths of $L_p = KM - 1$ and $L_p = KM$ are supported, but the filter length $L_p = KM + 1$ can be easily included to the next version.

- On-line calculation of the filter bank coefficients based on the frequency sampling based design approach of Section 3.1.1. Default values of the design parameters are fixed based on the optimization results, but designs based on alternative optimization criteria can be easily adopted based on the results of Section 3.3. Also the coefficients of arbitrary prototype filters can be loaded, and a set of perfect-reconstruction filter bank designs are included as another reference for comparative studies.

The software is fully parametrized, highly modular, and follows the style recommendations adopted in PHYDYAS. Special attention has been paid on the efficiency of the code, since it will be the core module in all FBMC simulations. The software will be updated based on the needs of other work packages.

The other algorithms developed under WP5, including the partial TMUX and FB-s-FBMC models, are currently not included in the work plans of other WPs, but they can be made available, if such need emerges.

A physical layer for radio communications must have the capability to adapt to various situations, wireless networks as well as cellular systems. With the results obtained by WP5 and with the signal processing tools which have been generated, the designers of filter banks for FBMC systems should have enough material to cope with all cases and succeed in their developments.

REFERENCES

[1] H. S. Malvar, *Signal Processing with Lapped Transforms.* Artech House, Boston, MA, USA, 1992.

[2] P. P. Vaidyanathan, *Multirate Systems and Filter Banks*. Prentice Hall, Englewood Cliffs, NJ, USA, 1993.

[3] N. J. Fliege, *Multirate Digital Signal Processing*. John Wiley & Sons, Chichester, NY, USA, 1994.

[4] R. Van Nee and R. Prasad, OFDM *for Wireless Multimedia Communications*. Artech House, Norwood, MA, USA, 2000.

[5] S. D. Sandberg and M. A. Tzannes, "Overlapped discrete multitone modulation for high speed copper wire communications," IEEE J. Select. Areas Commun., vol. 13, pp. 1571-1585, Dec. 1995.

[6] G. Cherubini, E. Eleftheriou, S. Olcer, and J. M. Cioffi, "Filter bank modulation techniques for very high-speed digital subscriber lines," IEEE Commun. Mag., pp. 98-104, May 2000.

[7] L. Lin and B. Farhang-Boroujeny, "Cosine-modulated multitone for very-high-speed digital subscriber lines," EURASIP J. Applied Signal Processing, vol. 2006, Article ID 19329, 16 pages, 2006.

[8] P. Siohan, C. Siclet and, N. Lacaille, "Analysis and design of OFDM/OQAM systems based on filterbank theory," IEEE Trans. Signal Processing, vol. 50, pp. 1170-1183, May 2002.

[9] S. Mirabbasi and K. Martin, "Overlapped complex-modulated transmultiplexer filters with simplified design and superior stopbands," IEEE Trans. Signal Processing, vol. 50, pp. 456-469, Aug. 2003.

[10] J. Alhava and M. Renfors, "Exponentially-modulated filter bank-based transmultiplexer," in Proc. IEEE Int. Symp. Circuits and Systems, Bangkok, Thailand, May 2003, vol. IV, pp. 233-236.

[11] M. G. Bellanger, "Specification and design of a prototype filter for filter bank based multicarrier transmission," in Proc. IEEE Int. Conf. Acoustics, Speech, and Signal Processing, Salt Lake City, USA, May 2001, pp. 2417-2420.

[12] E. Dahlman, S. Parkvall, J. Sköld, and P. Beming, *3G Evolution: HSPA and LTE for Mobile Broadband Communication Systems*. Academic Press, Oxford, UK, 2007.

[13] T. Karp and N. J. Fliege, "Modified DFT filter banks with perfect reconstruction," IEEE Trans. Circuits and Systems II, vol. 46, pp. 1404-1014, Nov. 1999.

[14] A. Viholainen, J. Alhava, and M. Renfors, "Efficient implementation of complex modulated filter banks using cosine and sine modulated filter banks," EURASIP J. Applied Signal Processing, vol. 2006, Article ID 58564, 10 pages, 2006.

[15] A. Viholainen, J. Alhava, M. Renfors, "Efficient implementation of 2x oversampled exponentially modulated filter banks," IEEE Trans. Circuits and Systems II, vol. 53, pp. 1138-1142, Oct. 2006.

[16] M. Bellanger, *Digital Signal Processing – Theory and Practice*. Wiley, Chichester, NY, USA, 1999.

[17] P. N. Heller, T. Karp, and T. Q. Nguyen, "A general formulation of modulated filter banks," IEEE Trans. Signal Processing, vol. 47, pp. 986-1002, Apr. 1999.

[18] R. D. Koilpillai and P. P. Vaidyanathan, "Cosine-modulated FIR filter banks satisfying perfect reconstruction," IEEE Trans. Signal Processing, vol. 40, pp. 770-783, Apr. 1992.

[19] H. S. Malvar, "Extended lapped transforms: Properties, applications, and fast algorithms," IEEE Trans. Signal Processing, vol. 40, pp. 2703-2714, Nov. 1992.

[20] D. Pinchon, P. Siohan, and C. Siclet, "Design techniques for orthogonal modulated filterbanks based on a compact representation," IEEE Trans. Signal Processing, vol. 52, pp. 1682-1692, June 2004.
[21] R. Bregovic and T. Saramäki, "A systematic technique for designing linear-phase FIR prototype filters for perfect-reconstruction cosine-modulated and modified DFT filter banks," IEEE Trans. Signal Processing, vol. 53, pp. 3193-3201, Aug. 2005.
[22] H. Xu, W.-S. Lu, and A. Antoniou, "Efficient iterative design method for cosine-modulated QMF banks," IEEE Trans. Signal Processing, vol. 44, pp. 1657-1668, July 1996.
[23] P. S. R. Diniz, L. C. R. Barcellos, S. L. Netto, "Design of cosine-modulated filter bank prototype filters using the frequency-response masking approach," in Proc IEEE Int. Conf. Acoustics, Speech, and Signal Processing, Salt Lake City, USA, May 2001, pp. 3621-3624.
[24] P. Martin-Martin, R. Bregovic, A. Martin-Marcos, F. Cruz-Roldan, T. Saramäki, "A generalized window approach for designing transmultiplexers," IEEE Trans. Circuits and Systems I, vol. 55, pp. 2696-2706, Oct. 2008.
[25] J. Tellado, *Multicarrier Modulation with Low PAR: Applications to DSL and Wireless*. Kluwer Academic Press, Boston, 2000.
[26] M. Höyhtyä, A. Hekkala, M. Katz, and A. Mämmelä, "Spectrum awareness: Techniques and challenges for active spectrum sensing," in *Cognitive Wireless Networks*, F. H. Fitzek and M. D. Katz Eds. Springer, Dordrecht, The Netherlands, 2007, Chapter 18, pp. 353-372.
[27] B. Farhang-Boroujeny and R. Kempter, "Multicarrier communication techniques for spectrum sensing and communication in cognitive radios," IEEE Commucations Magazine, pp. 80-85, Apr. 2008.
[28] T. Ihalainen, A. Viholainen, M. Renfors, "On spectrally efficient multiplexing in cognitive radio systems," in Proc. IEEE Int. Symp. Wireless Pervasive Computing, Santorini, Greece, May 2008, pp. 675-679.
[29] T. A. Weiss, J. Hillenbrand, A. Krohn, and F. K. Jondral, "Mutual interference in OFDM-based spectrum pooling systems," in Proc. IEEE Vehicular Technology Conf., Milan, Italy, May 2004, pp. 1873--1877.
[30] Final Draft ETSI EN 300 744 V1.5.1, "Digital video broadcasting (DVB)," June 2004.
[31] ISO/IEC 8802-11, IEEE Std 802.11, "Part 11: Wireless LAN medium access control (MAC) and physical layer (PHY) specifications,", 2nd Ed., Aug. 2005.
[32] Y. C. Lim, "Frequency-response masking approach for the synthesis of sharp linear phase digital filters," IEEE Trans. Circuits and Systems, vol. 40, pp. 357-364, Apr. 1986.
[33] L. Maret, C. Dehos, M. des Noes, D. Morche, and J. Barletta , "Sensitivity of a MC-CDMA beyond 3G system to RF impairments", in Proc. IST Mobile & Wireless Communcations Summit, Desden, 2005.
[34] J. Stott, "The effects of phase noise in COOFDM", BBC Research & Development Technical Review, Summer, 1998.
[35] H. V. Sorensen and C. S. Burrus, "Efficient computation of the DFT with only a subset of input or output points," IEEE Trans. Signal Processing, vol. 41, pp. 1184-1200, Mar. 1993.
[36] Q. GU, *RF System Design of Transceivers for Wireless Communications*. Springer-Verlag, New York, USA, 2005.